An integrated study of hydrothermal white mica in the footwall of the Kangaroo Caves VMS deposit, Western Australia

C.T.N. VAN HINSBERG

An integrated study of hydrothermal white mica in the footwall of the Kangaroo Caves VMS deposit, Western Australia

by

CAMIEL T.N. VAN HINSBERG

SUPERVISORS

DR. F.J.A. VAN RUITENBEEK (UNIVERSITY OF TWENTE, FACULTY ITC)

DR. P.R.D. MASON (UTRECHT UNIVERSITY, FACULTY OF GEO SCIENCES)

ITC

Universiteit Utrecht

August, 2010

Abstract

The aim of this research was to determine isomorphous substitution reactions in white mica from the Panorama district, Western Australia and define the factors controlling these substitutions. For this study a total of 11 rock samples were collected in the footwall of the Kangaroo Caves VMS deposit. A range of different analytical techniques have been used to study the rock samples. Techniques used include SWIR spectral reflectance measurements, thin section petrography, microanalysis by electron microprobe and laser ablation ICP-MS, and whole-rock geochemical analyses.

Field sample laboratory spectra show that white mica and chlorite are spectrally dominant. Two types of white mica can be identified from the reflectance spectra based on the wavelength position of the main Al-OH absorption feature near 2200 nm of white mica. White mica of short absorption wavelengths (<2202 nm) and long absorption wavelengths (>2208 nm). This is in agreement with airborne-derived reflectance spectra from the area. Petrographic examination of thin sections reveals that the 2200 nm absorption wavelength position of white mica is not controlled by the completeness of feldspar destruction. Electron microprobe analyses show that the wavelength position is negatively correlated with the Al content of white mica. The Al content in the white mica is controlled by both the tschermak and pyrophyllitic substitution.

It has been difficult to define the factors controlling the white mica compositions. Temperature could be a possible factor, but also the chemistry of the hydrothermal fluids. However, it has been demonstrated that host rock lithology can be excluded as a possible factor.

Acknowledgement

I have a number of people to sincerely thank for their contribution and support during the realisation of this thesis. It sometimes has been a struggle, but with the help of these people I was able to successfully complete this research. In particular, I would like to thank the following persons:

I want to express my sincere gratitude to my supervisors Frank van Ruitenbeek and Paul Mason. You both have invested much time and effort in me. Our meetings and contact by telephone were always pleasant and constructive. I have learned a great deal from you that will help me in the future.

I would also like to thank Kim Hein for her help on the thin sections, and Tilly Bouten, Gijs Nobbe and Peter van Krieken for their assistance in using the electron microprobe, laser ablation ICP-MS and photomicroscope. Without your help this thesis would not have been possible.

A special thanks to my family who have helped me in so many ways. First of all to my parents for believing in me and for supporting me a hundred percent. To my brother Michel for writing the MATLAB program and for helping me retrieving papers that were difficult to find. To my sister Esther for helping me out with creating several figures and designing the cover of this thesis. A special thanks to my brother-in-law Patrick for his help during the process of writing this thesis.

Finally, I would like to thank Dr. H.J. Beckers for his support.

Contents

List of Figures

List of Tables

Chapter 1: Introduction

1.1 Problem definition

White micas are commonly formed in hydrothermal mineralisation systems and often referred to as sericite. These white micas (i.e. illite, muscovite, phengite) vary systematically over different hydrothemal alteration facies. Their compositional variations reflect physical and chemical conditions, and are therefore very useful for reconstructing extinct hydrothermal systems and in guiding mineral exploration. Airborne imaging spectroscopy and field-based reflectance spectroscopy are operational tools for identifying and mapping the compositional variations of white micas within a hydrothermal system (Cudahy et al., 2000; van Ruitenbeek et al., 2005). By studying the subtle 10–20 nm shift of the 2200 nm absorption minimum, the different white micas can easily be identified. The relationship between this wavelength position and the type of white mica was studied by several researchers (Beran, 2002; Duke, 1994). It appears to be a function of the chemical composition of white micas and in particular the Al-content in octahedral sheets, which is controlled by Tschermack substitution:
$Al^{vi} + Al^{iv} \leftrightarrow (Mg,Fe^{2+})^{vi} + Si^{iv}$

However, in our research area, the Panorama district in the Archean Pilbara Block of Western Australia, the relationship between the chemical composition of white micas and their absorption wavelengths is not well understood. There are indications that also other substitutions play a role and there seems to be a relation with the K content of white micas. Furthermore the mechanism that controls the chemical composition and therefore the absorption wavelength of white micas is not known. Possible factors are temperature, pressure, source and chemical composition of hydrothermal fluids, precursor minerals, and chemical reactions with other mineral phases.

The objective of this research is to determine the exact relationship between the absorption wavelength of white micas and their chemical composition in the study area and which substitution mechanisms determine the chemical composition of white micas. Furthermore, the most likely factors controlling the differences in chemical compositions will be identified.

In order to meet the objectives 11 highly altered volcanic rock samples from the Panorama district will be described petrographically. The major and trace element composition of the various minerals in the thin section will be determined by microprobe and laser ablation analysis. Focus will be on the determination of chemical composition of white micas and the variation between and within the rock samples. The petrographic, microprobe and laser ablation data will be integrated with whole rock geochemistry and spectral measurements.

1.2 Main research question

Which isomporphous substitutions reactions have resulted in a wavelength shift of the main Al-OH absorption feature of white mica in the Panorama district, Pilbara craton, Western Australia and what are the factors controlling these substitution reactions?

1.3 Research objectives

Research objectives of the present study were:

- Determine spectral parameters from field sample laboratory spectra.
- Compare field sample laboratory spectra with airborne spectra.
- Petrographically describe the thin sections of the field samples
- Examine compositional variations in white mica rich samples
- Examine trace element concentrations in white mica
- Determine the factors controlling compositional variations in white mica
- Identify the primary rock type of the field samples

1.4 Test area

The 11 sample points for this study are located in the footwall of Kangaroo Caves and approximately 800 m south-southwest of the VMS mineralisation. The volcanic rocks are exposed as a range of dark rugged hills encircling the lighter colored topographic low of the Strelley (Monzo)granite (Drieberg, 2003; Brauhart, 1999). Topographic relief is up to 300 m and outcrop exposure is excellent. The region is semi-arid but can experience cyclonic activity in summer, which brings infrequent but heavy rainfall. The vegetation is dominated by spinifex grass over the hills with eucalypts and other trees variably developed along the major ephemeral drainage systems (Figure 1.1). Infrequent fires have left large areas with differing extents of spinifex cover (Cudahy & Quigley, 2004). Metamorphism of the volcano-sedimentary succession at the Kangaroo Caves VMS mineralization may be less than prehnite-pumpellyite facies. Most of the succession is essentially unmetamorphosed, with the rocks containing either primary or hydrothermal alteration textures (Vearncombe, 1995; Vearncombe et al., 1995; Vearncombe et al., 1998; Vearncombe & Kerrich, 1999). The surface rocks in the study area are weakly weathered. Weathering is characterized by the presence of iron-rich coatings of several millimetres in thickness and sometimes the presence of the secondary minerals halloysite and kaolinite (Van Ruitenbeek et al., 2006).

Figure 1.1 Outcrop exposure of the volcanic rocks in the Panorama district near the sample locations. The area of low topography in the far distance is the Strelley granite. Supergene oxidation gives the rocks its distinct red-brown colour.

1.5 Organisation of the thesis

The thesis has been written in 9 chapters.

Chapter 1 deals with the main problems behind this thesis, the research question and the objectives.

Chapter 2 describes the regional geology and hydrothermal alteration system of the Panorama district.

Chapter 3 describes all the analytical techniques employed on the rock samples and discusses the result of analytical method validation.

Chapter 4 presents the results of SWIR reflectance measurements on the rock samples.

Chapter 5 presents the results of petrologic examination of the thin sections.

Chapter 6 presents the results of electron microprobe analyses on white mica.

Chapter 7 presents the results of laser ablation ICP-MS analyses on white mica

Chapter 8 presents the results of whole-rock lithogeochemical analyses.

Chapter 9 discusses the data and interpretations presented in each of the preceeding chapters and makes conclusions.

Chapter 2: Geological setting of the Panorama district

2.1 Regional geology

The following section summarises work presented in Van Kranendonk (2000) and Van Kranendonk et al. (2001, 2002, 2006) and references therein The Panorama district (Figure 2.2) is located within the Soanesville Greenstone belt in the East Pilbara Terrane part of the Pilbara Craton in Western Australia. In 2006 detailed mapping and geochemistry, together with a large amount of geochronological data have resulted in a revised lithostratigraphy of supracrustal and intrusive rocks of the Pilbara Craton (Van Kranendonk et al., 2006). In this thesis the revised lithostratigraphy of Van Kranendonk et al. (2006) will be followed (Figure 2.1). The East Pilbara Terrane consists of three principal elements:

- A largely cryptic, ancient (3.72 – 3.60 Ga) sialic basement.
- A thick, demonstrably autochthonous succession of variably preserved, low- to medium-grade volcanic and sedimentary rocks (greenstones) known as the Pilbara supergroup. The Pilbara Supergroup is deposited into 4 groups that include, from base to top:
    - The Warrawoona Group, spanning a continuous range in ages from ≥ 3.53 to 3.43 Ga.
    - The Kelly Group, constrained by the youngest age from the underlying Warrawoona Group (ca. 3.43 Ga) and the overlying Sulphur Springs Group (ca. 3.26 Ga).
    - The Sulphur Springs Group, ranging in age from ca. 3.26 to 3.24 Ga.
    - The Gorge Creek Group, constrained by the youngest age from the underlying Sulphur Springs Group (ca. 3.24 Ga) and a maximum depositional age of ca. 3.02 Ga for the De Grey Supergroup (see below).
- And five supersuites of granitic rocks that include, from early to late emplacement:
    - The 3.49 to 3.460 Ga Callina Supersuite.
    - The 3.45 to 3.420 Ga Tambina Supersuite.

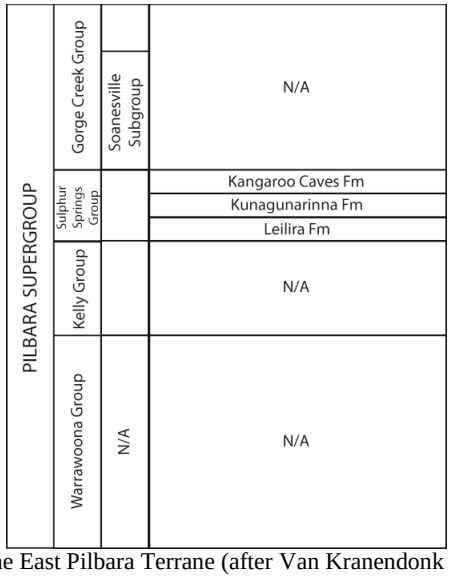

Figure 2.1 Stratigraphic column of the East Pilbara Terrane (after Van Kranendonk et al., 2006).

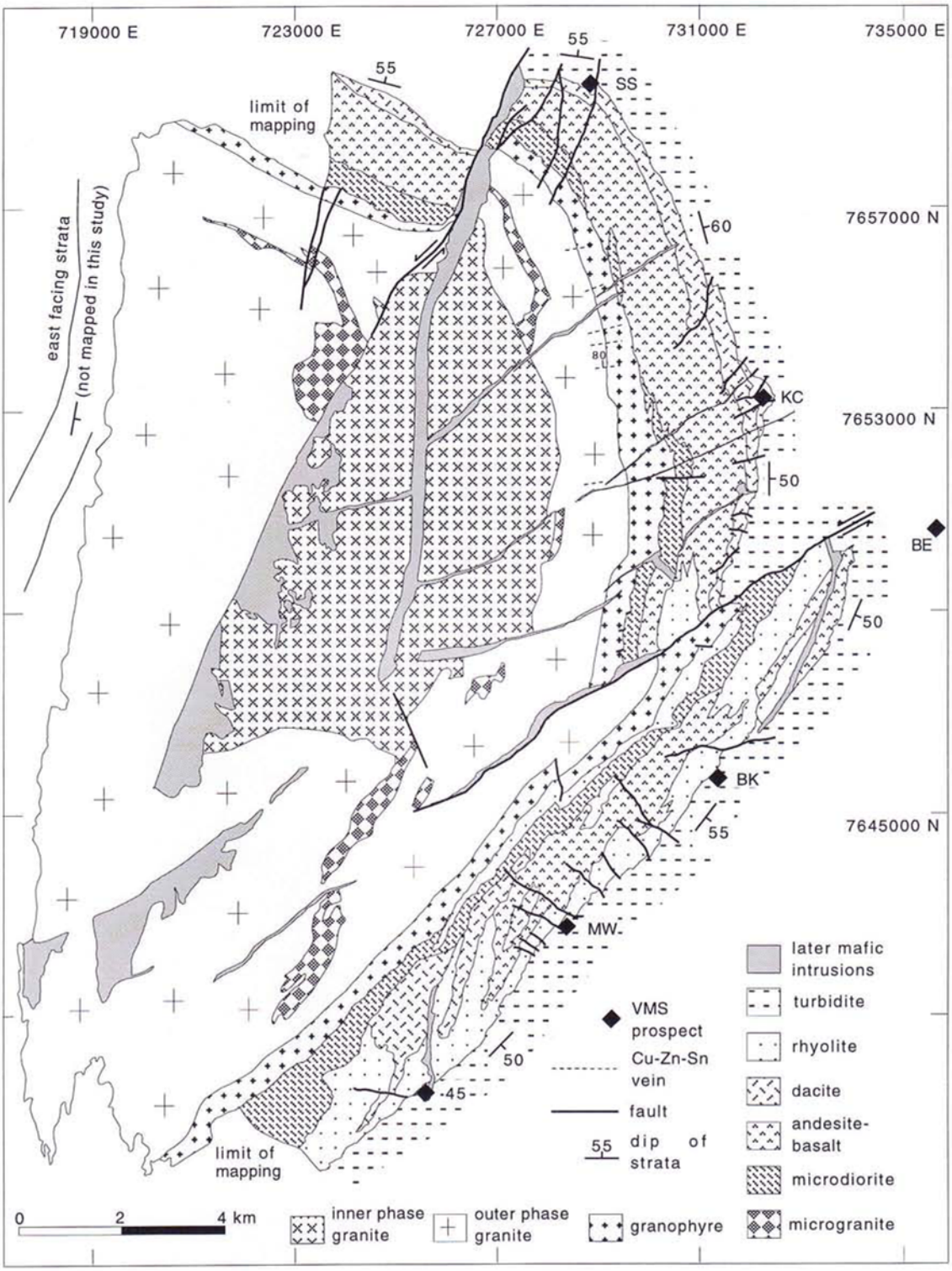

Figure 2.2 Geology of the Panorama study area after Brauhart (1999).

- The 3.33 to 3.29 Ga Emu Pool Supersuite.
- The 3.28 to 3.23 Ga Cleland Supersuite.
- The 3.20 to 3.17 Ga Mount Billroth Supersuite.

The Strelley (Monzo)granite is assigned to the Cleland Supersuite. The Pilbara Supergroup is unconformably overlain by the ca 3.02 to 2.93 Ga De Grey Supergroup. The Sulphur Springs Group and Soanesville Subgroup outcrop in our study area and will be discussed in more detail below. The stratigraphic description presented here refers only to the Soanesville greenstone belt. For a detailed lithostratigraphic description of the other two groups or other greenstone belts the reader is referred to the work of Van Kranendonk et al. (2001, 2002, 2006).

Sulphur Springs Group: The Sulpur Springs Group in the Soanesville belt is a succession of dominantly volcanic rocks. It reaches a maximum thickness of about 2500-3000 m. The group unconformably overlies the Kelly Group and is divided into three formations, from base to top:

- The Leilira Formation, a thick (0.1 – 0.5 km) unit of turbiditic sediments consisting of interbedded sandstones, wackes and mudrocks.
- The Kunagunarrina Formation, a thin unit of magnesian and komatiitic basalts capped in places by a distinctive bed of silicified vitric-lithic-crystal tuff containing mafic-ultramafic scoria, kerogenous chert pebbles and quartz from a felsic volcanic source.
- The Kangaroo Caves Formation, a regionally extensive pile of intermediate to felsic volcanic rocks 0.1 – 1.5 km thick, which forms the bulk of the succession. Felsic volcanism was coeval with emplacement of the Strelley Monzogranite laccolith, both of which have been dated at ca. 3238 Ma (Brauhart, 1999, Buick et al., 2002)

The Sulphur Springs Group has been inflated by syn- to post-volcanic sills, including the syn-volcanic Strelley Monzogranite. The Strelley Monzogranite contains two major phases. An outer equigranular hornblende-biotite granite with a granophyric upper margin and an inner porphyritic biotite-hornblende-magnetite granite which intrudes the outer phase. The outer phase has the geometry of a sill that was intruded at high crustal levels, indicated by miarolitic cavities in the marginal granophyre. This sill was then inflated into a laccolith by the intrusion of the inner phase, also a high-level event as shown by its highly variable phenocryst abundance. Both phases have been intruded by microgranite sills and later by dolerite dykes (Buick et al., 2002)

Similar profiles in trace-elements diagrams, similar REE behaviour, consistent Nb-Ta troughs, and high normalized Th contents, suggest that the igneous rocks in the Sulphur Springs Group are related to a common partial melt source. These trace-element characteristics are consistent with an arc-related setting (Brauhart, 1999).

The so called “marker chert”, comprising a laminated black chert, marks the contact between the Sulphur Springs Group and the overlying Gorge Creek Group. This chert horizon is typically less than 5 m thick, but thickness (up to 80 m) around the VMS mineralization sites, like Kangaroo Caves.

Soanesville Subgroup: The Soanesville Subgroup reaches a maximum thickness of about 6000 m in the Soanesville greenstone belt, and overlies the Sulphur Springs Group unconformably. The upper surface of the marker chert was eroded in many places prior to Gorge Creek deposition; the lower Gorge Creek sedimentary rocks onlap the marker chert at angles up to 15°, and the uppermost rocks of

the Sulphur Springs Group have undergone pervasive and pronounced hydrothermal alteration, unlike those of the basal Soanesville Subgroup. However, there is no change in metamorphic grade or deformational style across the unconformity, suggesting that the hiatus was not particularly prolonged (Buick et al., 2002).

The Soanesville succession in the northern Soanesville belt is dominated by fining-upwards turbiditic and chemical sedimentary rocks, ranging from immature sandstones and wackes, through ferruginous shales and muddy ironstones with interbedded debris-flow breccias, to a cap of banded iron-formation. Interpersed through these are different gabbroic sills in the lower part of the succession, thick tholeiitic flows with gabbroic textures, amygdaloidal flowtops and tuffaceous interbeds in the middle and pillowed magnesian basalts near the top (Thomas, 1997, *cited by* Buick et al., 2002). The whole sequence is unconformably overlain by sediments of the late Archean De Grey Supergroup.

2.2 Metamorphism

Metamorphic mineral assemblages in the greenstones show a common decrease in temperature away from the granitoid complexes, from lower amphibolite facies adjacent to granotoid complexes to greenschist and prehnite-pumpellyite facies throughout most of the upper part of the Warrawoona, Kelly, Sulphur Springs Group and Soanesville Subgroup, to very low temperature (anchizone) metamorphism of the De Grey Supergroup and Fortescue Group of the Hamersley Basin succession (Van Kranendonk, 2000; Van Kranendonk et al., 2001). Anchimetamorphism, a term only accepted among some European pertrologists, is the transitional field of overlap between diagenesis and metamorphism (Williams et al., 1982), better known as the zeolite metamorphism mineral facies. Examination of the Strelley Monzogranite by Hickman (1983) revealed the secondary minerals calcite, epidote, chlorite, rutile and rare prehnite, indicating prehnite-pumpellyite metamorphism. A lack of garnet with high-temperature mineral assemblages indicates low to moderate pressures during metamorphism. The annular distribution of metamorphic facies around the granitoid complexes, and the decrease in grade with stratigraphic height, is interpreted to reflect the effects of contact metamorphism and progressive structural doming.

2.3 Hydrothermal alteration

The following section summarizes work presented in Brauhart et al. (1998, 2000), and Brauhart (1999). Four major alteration facies are present in the volcanic and intrusive rocks in the Panorama district, with a series of subdivisions in each facies (Figure 2.3). Alteration facies are not lithology specific, but are developed in all lithologies from andesite-basalt, through rhyolite, to granite. The four alteration facies are the following:

- Background alteration, which is akin to spilitic alteration in basalt, and keratophyric alteration in felsic rocks, is typified by an albite and/or K feldspar-chlorite-calcite and/or ankerite-quartz-pyrite ± leucoxene ± magnetite ± sericite assemblage.
- Feldspar-sericite-quartz alteration is commonly characterized by a K feldspar and/or albite-sericite-quartz-ankerite-leucoxene ± pyrite assemblage. In rocks transitional to background alteration, minor chlorite is present.
- Sericite-quartz alteration is completely feldspar-destructive and is typically a quartz-sericite-leucoxene ± ankerite ± pyrite assemblage.

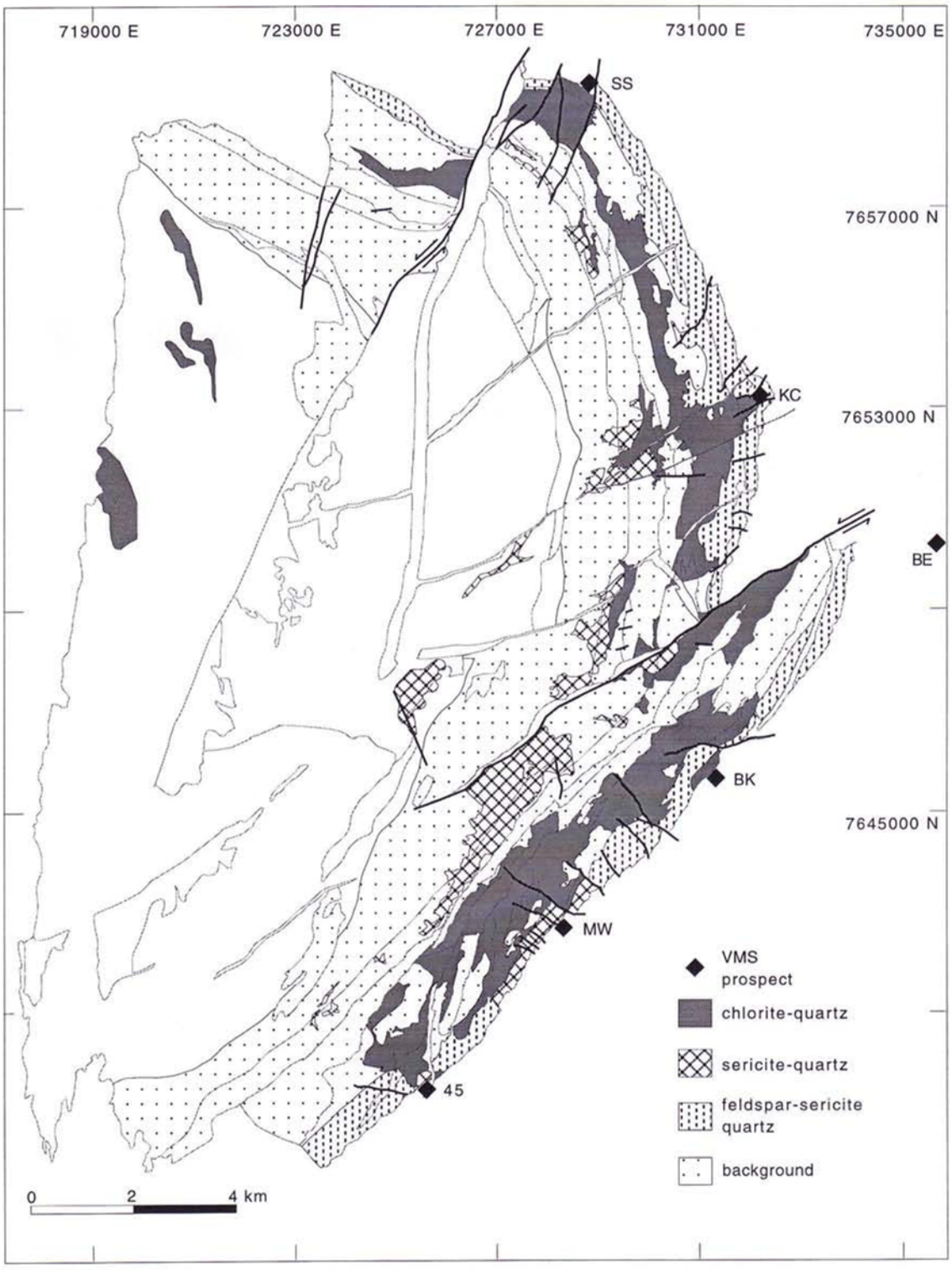

Figure 2.3 Alteration facies map of the Panorama study area after Brauhart (1999).

- Feldspar-destructive chlorite-quartz alteration is defined by a quartz-chlorite-sericite ± leucoxene ± hematite assemblage, in which pyrite ± base metal sulfides and ankerite-siderite are only developed immediately beneath zones of base metal mineralization.

Feldspar-bearing rocks at the top of the volcanic pile are enriched in potassium and silicon, but depleted in sodium, and contrast those at the bottom of the volcanic pile, which are enriched in sodium and depleted in potassium. Sericite-quartz-altered rocks are typically enriched in silicon and depleted in calcium, sodium, and iron, whereas chlorite-quart-altered rocks, which dominate transgressive feldspar destructive alteration zones, are marked by potassium-calcium-sodium depletion and magnesium-iron enrichment. Copper and zinc are strongly depleted in rocks at the base of the volcanic pile and, to a lesser extent, in transgressive feldspar-destructive alteration zones. The amount of metal leached from the volcanic pile is far greater than that contained in known deposits, and thus a magmatic metal source is not necessary to explain the formation of the Panorama VMS deposists.

Whole-rock oxygen isotope data of Brauhart et al. (2000) are consistent with a hydrothermal system dominated by seawater, in which low-temperature alteration took place in semi-conformable alteration zones at the top of the volcanic pile (high $\delta^{18}O$ values), and high temperature alteration took place at the base of the volcanic pile and in transgressive feldspar-destructive alteration zones (low $\delta^{18}O$ values). However $\delta^{18}O$ values for sericite-quarzt-altered granite are more consistent with a dominant magmatic fluid. Fluid exsolution textures, semi-massive copper-zinc-tin veins, and greisen style alteration in the Strelley Monzogranite provides supporting evidence for a contribution of magmatic fluids at the base of the Panorama VMS hydrothermal system.

A convective hydrothermal model is invoked to explain this distribution of alteration facies, whole-rock geochemical values, and oxygen-isotope data (Brauhart et al., 1998, 2000). In this model semi-conformable alteration zones represent seawater recharge, and transgressive feldspar-destructive alteration zones mark the path of evolved seawater discharging back to the seafloor. The interpreted discharge sites are coincident with base-metal sulphide deposits at the top of the volcanic pile.

2.4 Spectral information

In the Panorama VMS district numerous successful studies have been conducted, using field and airborne spectroscopy to map the mineralogy, mineral chemistry and spatial geometry of the Panorama hydrothermal alteration system (Cudahy et al., 1999; Cudahy & Quigley, 2004; Huston et al., 1997; Van Ruitenbeek et al., 2005, 2006). The area makes good results using these techniques, because of the benefits as a semi-arid environment with relatively unmetamorphosed and unweathered rocks well exposed over large areas, with critical alteration minerals that contain diagnostic absorption features (Cudahy & Quigley, 2004). In the studies particular attention is given to the short wavelenght infrared (SWIR) region between 1300 and 2500 nm as hydrothermal minerals such as white micas and chlorite have diagnostic features within these wavelenghts. Chlorite has an absorption feature around 2250 nm. The depth and position of the white mica and chlorite absorption features are useful tools to define the alteration zonation. High white mica concentrations and low chlorite concentrations coincide with feldspar-sericite-quartz alteration facies mapped by Bauhart (1999). In the feldspar-sericite-quartz alteration facies the white mica absorption peak shifts from ca. 2199 nm to ca. 2215 nm from the top of the volcanic succession downwards, due to a increase in temperature (Van Ruitenbeek et al., 2005). Chlorite dominates in the chlorite-quartz alteration facies mapped by Brauhart (1999) and coincide

with a high temperature discharge sites. Recognition of hydrothermal discharge sites is critical for locating areas of potential economic base metal mineralisation.

Chapter 3: Description and validation of the employed analytical procedures

3.1 Introduction

A range of different analytical techniques had been used to study the 11 rock samples from the Panorama district. Rock samples were located in the footwall of the Kangaroo Caves VMS deposit and comprise different lithologies and alteration facies (Figure 3.1). Sample locations and descriptions are summarised in appendix 1. Techniques used include spectral reflectance measurements, thin section petrography, microanalysis by electron microprobe and laser ablation ICP-MS, and whole-rock geochemical analyses. An overview of the different analytical techniques employed on each of the 11 samples is given in Table 3.1.

This chapter describes the analytical procedures that were employed and discusses the results from analytical method validation. All the analytical data generated from the 11 samples are available through the enclosed CD-ROM in the folder *Analytical data*.

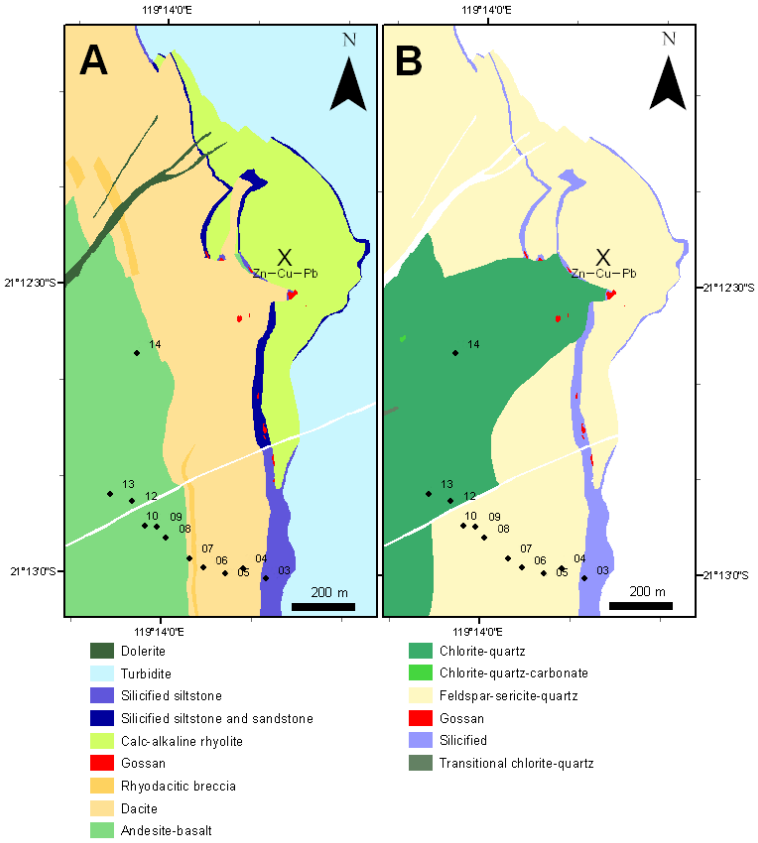

Figure 3.1 Geology and alteration facies map of the Kangaroo Caves footwall showing the sample locations. For clearness only the two numbers of each sample point are shown.

Table 3.1 Overview of the various analytical techniques employed on each of the 11 samples.

	p03	p04	p05	p06	p07	p08	p09	p10	p12	p13	p14
Spectral reflectance measurements	X	X	X	X	X	X	X	X	X	X	X
Thin section petrography	X	X	X	X	X	X	X	X			
Electron microprobe analysis		X	X	X	X	X	X	X			
Laser ablation ICP-MS analysis		X		X	X	X	X	X			
Whole-rock geochemical analysis	X	X	X	X	X	X	X	X	X	X	X

3.2 Spectral reflectance measurements

Reflectance spectra in the wavelength range of 350–2500 nm were obtained using an ASD FieldSpec Pro spectrometer. To achieve high quality spectra, measurements were taken at the ITC laboratory (Enschede, The Netherlands) using the contact reflectance probe configuration. The contact reflectance measurements were performed on clean, flat surfaces cut for the preparation of the thin sections. Sampling interval for the ASD FieldSpec Pro spectrometer was 1.4 nm for the 350–1000 nm spectral range and 2 nm for the 1000–2500 nm spectral range. Spectral resolution was 3 nm at 700 nm, 10 nm at 1500 nm and 10 nm at 2100 nm. Spectrum average was set at 25 scans per spectrum.

For each sample three separate reflectance measurements were taken at different positions on the sample. Results of these measurements are available on the enclosed CD-ROM through the excel document *Spectral reflectance measurements*. Excellent agreement was shown between the three separate reflectance measurements per sample and consequently the rock samples were assumed to be homogeneous on a centimetre scale. Therefore, results presented for each sample were based on an average of the three separate measurements per sample.

3.2.1 Spectral parameters

Several spectral parameters were used to characterise the spectra of the 11 rock samples. The spectral parameters derived from the spectra were the wavelength position and depth of absorption features and the white mica alteration index (WMAI). The wavelength position of absorption features often varies between 'uncorrected' reflectance spectra and hull corrected spectra. In this study reported wavelength positions were that of hull quotient corrected spectra. Hull quotient corrected spectra were created using the image processing software program ENVI 4.7.

The depth, D, of an absorption feature was calculated according to the formula of Clark & Roush (1984, *cited in* Clark, 1999):

$$D = 1 - \frac{R_b}{R_c}$$

R_b is the reflectance at the reflectance minimum and R_c is the reflectance of the hull at the same wavelength as R_b.

The WMAI is a measure of the spectral dominance of white mica over chlorite and described by Van Ruitenbeek et al. (2005) (Figure 3.2):

$$WMAI = \frac{D_{AlOH}}{D_{AlOH} + D_{FeOH}}$$

where

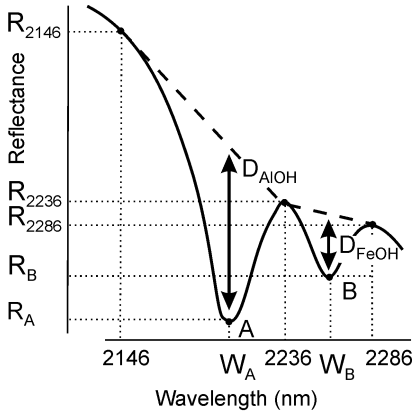

Figure 3.2 Reflectance spectrum illustrating the principles of the white mica alteration index (WMAI) as described by Van Ruitenbeek et al. (2005). Function parameters in the figure are explained in the text.

$$D_{AlOH} = R_{2146\,nm} - \frac{(W_A - 2146)}{90} * (R_{2146\,nm} - R_{2236\,nm}) - R_{W_A}$$

and

$$D_{FeOH} = R_{2236\,nm} - \frac{(W_B - 2236)}{50} * (R_{2236\,nm} - R_{2286\,nm}) - R_{W_B}$$

D_{AlOH} is the depth of the Al-OH absorption feature near 2200 nm, diagnostic for white mica (Pontual et al., 1997b). D_{FeOH} is the depth of the Fe-OH absorption feature near 2245 nm, diagnostic for chlorite (Pontual et al., 1997b). *A* is the reflectance minimum of the Al-OH absorption feature and *B* is the reflectance minimum of the Fe-OH absorption feature. R_x is the reflectance at wavelength *x*, and W_Y is the wavelength position of feature *y*. Note that the depth calculated for the WMAI is described differently than the depth defined by Clark & Roush (1984, *cited in* Clark, 1999). The WMAI ranges from 0 to 1 and increases with increasing white mica abundance relative to chlorite.

3.3 Thin section photographs

Photographs of the thin sections were made at Utrecht University, The Netherlands. A Leica DC300 digital camera system was mounted on a Leica DMRX polarised light microscope. These were attached to a computer equipped with Leica's image processing software program QWin to digitally enhance and capture the images. Photographs of a ruler were taken at each magnification to determine the field of view of the images.

3.4 Electron microprobe analyses

In total 264 electron microprobe analyses were performed on the thin sections p04 to p10. The results of these analyses are available on the enclosed CD-ROM through the Excel document *Electron microprobe analyses*. About 80 % of the analyses were performed for the 10 elements Si, Al, Na, K, Mg, Ca, Ti, Cr, Mn and Fe. For the other 20 % of the analyses also concentrations of the additional elements Ni, P, S, F and Cl were determined.

The electron microprobe analyses were conducted on carbon-coated thin sections using a JEOL JXA-8600 Superprobe with five wavelength-dispersive spectrometers at Utrecht University, The Netherlands. The microprobe was equipped with Voyager IV software by Noran Instruments.

Quantitative analyses were performed using Noran's PROZA matrix correction routine. The instrument was set at an acceleration voltage of 15 kV with a beam current of 20 nA and a take-off angle of 40°. Counting time for Ni was 50 seconds and for all the other elements 30 seconds. Standards used for the different elements were as follows: diopside for Si and Ca, corundum for Al, hematite for Fe, tephroite for Mn, forsterite for Mg, $KTiPO_5$ for K and P, jadeite for Na, TiO for Ti, chromium metal for Cr, nickel metal for Ni, chalcopyrite for S, halite for Cl and fluorite for F.

3.4.1 Limit of detection and limit of quantitation

Laboratory reporting limits can in general be divided in two distinct classes: detection limits and quantitation limits. Detection limits refer to a minimum concentration of an analyte that can be measured above the instrument background noise. On the other hand, quantitation limits refer to a minimum concentration of an analyte that can be measured within specified limits of precision and accuracy. The different types of detection and quantitation limits arise from different methods of calculation and from taking different factors into account. Thomsen et al. (2003) uses the terms limit of detection (LOD) and limit of quantitation (LOQ) which can be assigned to the first and second class, respectively. The LOD is quantified by a relative standard deviation of 33 % and the LOQ by a relative standard deviation of 10 %. The relative standard deviation (RSD) is a commonly used estimate of the precision and is a function of the number of counts collected on a sample. The more counts, the higher the precision and the smaller the RSD.

Besides element concentrations also corresponding RSDs were reported for a number of analyses. For each individual element these results were plotted in a RSD versus concentration diagram (Figure 3.3). The LOD and LOQ per element could be calculated by using the equation of the trendline and the for the LOD and LOQ quantified RSDs, cited above. Calculated LODs and LOQs are reported in Table 3.2. The reliability of the LOD and LOQ depends strongly on the number and distribution of the plotted data. Analytical results below the LOD were removed and for the structural formula calculations replaced with zero. Results between the LOD and LOQ are less certain than results above the LOQ and should therefore be interpreted with some caution.

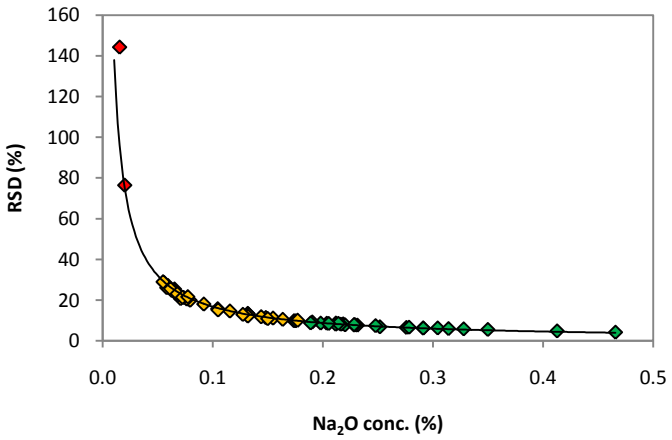

Figure 3.3 Precision, expressed as the relative standard deviation (RSD), as a function of the Na_2O concentration. The limit of detection (LOD) is quantified by a RSD of 33 % and the limit of quantitation (LOQ) by a RSD of 10 % (Thomsen et al., 2003). Analytical results below the LOD (red) are removed. Results between the LOD and LOQ (yellow) are less certain than the results above the LOQ (green).

Table 3.2 Limit of detection (LOD) and limit of quantitation (LOQ) for the elements analysed by electron microprobe. The LOD and LOQ for Ni cannot be determined.

	LOD (wt%)	LOQ (wt%)
SiO_2	45 ppm	453 ppm
Al_2O_3	0.02	0.13
Na_2O	0.05	0.17
K_2O	26 ppm	291 ppm
MgO	0.03	0.14
CaO	0.02	0.10
TiO_2	0.02	0.15
Cr_2O_3	0.03	0.11
MnO	0.09	0.36
FeO	0.03	0.26
P_2O_5	0.13	0.46
SO_3	0.05	0.20
F	0.44	1.46
Cl	0.02	0.06

For the element Ni it was not possible to determine the LOD and LOQ, because for only one analysis a RSD (of 111 %) was reported. The highest measured Ni concentration was about 2.4 times higher than the Ni concentration with the RSD of 111 %. For the other 14 analysed elements the LOD was always more than 3.3 times higher than the concentration with a RSD of 111 %. Based on this all Ni results were assumed to be below the LOD.

3.4.2 Structural formula and major component calculations

The inability of the electron microprobe to distinguish between ferrous iron (Fe^{2+}) and ferric iron (Fe^{3+}) presents a problem. For mica there is no satisfactory procedure to estimate the proportion of ferrous and ferric iron. Some authors (Dalla Torre et al., 1996 and Cathelineau & Izquierdo, 1988) have proposed methods based on certain specific assumptions. Unfortunately, these assumptions do not hold for the analyses used in the present study. Other authors (references in Cathelineau & Izquierdo, 1988) use hypothetical Fe^{2+}/Fe^{3+} ratios, but their choice is arbitrary and therefore not considered. As the white mica did not contain much iron the assumptions $Fe^{2+} = Fe_{total}$ and $Fe^{3+} = Fe_{total}$ yielded very similar results. Therefore, as a first approximation Fe was assumed to be divalent for the structural formula calculations. However, it should be clear that this assumption implicates that it was impossible to assess the ferrimuscovite substitution.

In principle the above valence problem for Fe is also applicable to the elements Mn and Ti (Rieder, 2001). In the present study Mn was assumed to be divalent and Ti to be tetravalent, but these assumptions were arbitrary. However, for Ti and especially Mn this valence problem was less problematic as for Fe, because of the very low quantities in which these two elements were present in the white mica.

Rieder et al. (1998) recommends that when there is no determination of H_2O, as in electron microprobe analyses, an idealised anion group must be assumed. The structural formulae have therefore been calculated on the basis of 22 oxygens (anhydrous basis). All the Si was assigned to the tertrahedral sheet and the number of tetrahedral atoms per formula is then brought to eight using Al.

The remainder of the Al was assigned to the octahedral sheet, as well as Mg, Fe, Ti, Mn, Cr and Ni. All the K, Na and Ca was assigned to the interlayer.

Seven components, which describe the white mica composition of our seven sericite altered samples as completely as possible, were chosen for major component calculations. The end-members are listed below together with the chemical formula.

- Muscovite (Ms) $K_2Al_4[Al_2Si_6O_{20}](OH)_4$
- Paragonite (Pg) $Na_2Al_4[Al_2Si_6O_{20}](OH)_4$
- Margarite (Mrg) $Ca_2Al_4[Al_4Si_4O_{20}](OH)_4$
- Fe^{2+}-aluminoceladonite (Fe^{2+}Al-Cel) $K_2Al_2Fe^{2+}{}_2[Si_8O_{20}](OH)_4$
- Mg-aluminoceladonite (MgAl-Cel) $K_2Al_2Mg_2[Si_8O_{20}](OH)_4$
- Pyrophyllite (Prl) $Al_4[Si_8O_{20}](OH)_4$
- Biotite (Bt) $K_2Fe^{2+}{}_3Mg_3[Al_2Si_6O_{20}](OH)_4$

Mineral abbreviations closely follow the recommendations of Siivola & Schmid (2007). A homemade vector program, written in the vector-based program MATLAB (Appendix 2), was used to find the ratio of major components which gave the best fit to the calculated structural formula. The program was designed in such way that firstly, none of the major components ratios was negative. Secondly, each value of the constituents in the computed chemical formula never exceeded the value in the calculated chemical formula.

3.4.3 Selection of valid white mica compositions

Not all the calculated structural formulae represented valid white mica compositions. One of the reasons for this problem was the very fine-grained nature of the sericite (Figure 3.4). Analysing at the edges of mineral grains was avoided as far as possible, but it cannot be excluded that analyses were still ‘contaminated’ by other surrounding minerals like quartz. In order to exclude such analyses from

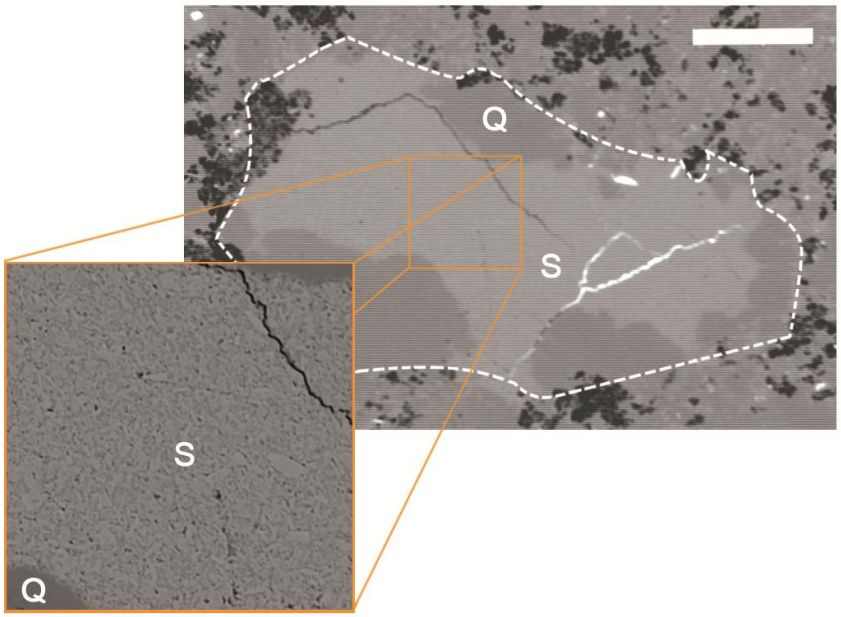

Figure 3.4 Backscattered electron image of an altered subhedral phenocryst. The primary mineralogy of the phenocryst is completely replaced by sericite (S) and quartz (Q). Black areas represent holes. The inset shows clearly the very fine-grained nature of the sericite. Scale bar = 250 µm.

further interpretation a number of criteria had been established. These criteria were consistent with the white mica structure. For any needed chemical and structural information on white mica the reader is referred to section 6.2.

- The number of Si atoms p.f.u. lies between 4 and 8.
- The sum of Si and Al in the tetrahedral sheet is not less than 8 atoms p.f.u.
- The total number of trivalent cations in the octahedral sheet does not exceed 4 p.f.u.
- The sum of octahedral cations p.f.u. lies between 4 and 6.
- The interlayer cation number does not exceed 2 p.f.u.
- The Ti number is less than 0.4 atoms p.f.u. Only in rocks subjected to high T and very high P the Ti content rises to levels of 0.36 to 0.56 atoms p.f.u. (Guidotti & Sassi, 1998a, 1998b, and references therein). These conditions are not applicable to the rock samples used in the present study and therefore a limit of 0.4 Ti atoms p.f.u. is appropriate.

Analyses that fail to meet one or more of these criteria were excluded from further interpretation. In total 62 out of the 264 electron microprobe analyses were excluded as not representing valid white mica compositions.

3.5 Laser ablation ICP-MS analyses

Trace element concentrations in white mica were determined by laser ablation ICP-MS at Utrecht University, The Netherlands. Analyses were carried out on thin sections using a 193 nm ArF excimer laser ablation system of the type MicroLas GeoLas 200Q in combination with a quadrupole ICP-MS of the type Micromass Platform ICP. White mica was selected by using a Zeiss petrographic microscope attached to the laser ablation ICP-MS instrument. The carbon coating on the thin sections from electron microprobe analyses was removed prior to the laser ablation ICP-MS analyses by cleaning with ultrapure acetone. Ablation was performed at a fixed point with a pulse energy of 72 mJ and a laser pulse repetition rate of 10 Hz. The ablation crater diameter was 120 µm except for the analyses performed on thin section p10 which was 60 µm. The carrier gas flow was 0.40 l/min Ar and 0.45 l/min He mixed after the ablation cell.

Each analysis consisted of sequential measuring the following isotopes: ^{24}Mg, ^{25}Mg, ^{26}Mg, ^{27}Al, ^{43}Ca, ^{44}Ca, ^{51}V, ^{52}Cr, ^{60}Ni, ^{85}Rb, ^{88}Sr, ^{89}Y, ^{90}Zr, ^{93}Nb, ^{133}Cs, ^{137}Ba, ^{139}La, ^{140}Ce, ^{141}Pr, ^{143}Nd, ^{147}Sm, ^{149}Sm, ^{151}Eu, ^{157}Gd, ^{161}Dy, ^{163}Dy, ^{166}Er, ^{167}Er, ^{172}Yb, ^{175}Lu, ^{178}Hf and ^{181}Ta. Quantitative results were obtained using NIST reference glass SRM 612 as the calibration standard with element concentrations taken from the compilation by Pearce et al. (1997) and Al as the internal standard element. Al_2O_3 concentrations in white mica were determined previously by electron microprobe analyses (see Section 3.4) and for each thin section the average white mica-Al concentration of that thin section is used. MPI-DING reference glass T1-G served as a secondary standard. The data reduction program GLITTER allowed for the rapid selection of background and signal interval (Van Achterbergh et al., 2001). Laser ablation ICP-MS results are available on the enclosed CD-ROM through the Excel document *Laser ablation ICP-MS analyses*.

3.5.1 Assessment of sample spot homogeneity

Concentrations of trace elements, and especially rare earth elements, are very low in white mica. Therefore, a sufficiently large laser ablation crater size diameter was required to obtain data with a high degree of confidence. However, this immediately possessed a problem for the very fine-grained

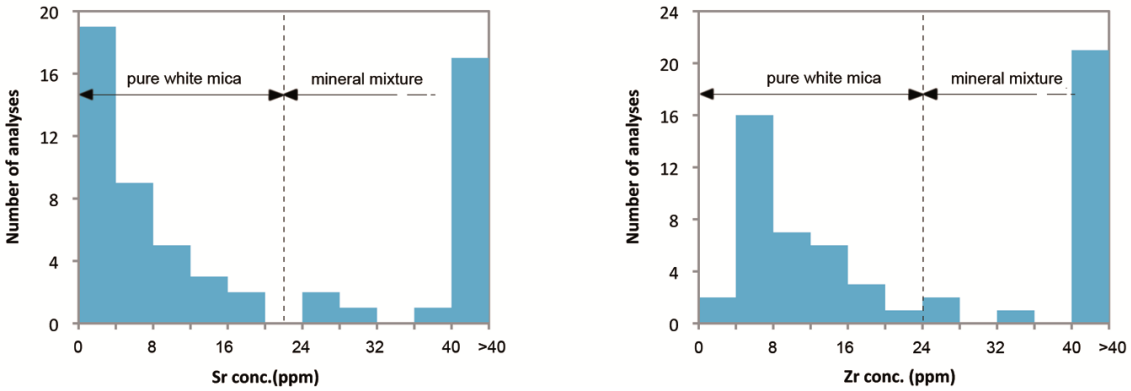

Figure 3.5 Histograms of concentration distribution of the elements Sr and Zr. The extremely positive skweness of the concentration distribution with maximum concentrations up to 0.5 weight % are assumed to result from sample spot heterogeneity.

white mica of the Panorama district. Petrographic examination of the thin sections revealed that there is a risk that besides white mica also other minerals like quartz and iron oxides would be ablated by the laser, resulting in sample spot heterogeneity. Sample spot heterogeneity introduces two sources of uncertainty. First, the applied internal standard concentration is not correct and consequently the laser ablation ICP-MS results do not represent absolute values. Secondly, the results are not representative for white mica. Therefore, without a thorough assessment of sample spot homogeneity, interpretation of the laser ablation ICP-MS results will lead to meaningless conclusions.

In the literature, there is not much information about the compositional range of trace element concentrations in white mica. Fleet (2003) summarises the major element composition of dozens of white mica samples. Only for a few samples also concentrations for the trace elements V, Cr, Ni, Rb and Ba are reported. Compared with these reported concentrations, none of the obtained laser ablation ICP-MS values could be regarded as being anomalous. As a next step, a more detailed study on the laser ablation ICP-MS results was conducted. Figure 3.5 shows the histogram of concentration distribution for the elements Sr and Zr. Concentrations for these two elements were all above the LOQ and consequently represent quantitative results with a high degree of confidence. Both histograms

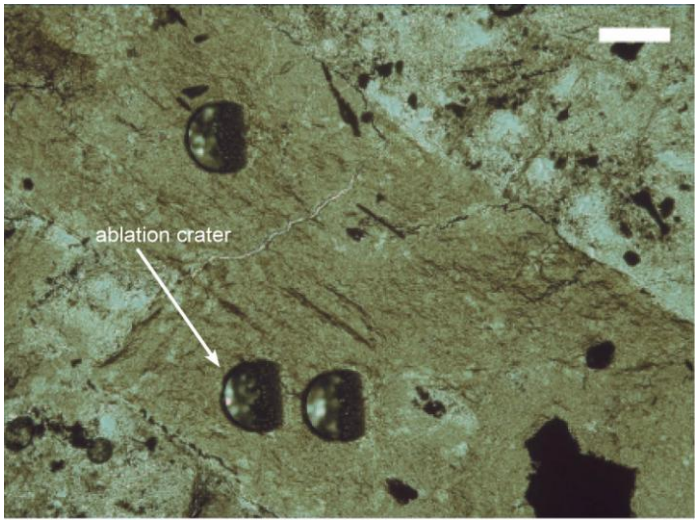

Figure 3.6 Photomicrograph (plane polarised light) of a sericitic altered phenocryst with clearly visible three laser ablation craters. The phenocryst shows patches of dark brown Fe-oxides throughout. The laser ablation ICP-MS analyses corresponding to these ablation craters have been rejected as representing a mineral mixture of sericite and Fe-oxides. Scale bar = 120 µm.

show an extremely positively skewed distribution with maximum concentrations up to 0.5 weight %. It was assumed that low Sr and Zr abundances are indicative for pure white mica, while higher abundances represented mineral mixtures as a result of sample spot heterogeneity. This statement had been thoroughly verified and confirmed by checking lab notes, careful petrographic examination of the ablation crater (Figure 3.6) and reassessment of the time-resolved signal recorded by the ICP-MS during ablation. A threshold value of 22 ppm for Sr and 24 ppm for Zr had been chosen to discriminate pure white mica analyses from mineral mixture analyses (Figure 3.5). Analyses with one or both of the concentrations for the elements Sr and Zr above the threshold were rejected as representing mineral mixtures as a result of sample spot heterogeneity. Of the 60 laser ablation ICP-MS analyses performed on white mica only 29 analyses were regarded as representing pure white mica and only these analyses were used for further processing and interpretation.

3.5.2 Data quality

One of the analytical difficulties with laser ablation ICP-MS is the presence of interferences in the sample analysis affecting the accuracy of certain element concentrations. When multiple isotopes of an element were measured, the results of the isotope that was least affected by potential interferences were used for further processing and interpretation i.e. ^{25}Mg, ^{44}Ca, ^{147}Sm, ^{163}Dy and ^{166}Er. The formation of BaO during the ablation results in a significant interference on the ^{151}Eu signal when the Ba:Eu ratio is more than 200:1 (Jarvis, 1989). White mica in the study area was characterised by extremely high Ba:Eu ratios that exceed 2500:1. Therefore, the obtained Eu results should be rejected.

Results below the minimum detection limit (MDL) were excluded from further study, as the analyte signal was not significantly different from the background signal. The MDL at the 99 % confidence level was calculated for each element within each individual analysis by the GLITTER software package using Poisson counting statistics on the gas blank signal (Van Achterbergh et al., 2001). The LOQ was simply calculated by multiplying the MDL by 3.3. MDLs of the trace elements were very low and typically in the range of 0.01–1 ppm. Rare earth element concentrations in white mica exceeded only sporadically the LOQ and were in general even below the MDL. Eu is an exception to this, but that is an artefact of the earlier explained interference with BaO. Element concentrations of Mg, Ca, V, Rb, Sr, Zr, Cs, Ba, Hf and Ta in white mica were all above the LOQ and can be used with confidence.

The precision and accuracy of the laser ablation ICP-MS analyses were assessed by measuring the MPI-DING reference glass T1-G six times during the operating period. Precision refers to how closely individual measurements agree with each other and can be defined by the relative standard deviation (RSD):

$$RSD^i = 100 \cdot \frac{s^i}{\bar{x}^i}$$

where s^i is the standard deviation of element i in the samples analysed, and $\bar{x}^i$ is the sample mean. Accuracy is a measure of how close analytical data lie to the 'true' values and is expressed as a positive or negative percentage difference:

$$A^i = 100 \cdot \frac{(C_a^i - C_m^i)}{C_a^i}$$

where $C_a{}^i$ is the 'true' or accepted proportion of element i and $C_m{}^i$ is the measured proportion of element i. Reference glass results are all above the LOQ. The precision ranged between 5–15 % RSD,

but could increase to 25 % RSD for concentrations below the 10 ppm. Comparison of the measured concentrations with reference concentrations (Jochum et al., 2006) showed poor agreement with for individual analyses deviations of more than 20 %. This poor accuracy cannot solely be attributed to very low concentrations, as for example also for the element Zr, with a reference concentration of 144 ± 2 ppm (1 σ), deviations in the range of 3–24 % were reported. In general, the deviations showed no consistent trend, except for the elements Mg, Ca and Gd where the measured concentrations of the reference glass were consistently too high by on average 40 %. Most probably that was the due to a calibration error for these three elements. With such a poor accuracy, laser ablation ICP-MS results should not be compared with the literature.

To conclude, the obtained laser ablation ICP-MS results should be interpreted with much caution. Sample spot heterogeneity and element interferences have proven to be a problem. Quantitative results with a high degree of confidence were not always obtained. Furthermore, the accuracy of the results is very poor and at concentrations below the 10 ppm also the precision.

3.6 Whole-rock geochemical analyses

The whole-rock geochemical analyses were conducted by Activation Laboratory Inc. (Actlabs). The following information on sample preparation, digestion procedures and analytical procedures is based on information provided on the website of Actlabs (www.actlabs.com). The 11 samples were first crushed, split and pulverised using mild steel. Mild steel is the best option for low contamination with only Fe added (up to 0.2%). To avoid cross-contamination cleaner sand is used after each sample.

Oxides and trace element concentrations were determined by lithium metaborate/tetraborate fusion ICP. Samples were mixed with a flux of lithium metaborate and lithium tetraborate and fused in an induction furnace. The molten melt was immediately poured into a solution of 5% nitric acid and mixed continuously until completely dissolved (~30 minutes). The samples were run for major oxides and the trace elements Be, Sc, V, Sr, Y, Zr and Ba on an ICP-OES. For the determination of the other trace elements, as well as the already analysed elements V, Sr, Y, Zr and Ba, the sample solution was further diluted. Following this the samples were analysed on an ICP-MS.

The 8 base metal elements S, Ni, Cu, Zn, Ag, Cd, Pb and Bi were determined by multiacid digestion ICP. A 25 g sample was digested with four acids beginning with hydrofluoric acid, followed by a mixture of nitric and perchloric acids. Samples were heated to dryness and brought back into solution using hydrochloric acid. Only sulphide sulphur will be solubilised. Zircon, monazite, sphene, gahnite, chromite. cassiterite, rutile and barite may only partially solubilised. After digestion samples were analysed on an ICP-OES.

The ferrous iron content (FeO) was determined through titration, using a cold acid digestion of ammonium metavanadate, sulphuric acid and hydrofluoric acid in an open system. This cold digestion will dissolve silicates and some sulphides. Pyrite may not be totally dissolved. Ferrous ammonium sulphate was added after digestion and potassium dichromate was the titrating agent. When titrating the endpoint was determined by colour.

The whole-rock geochemical lab results of the 11 samples are available on the enclosed CD-ROM through the Excel document *Whole-rock geochemical analyses*. The reported loss on ignition (LOI)

values are not corrected for iron oxidation. During the LOI process oxidation of ferrous iron to ferric iron can produce a weight gain, partly offsetting the LOI values. Correction assumes that all ferrous iron is completely oxidised and, as mentioned by Potts (1987, *cited in* Gifkins et al. 2005), this is not reasonable to assume.

3.6.1 Data quality

For a good interpretation of the obtained data reliable and accurate analytical measurements are a prerequisite. To assess the quality of the analytical results certified reference materials, a replicate and a method blank were analysed parallel with the samples. The method blank is an indicator of possible contamination introduced during the laboratory work. It contains no added analyte, only the same solvents, reagents, etc. used for the preparation of the samples. The method blank is prepared and analysed simultaneously with and exactly as the other samples. The results of the method blank were below the detection limit for all elements and oxides, except for SiO_2, $Fe_{(total)}$ and K_2O. Reported concentrations for these 3 oxides were respectively 0.02 %, 0.01 % and 0.01 %. The results reveal that some contamination has taken place in the laboratory. However, the level of contamination is so low that the results are still usable. As clearly explained by Smith (2001), the absence of a clear cause for the contamination (e.g. a contaminated acid or a piece of dust falling into the sample), does not make it appropriate to treat the contamination as a systematic event. Therefore, the method blank results were not subtracted from the sample results.

The relative percent difference (RPD) is a measure of precision and is formulated by the following equation:

$$RPD = \frac{|X_1 - X_2|}{X_{ave}} \cdot 100$$

where X_1 is the concentration of the first measurement, X_2 is the concentration of the replicate measurement and X_{ave} the average concentration of X_1 and X_2. The precision for concentrations equal or greater than 20 times the detection limit were generally better than 10 % RPD for the trace elements and even better than 1 % RPD for the oxides. RPD of more than 10 % were only reported for concentrations close to the detection limit. The obtained replicate results of the rare earth elements always agreed within 5 % RPD.

Actlabs has only analysed certified reference materials. The true or accepted concentrations and accompanying uncertainties (i.e. standard deviations) for these certified reference materials are reported in the literature. The accuracy can be expressed as the normalised standard deviation (σ_n), which is defined as the concentration difference between the measured and accepted concentration of the reference material, normalized to the standard deviation of the accepted concentration:

$$\sigma_n = \frac{(C_m - C_a)}{\sigma_a}$$

where C_m is the measured concentration, C_a is the accepted concentration and σ_a the standard deviation of C_m. For a selection of elements the results are presented diagrammatically in Figure 3.7. To assess the accuracy a z-test was performed for each element with a confidence interval of 50 % (= 0.67 σ). Results of these tests show that the measured concentrations of the certified reference materials for P_2O_5, As, Mo, Cd, W and Bi differed significantly from the accepted concentrations. Analytical results of these 6 elements are therefore assumed to be inaccurate and should not be compared with results

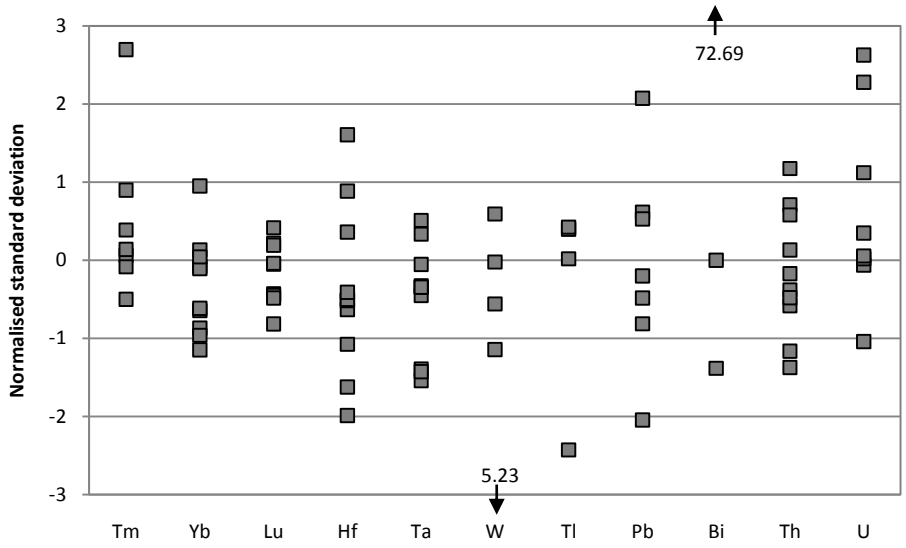

Figure 3.7 Diagrammatic representation of the normalised standard deviation, which is an expression of the precision, for a selection of elements.

reported in the literature. However, relative differences between the samples can still be interpreted, as the precision is satisfactory.

In summary, the quality of the obtained data is good. The level of contamination in the laboratory was minimal. Only concentrations close to the detection limit should be interpreted with caution because they may not be precise. Also the concentrations of P2O5, As, Mo, Cd, W and Bi have to be interpreted with caution as they were not accurate. The other obtained data can be used with confidence.

Chapter 4: Short wavelength infrared spectral analysis of the 11 collected rock samples

4.1 Introduction

The wavelength position of the main Al-OH absorption feature of white mica varies with composition between 2180–2228 nm (Pontual et al., 1997b). The fossil Archaean submarine hydrothermal system of the Panorama district is an excellent area to study these distinct wavelength variations at around 2200 nm. Studies from this area show a systematic variation in the wavelength position of the absorption feature near 2200 nm of white mica, related to fossil submarine hydrothermal fluid convection (Cudahy et al., 2000; Cudahy & Quigley, 2004; Van Ruitenbeek, 2007; Van Ruitenbeek et al., 2005, 2006). Van Ruitenbeek et al. (2006) created two images for the Panorama district using airborne derived reflectance spectra. An image representing the probability, ranging from 0 to 1, of white mica being present (Figure 4.1A) and an image showing the wavelength position of the

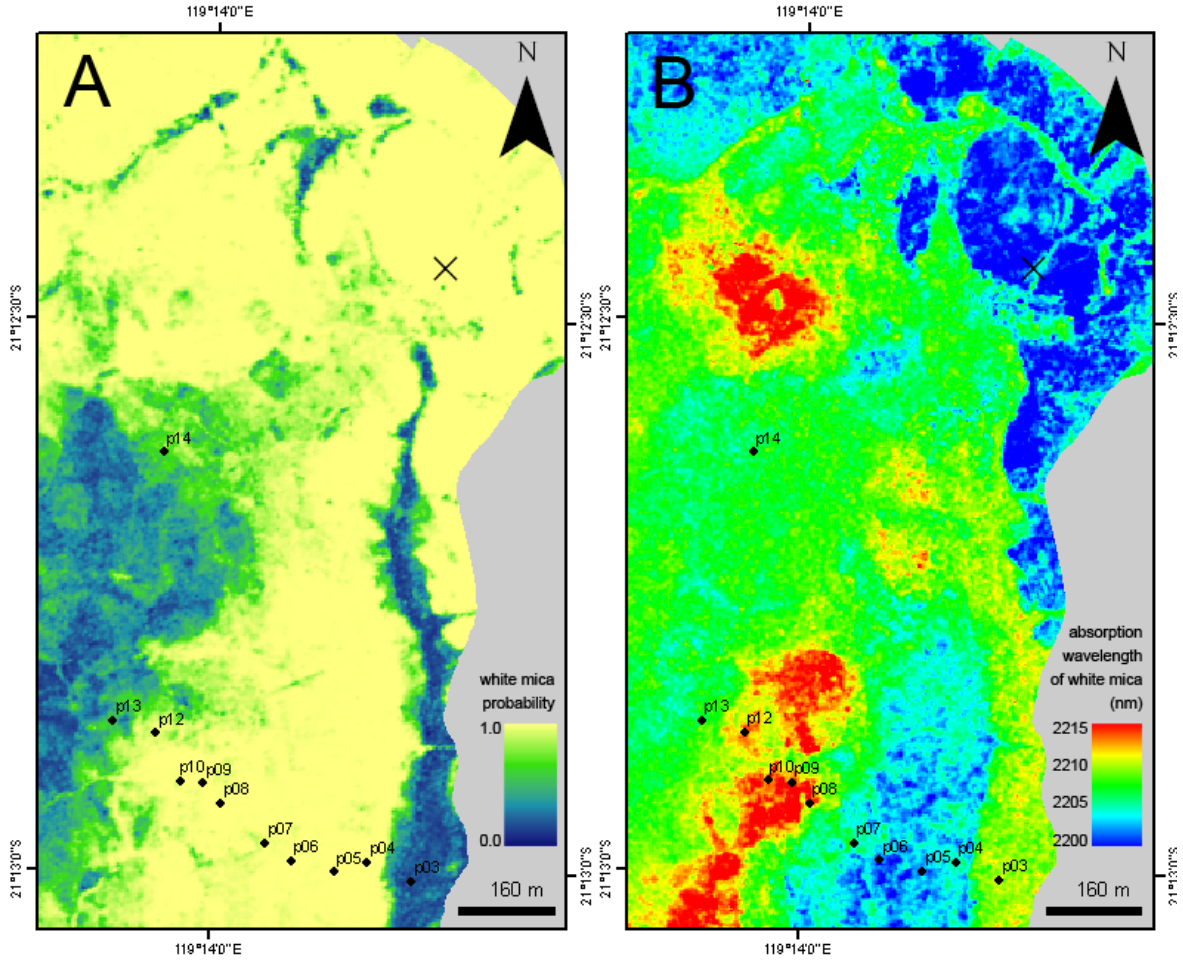

Figure 4.1 (A) Image representing the probability of white mica being present for the study area (after Van Ruitenbeek et al., 2006). (B) Image showing the wavelength position of the absorption feature near 2200 nm of white mica for the study area (after Van Ruitenbeek et al., 2006). Both images are created using reflectance spectra derived from airborne HyMap data. X marks the Kangaroo Caves VMS deposit.

absorption feature near 2200 nm of white mica (Figure 4.1B). According to these images the transect of the 11 collected rock samples intersects with a white mica rich area of short absorption wavelengths (<2205 nm) and a white mica rich area of long absorption wavelengths (>2208 nm). Reflectance spectroscopy is used to verify the results of Figure 4.1 and determine the wavelength position of the main Al-OH absorption feature of white mica for the white mica rich samples.

4.2 Spectral characteristics of white mica and chlorite

The information in the following section is largely based on the spectrum guides of Pontual et al. (1997a, 1997b). The common molecular bonds OH, H_2O, CO_3, NH_4, Al-OH, Fe-OH and Mg-OH produce diagnostic absorption features in the SWIR region (Figure 4.2). The combination of these absorption features allows the identification of many mineral groups including phyllosilicates (e.g. white mica and chlorite), carbonates and sulphates. White mica spectra are characterised by a strong, sharply defined single Al-OH absorption feature between 2180 and 2228 nm and weaker secondary Al-OH absorption features near 2344 and 2440 nm (Figure 4.2). Chlorite spectra have diagnostic Fe-OH and Mg-OH absorption features in the ranges of 2235 to 2255 nm and 2320 to 2360 nm, respectively. Mixed assemblages containing both white mica and chlorite produce spectra that have absorption features in all three of the Al-OH, Fe-OH and Mg-OH bands. The proportion of white mica relative to chlorite can be estimated using the white mica alteration index (WMAI). The WMAI is developed by Van Ruitenbeek et al. (2005) and is described in detail in section 3.2.1. The WMAI ranges from 0 to 1 and increases with increasing white mica abundance relative to chlorite. For the "Chlorite > white mica" spectrum in Figure 4.2, in which chlorite dominates the sample over white mica, the WMAI is 0.57. For the converse case in which white mica dominates the sample, the "White mica > chlorite" spectrum, the WMAI is 0.86.

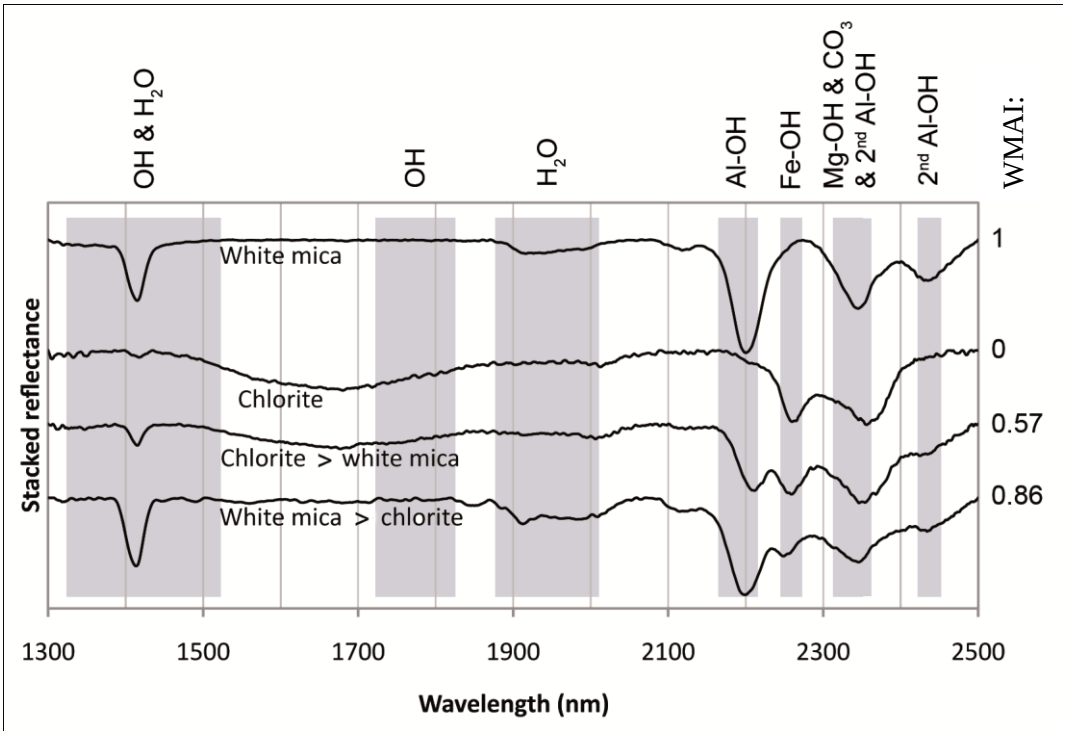

Figure 4.2 Characteristic SWIR absorption features in spectra of white mica, chlorite and mixed assemblages of white mica and chlorite (modified from Pontual et al., 1997a, 1997b). Annotations at right represent the WMAI for each spectrum. See text for explanation.

Carbonate has a diagnostic CO_3 absorption between 2300 and 2360 nm, which coincides with the Mg-OH feature of chlorite and one of the secondary Al-OH features of white mica. Because of this overlap, and because carbonate has a significantly weaker absorption coefficient compared to the phyllosilicates, carbonate tends to be obscured in mixed assemblages containing phyllosilicates. In mixed assemblages with white mica, carbonate can still be recognised by an increase in the relative depth of the secondary Al-OH feature of white mica near 2344 nm compared to the other the secondary Al-OH feature near 2440 nm. Consequently, the "White mica" spectrum in Figure 4.2 contains some carbonate.

4.3 Results and discussion

4.3.1 Interpretation of the field sample laboratory spectra

SWIR reflectance spectra of the 11 collected rock samples are shown in Figure 4.3. For each spectrum the wavelength position and depth of the absorption feature near 2200 nm of white mica is listed in Table 4.1. Except for sample p03, all the spectra have clearly defined absorption features which allows for mineral identification. On the basis of prominent absorption features the following three spectral

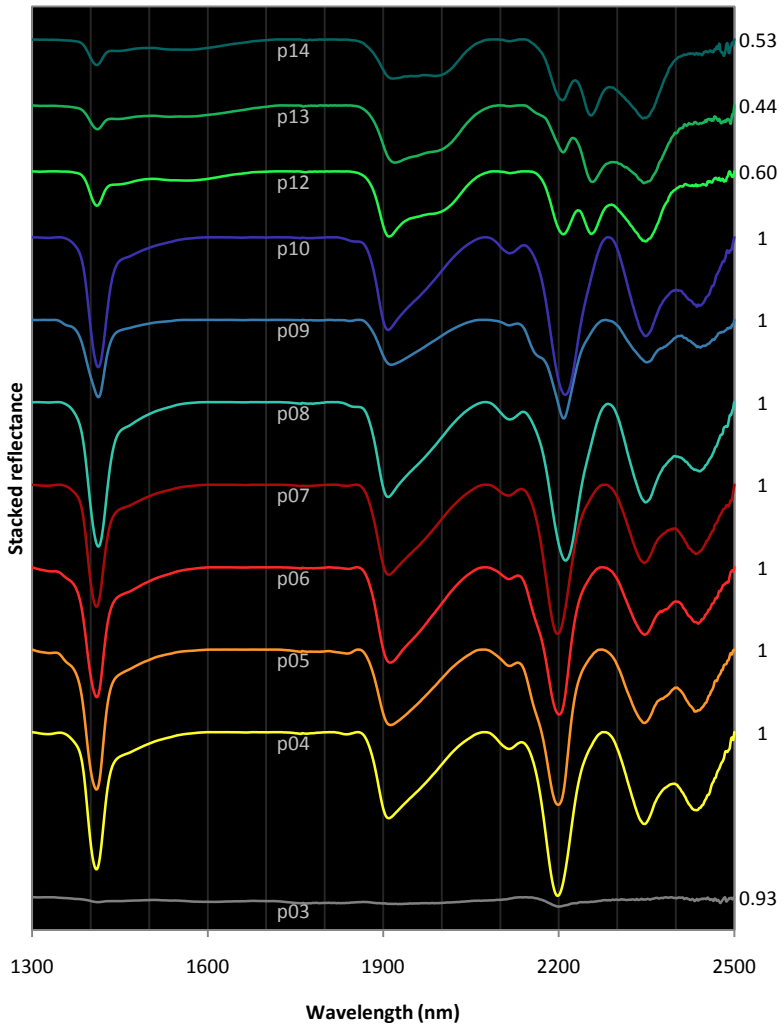

Figure 4.3 SWIR reflectance spectra of the 11 collected rock samples. Annotations at right represent the WMAI for each spectrum.

Table 4.1 Wavelength position and depth of the absorption feature near 2200 nm of white mica for each spectrum.

	λ (nm)	Depth
p03	2199	0.028
p04	2198	0.496
p05	2199	0.470
p06	2201	0.446
p07	2198	0.452
p08	2212	0.480
p09	2208	0.299
p10	2211	0.477
p12	2207	0.190
p13	2207	0.142
p14	2206	0.184

types are represented:

1. Spectra with moderate to high background reflectance and prominent Al-OH absorption features characteristic for white mica. The increase in depth of the absorption near 2344 nm relative to the absorption near 2440 nm could be an indication that in all samples carbonate is present as a minor component. The samples p04 to p10 belong to this spectral type.
2. Flatter, lower reflectance spectra with prominent absorption features in all three of the Al-OH, Fe-OH and Mg-OH bands typical for chlorite in mixtures with white mica. Consequently, these spectra all have an intermediate WMAI. The samples p12 to p14 belong to this spectral type.
3. Low reflectance, noisy spectra without recognisable absorption features. Only the spectrum of sample p03 belongs to this spectral type.

The featureless spectrum of sample p0s can be associated with the intensely silicified unit at the top of the volcanic sequence, termed the Marker Chert. Quartz is a spectral featureless mineral and is consequently devoid of any spectral features in the 1300–2500 nm wavelength range. The very weak absorption feature at 2199 nm can possibly related to the presence of white mica. However, as the secondary Al-OH absorption features of white mica are not apparent the presence of white mica in sample p03 should be confirmed by petrographic work.

The wavelengths of the Al-OH absorption feature of white mica ranges between 2198 and 2212 nm. The spectra can be subdivided into a group of short-wavelength white mica (<2201 nm) and long-wavelength white mica (>2208) (Figure 4.14). The spectra of the samples p04 to p07 belong to the group of short-wavelength white mica and the spectra of the samples p08 to p10 belong to the group of long-wavelength white mica. The spectra of the samples p12 to p14 are omitted from this subdivision as high amounts of chlorite tend the shift the wavelength position of white mica.

There are spectral indications that of the white-mica spectra p04 to p10 the sample p09 contains weathering products. Weathering in the Panorama district is characterised by the presence of the clay minerals halloysite and kaolinite (Van Ruitenbeek et al., 2006). The 2200 nm absorption feature of both halloysite and kaolinite is accompanied by a well-known shoulder near 2160 nm (Clark et al., 1990). The reflectance spectrum of sample p09 shows a clear indication of such shoulder (Figure 4.3). Furthermore, the presence of an additional inflection point at around 1360 nm in the spectrum of sample p09 (not shown) can also be attributed to the presence of the minerals halloysite and kaolinite

(Clark et al., 1990). As pointed out Suryantini et al. (2005) weathering shifts the wavelength position of the 2200 nm absorption feature of white mica. For long-wavelength white mica the absorption shifts towards ~2204 nm. Consequently, with a wavelength position of 2208 nm for sample p09 the degree of weathering of sample p09 is regarded as being low. Nevertheless, care should be taken in interpreting the wavelength position of the main Al-OH absorption feature of sample p09.

4.3.2 Comparison of field sample laboratory spectra with airborne spectra

The results of the SWIR analysis can be used to check the agreement between the field sample laboratory spectra and the parameters presented in Figure 4.1. The white mica probability of each sample location is compared with the absorption depth of the 2200 nm feature obtained from each rock sample (Table 4.1). This absorption depth is however only a semi-quantitative measure for the presence of white mica, as for example opaque minerals tend to suppress spectral features. The absorption wavelength of the 2200 nm feature of white mica of each sample location can be quantitatively compared the absorption wavelengths obtained from each rock sample. The results of these comparisons are shown in Figure 4.4. These graphs will always be accompanied with a certain amount of random scattering introduced by:

- A difference in the object size. Pixel values in Figure 4.1 represent an area of 15 by 15 m.
- The presence of vegetation and weathering material at the ground surface.
- The use of hull corrected reflectance spectra in this study. The parameters in Figure 4.1 are based on uncorrected reflectance spectra.

Despite these introduced errors the figures show a satisfying fit. Furthermore, the subdivision of short- and long-wavelength white mica based on the rock samples is in agreement with the transition for the white mica rich area from short absorption wavelengths to long absorption wavelengths as shown in Figure 4.1. Therefore, patterns in Figure 4.1 can be used for further interpretation.

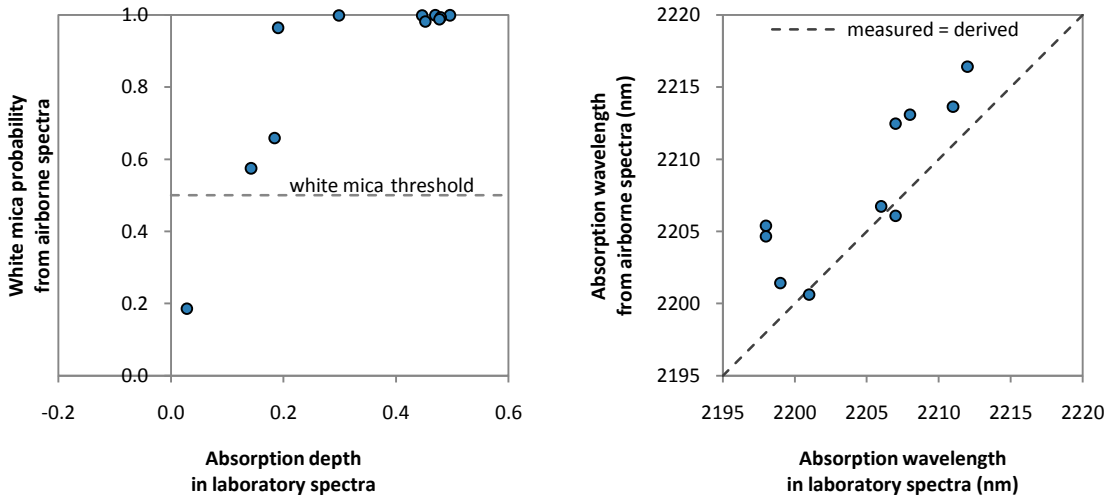

Figure 4.4 (A) Measured absorption depth of field sample laboratory spectra versus the white mica probability derived from Figure 4.1. As a threshold for white mica being present Van Ruitenbeek et al. (2006) used a value of 0.5. (B) Measured absorption wavelength of field sample laboratory spectra versus derived absorption wavelength from Figure 4.1. Sample p03 is omitted from this graph as it does not contain white mica.

Chapter 5: Thin section petrology

5.1 Introduction

In the previous reflectance spectroscopy chapter the samples p04 to p10 were recognized as white mica rich samples. This interpretation of the reflectance spectra is validated using thin section petrology. This chapter is divided into two parts; the first part, thin section petrography, is the descriptive part and focus on mineral composition and textures in the thin sections. The second part, thin section petrogenesis, is the interpretative part.

5.2 Thin section petrography

The 11 thin sections have already been studied by Kim Hein in 2005. Her unpublished petrologic report has served as a very useful guide to both the descriptive and interpretative petrology of the thin sections presented in this chapter. Presented estimates of the alteration intensity at the end of each subsection are after Gifkins et al. (2005) and are primarily based on the completeness of replacement.

5.2.1 Section p03

The section consists of irregular, sub-parallel, wavy laminae varying in thickness between 30 μm and 2.2 mm (Figure 5.1). Laminae are very fine grained and defined by:

- Anhedral granular quartz (rare).
- Anhedral quartz, sericite, and opaque minerals; including limonite. The micron-sized nature of both quartz and sericite makes it difficult to asses the exact proportions of these 2 minerals. Sericite occurs as elongated clots of micron-sized crystals with an orientation parallel to the lamina and shows simultaneous extinction throughout the whole lamina (Figure 5.1). Limonite occurs as a red staining with a preferred orientation parallel to the lamina.
- Anhedral quartz and opaque minerals; including limonite. The proportions differ for each lamina. Limonite occurs as a red staining to discrete rounded crystals. Some of the laminae contain numerous rounded to elongated clasts of polycrystalline quartz.

The section is crosscut by several quartz veins both parallel and perpendicular to the lamination. Quartz veins parallel to the lamination are only restricted to certain laminae and have diameters of approximately 10 to 30 μm, while quartz veins perpendicular to the lamination can reach diameters up to 0.2 mm. Furthermore, a millimetre-scale slump texture is evident parallel to the lamination. Exhibits the section an irregular erosional surface cutting into the underlying laminae forming angular contacts and a small normal fault with an displacement of approximately 0.3 mm in the plane of view.

Relict textures: wavy-laminar; slump
Alteration textures: replacement
Alteration type: sericitic, silicic
Alteration intensity: weak

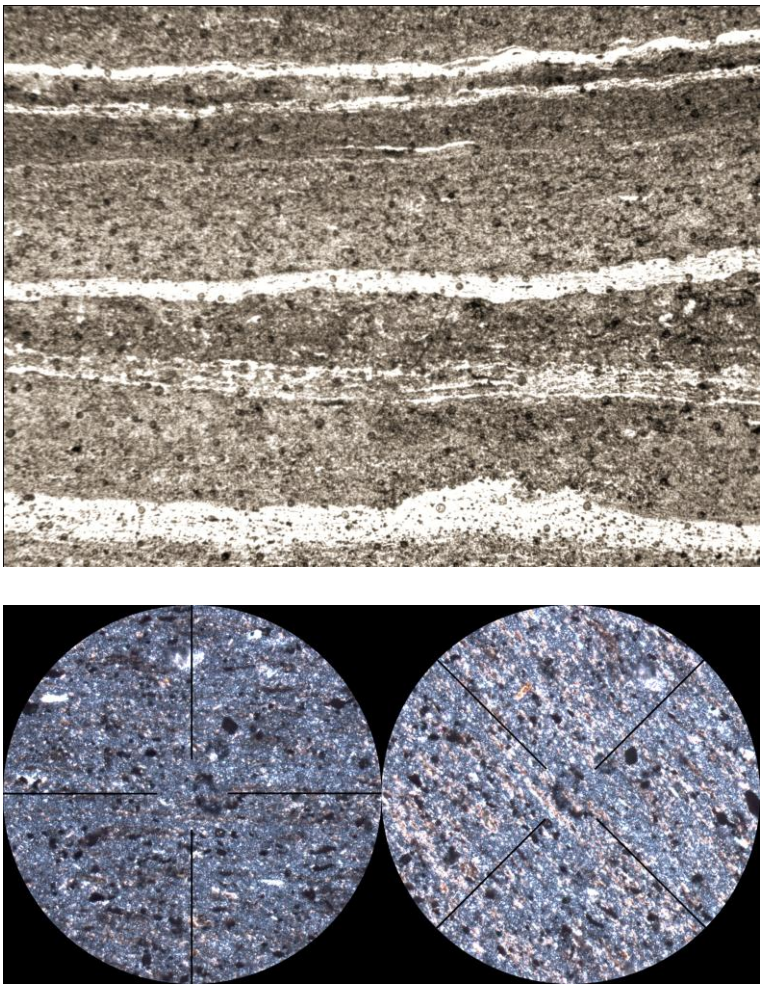

Figure 5.1 (upper) PPL photomicrograph of section p03 showing the wavy-laminar texture of the chert. FOV: 5 mm. (lower) XPL photomicrographs of section p03. By rotating the stage sericite shows an almost complete extinction throughout the lamina.

5.2.2 Section p04

The sericitic altered section consists of amygdales, phenocrysts and glomerocrysts set in a fine-grained groundmass. Alteration is moderate, selective, and relict textures are well preserved.

The amygdales are well-rounded to angular shaped and are up to 5 mm in diameter (Figure 5.2). They comprise about 20–25 % of the thin section. The former vesicles show all complete infilling by, in general, very fine-grained to cryptocrystalline quartz, or by, occasionally, an aggregate of small quartz crystals. The cryptocrystalline quartz has a (concentric zoned) radial-fibrous structure showing sweeping extinction when rotated. Straight boundaries exist between adjacent growths of cryptocrystalline quartz, and triple points where three growths meet. It is not clear whether the infilling is late-stage magmatic or post-magmatic. All the amygdales have an outer reaction rim of re-equilibrated quartz and a few rosettes of sericite.

Altered phenocrysts up to 3 mm in length are completely replaced by sericite (Figure 5.2). Euhedral to subhedral crystal outlines are well preserved and the elongated shape suggests that feldspar was the primary mineral. Phenocrysts occur from free-floating crystals to complex intergrowths with quartz and, as interpreted by Brauhart (1999), leucoxene pseudomorphs of primary magnetite crystals.

The fine-grained groundmass is mainly composed of quartz and feldspar. Sericitic alteration of the groundmass is weak and restricted to the rims of feldspar crystals. Deuteric alteration gives the groundmass a hazy appearance.

Relict textures: vesicular/amygdaloidal, porphyritic, glomeroporphyritic
Alteration textures: infill, replacement, recrystallisation
Alteration type: sericitic
Alteration intensity: moderate

5.2.3 Section p05

The section consists of large euhedral and anhedral phenocrysts with diameters up to 5 mm in a fine grained groundmass. Amygdales are not obvious. The section is crosscut by 2 medium scale quartz veins.

Relict phenocryst outlines are sparse, but phenocrysts can still be recognised by the complete alteration to sericite and the high amount of rounded limonite crystals. Phenocrysts up to 5 mm in diameter, but mostly smaller occur form individual crystals to very complex clusters of quartz and subhedral magnetite pseudomorphed by leucoxene (Brauhart, 1999). It is not clear whether the quartz is primary or secondary.

Small laths of feldspar completely replaced by sericite, and interstitial quartz make up the fine-grained groundmass. Irregular shaped, empty dissolution vugs are sparsly present. The groundmass is deuterically altered and contains numerous rounded limonite crystals. Iron oxidation gives the section at some places a yellow stain.

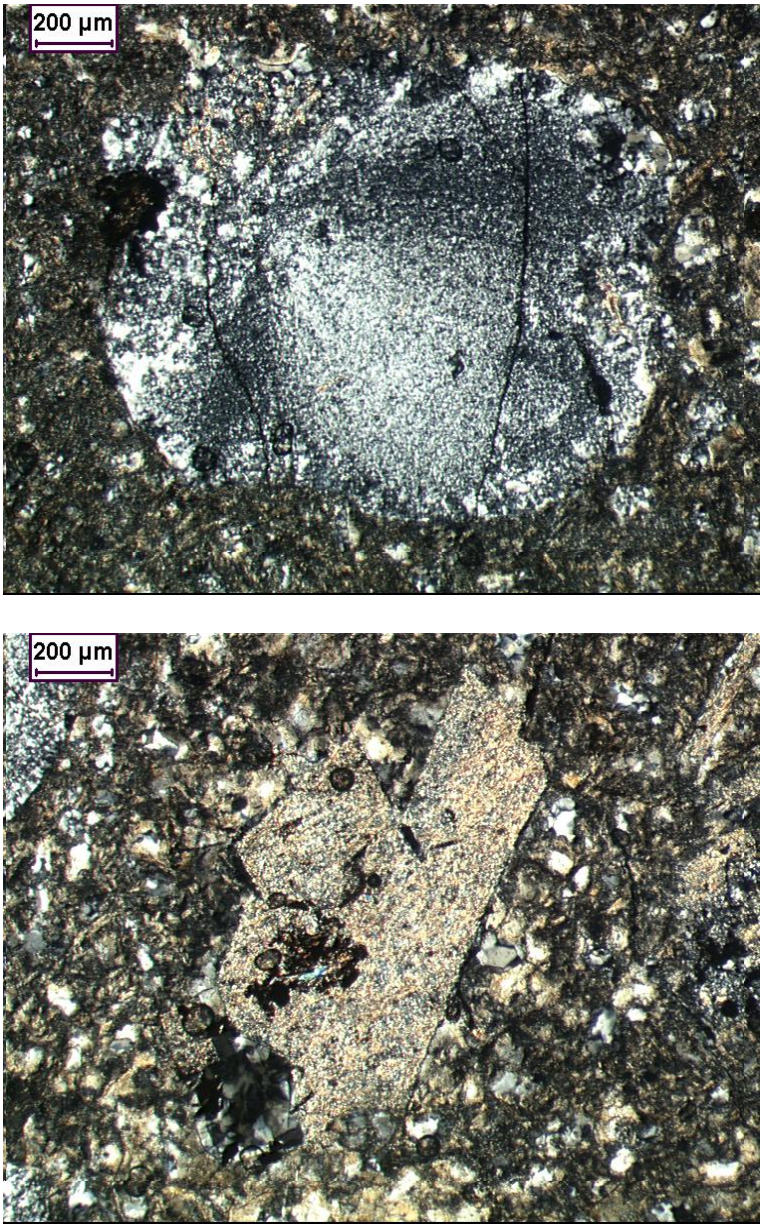

Figure 5.2 XPL photomicrographs of section p04. (Upper) A former vesicle completely infilled by cryptocrystalline quartz showing a sweeping extinction. At the rims of the amygdale the quartz is re-equilibrated. (Lower) A completely sericitic altered phenocryst.

Relict textures: porphyritic, glomeroporphyritic
Alteration textures: replacement, dissolution
Alteration type: sericitic
Alteration intensity: strong

5.2.4 Section p06

The sericitic altered section consists of phenocrysts up to 1 mm in length set in a fine-grained groundmass. Glomerocrysts are not obvious. The euhedral to subhedral phenocrysts are completely altered to sericite and show a discontinuous rim of quartz at the edge of the phenocrysts (Figure 5.3). The quartz is layered and contains quartz with small inclusions in the inner part and fibrous outgrowing quartz with no inclusions at the outer part.

The groundmass is fine-grained and is mainly composed of quartz and sericite after most probably feldspar. Rounded limonite crystals occur throughout the section. Deuteric alteration gives the groundmass a hazy appearance. Leucoxene is a replacement after magnetite (Brauhart, 1999). Dissolution vugs are sparse.

Relict textures: porphyritic
Alteration textures: replacement, dissolution
Alteration type: sericitic
Alteration intensity: strong

5.2.5 Section p07

The strongly sericitic altered section consists of primary phenocrysts and glomerocrysts set in a fine-grained, deuterically altered groundmass composed of crystallites. Alteration structures, such as solution seams and dissolution vugs (Figure 5.3), are present throughout the whole section.

Clusters of transmineral strings occur along regular planes. These clusters consist of discontinuous contraction fractures with an average thickness of 0.1 mm that sometimes form interconnected networks. The contraction fractures show a complete infilling with quartz crystals. A large fracture, only partly visible at the edge of the thin section, with a minimum diameter of 5 mm shows euhedral quartz crystals projecting inwards from the fracture wall (comb texture). The quartz crystals show signs of competitive growth in which the large quartz crystals with a maximum length of 1 mm make up the face. The centre of the fracture has been infilled with small quartz crystals and aggregates of small rounded limonite crystals.

The infilled contraction fractures are crosscut at almost right angles by solution seams of sericite and by very small sericite veinlets. Subsequently, these solution seams and sericite veinlets are crosscut by very small veinlets of opaque minerals.

Relict textures: porphyritic, glomeroporphyritic, contraction, quench
Alteration textures: infill, replacement, dissolution
Alteration type: sericitic
Alteration intensity: strong

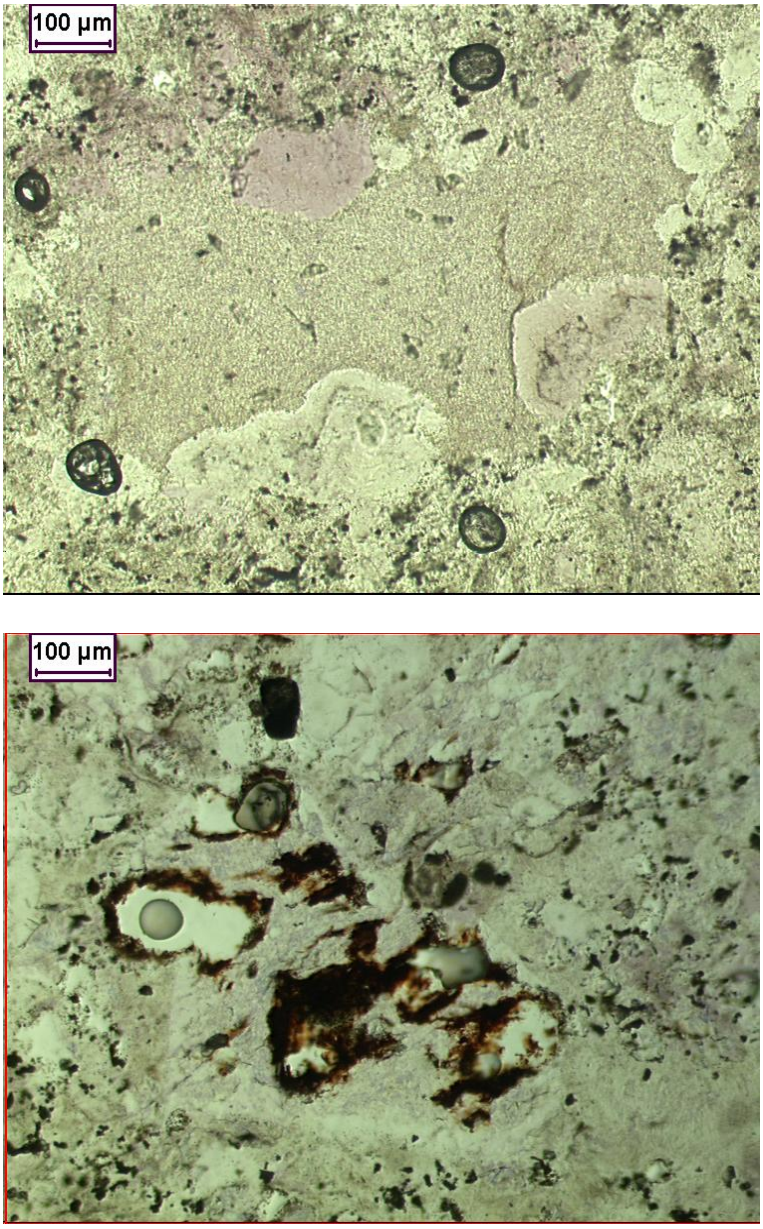

Figure 5.3 (upper) PPL photomicrograph of section p06 showing a completely altered suhhedral phenocryst. At the edge of the phenocryst discontinuous rim of layered quartz is obvious. (lower) PPL photomicrographs of section p07 showing dissolution vugs. The rims of the vugs are marked by iron oxides.

5.2.6 Section p08

The section contains large euhedral to subhedral phenocrysts up to 2 mm in diameter completely altered to sericite. The overall alteration intensity is strong. The section is crosscut by micro-veinlets of micron sized quartz, which in their turn are crosscut by solution seams (Figure 5.4).

The groundmass is composed of crystallites and consists of quartz, the primary mineral feldspar altered to sericite and opaque minerals. The opaque minerals include rutile needles, hematite and goethite. Deuteric alteration is less obvious.

Relict textures: phenocrysts
Alteration textures: replacement, dissolution
Alteration type: sericitic
Alteration intensity: strong

5.2.7 Section p09

Rounded to very angular shaped masses ranging in diameter from 0.1 mm up to 8 mm dominate the section by at least 45 %. The larger masses show a composite layered structure with a roughly concentric outer zone consisting of separate domains of euhedral quartz and sericite and a cryptocrystalline inner zone often containing patches of limonite. In contrast to these larger masses no inner zone is present in the smaller masses. The layered structure could be the result of layered infill of a vesicle or re-equilibriation of the rim of a xenocryst.

The overall texture of the groundmass is fine-grained and has undergone sericitic alteration. Micro-veinlets of opaque minerals crosscut the groundmass and the previously described masses present in the section. Phenocrysts and glomerocrysts are not obvious.

Relict textures: possible amygdales or xenocrysts
Alteration textures: replacement, infill or re-equilibration
Alteration type: sericitic
Alteration intensity: strong

5.2.8 Section p10

This section is of an intensely sericitic altered volcanic rock in which primary features are sparse (Figure 5.4). The fine-grainded groundmass shows radiating patterns indicative for quench of the magma. Solution seems and dissolution occur throughout the section.

The section shows nice cross-cutting relationships. A vein of micron sized quartz crosscuts the section. This vein is in their turn crosscuts by solution seems of sericite. Finally micro-veinlets of opaque minerals are formed.

Relict textures: nil
Alteration textures: replacement, dissolution
Alteration type: sericitic
Alteration intensity: intense

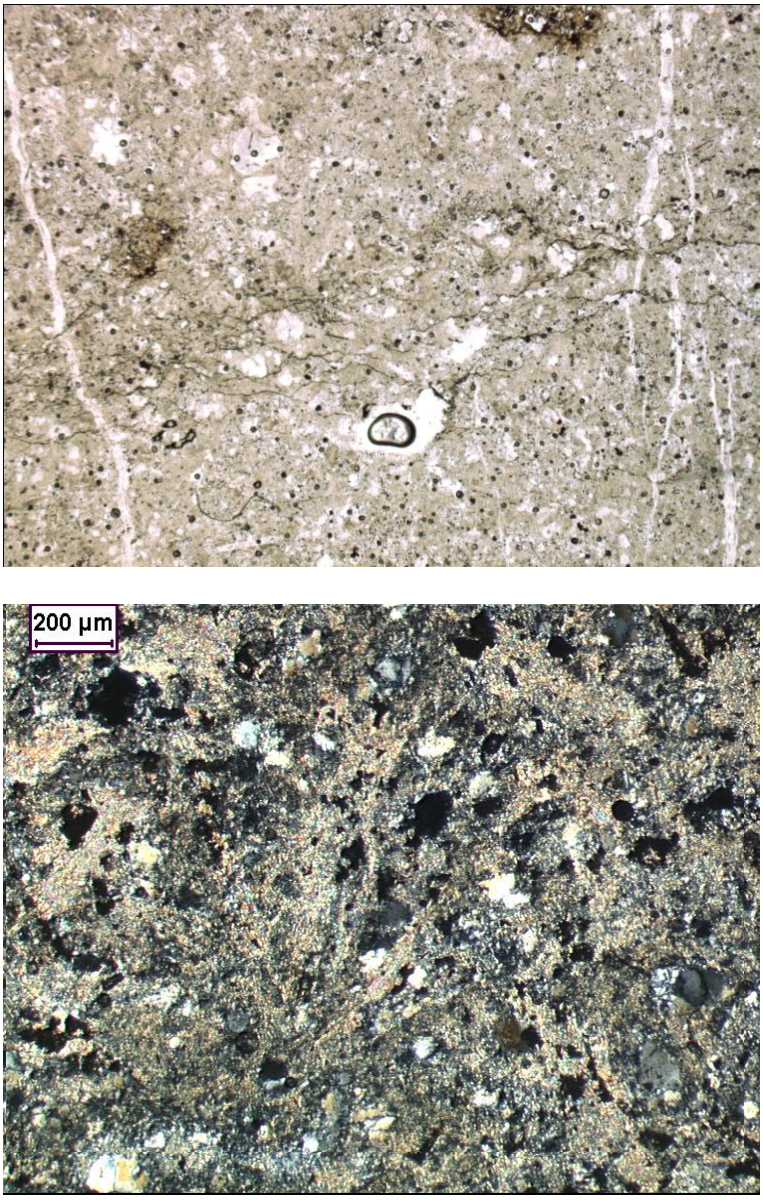

Figure 5.4 (upper) PPL photomicrograph of section p08 showing solution seams running horizontal trough the image and crosscutting the vertical micro-veinlets of quartz (lower) XPL photomicrographs of section p10 showing the intensity of sericite alteration in the thin section.

5.3 Thin section petrogenesis

The samples p04 to p10 are considered to have formed as coherent lavas. Porhyritic textures indicate that the samples have been cooled and solidified in two stages. An early stage of slow cooling led to the crystallisation of large phenocrysts. Subsequently, a stage of relative rapid cooling resulted in the crystallisation of the fine-grained groundmass. The observed contraction veins in sample p07 and the crystallites seen in both samples p07 and p08 even indicate quenching of the lava. This is in agreement with the observations in the field of the sample sites by Kim Hein and Frank van Ruitenbeek (appendix 1). They described sample p07 as being a hydroclastic breccia, which is typical for volcanic rock that is chilled under water or in ice.

The primary mineralogy of the phenocrysts is completely replaced by secondary sericite. However, the shapes of the phenocrysts suggest that feldspar was the primary mineral. Olivine has not been observed in the thin sections and therefore the magmatic source of the volcanic samples must have had an intermediate composition.

The first alteration phase occurred during the cooling process of the volcanic succession and is of deuteric origin. Deuteric alteration is the alteration of recently crystallised magma by trapped magmatic fluid exsolved from the same cooling magma (Shelley, 1993). The changes due to deuteric alteration are minimal and only visible in the groundmass of the least altered samples p04 to p07. It is assumed that all the samples have undergone deuteric alteration, but these changes have been overprinted by later alteration phases and are therefore no longer visible.

The infilling of the vesicles of sample p04 by quartz, the formation of a discontinuous rim of quartz in the phenocrysts of sample p06 and the infilling of the contraction veins in sample p07 by quartz all indicate a silicifcation phase following the first phase of deuteric alteration. Because no sericite was found in the infilling with quartz, it is reasonable to assume a third alteration phase. If the contraction veins in sample p07 were still open during sericitic alteration, the solution seams of sericite would have followed these open spaces. However, a clear crosscut relationship is evident between the solution seams and the contraction veins (Figure 5.4).

In the third alteration phase samples of the volcanic succession have been extensively altered to sericite. The reaction formula of the replacement of feldspar to secondary sericite implies the formation of secondary quartz. The outer reaction rim of re-equilibrated quartz and the few rosettes of sericite in the amygdales of sample p04 in combination with the fibrous outgrowing quartz at the outer part of the phenocrysts in sample p06 confirm the formation of secondary quartz.

Following the transection there is a gradual increase in the intensity of sericite alteration from the moderately altered sample p04 to the intensely altered sample p10. This gradual increase in alteration intensity is determined by the pervasiveness of solution seams, the replacement by sericite and the dissolution of the rock. This finding may imply that the transection follows the hydrothermal circulation of fluids.

According to the Vearncombe (1995) the timing of the chert displacement coincides with the silicification phase. In sample p03 collected from the chert, sericite occurs in distinctive laminae and

shows a simultaneous extinction throughout these whole laminae. This might suggest that the sericite is a primary mineral and consequently the chert would have been displacement during the third sericitic alteration phase.

Weathering in the Panorama district is characterised by the presence of iron-rich coatings of several millimeters in thickness and the presence of halloysites and kaolinites (Van Ruitenbeek et al., 2006). In chapter 4 the presence of the clay minerals halloysites and kaolinites were detected in the thin sections p05, p06 and p09 with the use of spectroscopy. However, the presence could not be confirmed during thin section petrography. This may be due to the microscopic nature of the clay minerals in combination with the very low abundances.

In all thin sections the presence of opaque minerals was established. Especially in the thin section p09 abundances of opaque minerals were much higher compared to the other thin sections. This could be linked to the presence of iron-rich coatings as is mentioned in the paper of Van Ruitenbeek et al. (2006). Therefore, this thin section has indeed undergone weathering.

Chapter 6: Isomorphous substitutions in white mica from the Panorama district

6.1 Introduction

Two types of white mica have been recognised by short wavelength infrared spectral analyses at the Panorama district (Figure 6.1). Short wavelength white mica with the main Al-OH absorption feature at around 2200 nm and a long wavelength white mica with the main Al-OH absorption feature at round 2210 nm. These wavelength variations are directly related to white mica compositional variations (Pontual et al., 1997b). The exact wavelength position of the absorption feature varies as a function of the Al content in white mica (Beran, 2002). Variations in the Al content of white mica are largely the result of the tschermak substitution where Al is replaced by Fe and Mg (Duke, 1994). However, besides the tschermak substitution the Al content in white mica is also controlled by other substitutions like the pyrophyllitic substitution (Yang, 1998).

The main objective of this chapter is to determine the exact white mica composition and the

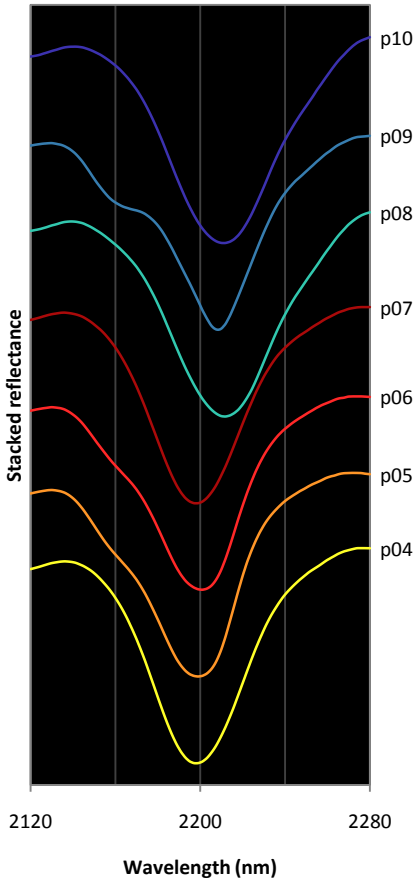

Figure 6.1 Stacked hull quotient reflectance spectra of the white mica dominated samples. The spectra show a distinct wavelength shift of the main Al-OH absorption feature at around 2200 nm of white mica. There are spectral indications like the shoulder near 2160 nm that sample p09 has undergone a low degree of weathering.

relationship between compositional variations in white mica and isomorphous substitutions. Furthermore, the most likely factors controlling the differences in chemical composition of white mica will be discussed.

6.2 Crystallographic description of white mica

6.2.1 Chemical structure

The following section is based on reviews and summaries on mica mineralogy of Deer et al. (1992), Rieder et al. (1998), Brigatti & Guggenheim (2002) and Fleet (2003). Mica minerals are part of the family of phyllosilicates, also referred to as sheet silicates. The mica structure consists of an octahedral sheet (o) between two opposing tetrahedral sheets (t), resulting in 't-o-t' layers. These negatively charged 't-o-t' layers are compensated and bonded together by large, positively charge, interlayer cations (Figure 6.2).

The mica structure has a general formula of $A_2M_{4-6}\square_{2-0}T_8O_{20}X_4$, where:

- *A* is an interlayer cation, usually K, Na, Ca, Ba, and rarely Rb, Cs, NH_4, H_3O and Sr;
- *M* is an octahedral layer cation, generally Mg, Fe^{2+}, Al and Fe^{3+}, but other cations such as Li, Ti, V, Cr, Mn^{2+}, Mn^{3+}, Na, Co, Ni, Cu and Zn can also occur;
- $\square$ is a vacancy in the octahedral layer;
- *T* is a tetrahedral layer cation, generally Si, Al and Fe^{3+}, and rarely B and Be;
- *O* is oxygen;
- *X* is an anion (ligand) not bonded to *T*: (OH), F, Cl, O, S.

The interlayer, octahedral and tetrahedral cations are denoted throughout the text with the superscripts *it*, *vi* and *iv*, respectively. Square brackets are used to indicate the tetrahedral sheet component of complex mineral formulae. It should also be noted that all chemical data in this study are to be considered in terms of a 22 oxygen per formula unit (p.f.u.).

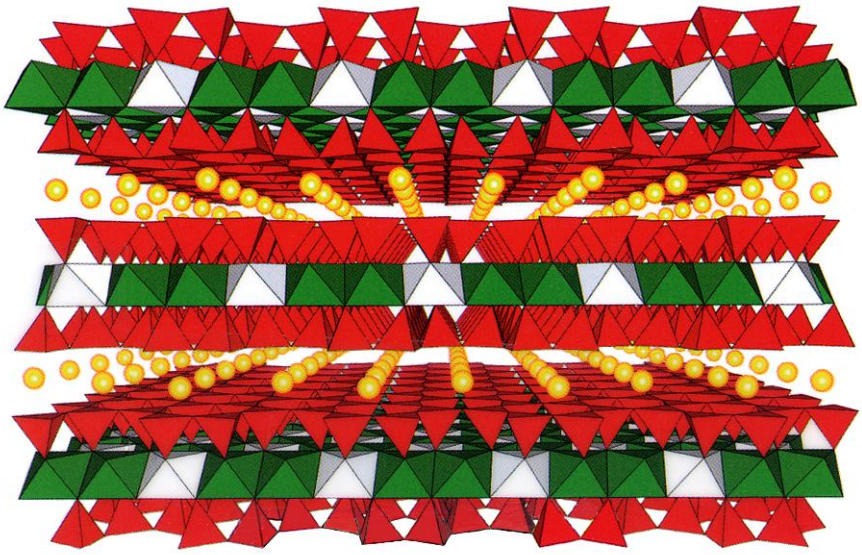

Figure 6.2 Perspective view of 't-o-t' layers in the mica structure. The red layers represent the tetrahedral sheet (t). The green and white octahedra together constitute the octahedral sheet (o). The green octahedra are always occupied, i.e. have octahedral cations at their centres. If half of the white octahedra are also occupied, the mica is trioctahedral, otherwise it is dioctahedral. The yellow spheres represent the interlayer cations (after Mottana *et al.*, 2002).

Table 6.1 Schematic representation of the most common and important isomorphous substitutions in natural white mica. See the text for the substitution formulas. In red the reactant constituents and in green the reaction products. Muscovite, $K_2Al_4[Al_2Si_6O_{20}](OH)_4$, is taken as the initial composition for the substitution direction, except for the Fe-Mg substitution where the direction is arbitrarily chosen. The number of dots represents the number of constituents. Vacant positions are denoted with the symbol □.

Substitution:	**Interlayer**				**Tetrahedral sheet**					**Octahedral sheet**	
	K	Na	Ca	□	Al	Mg	Fe^{2+}	Fe^{3+}	□	Si	Al
Paragonitic	●	●									
Margaritic	●		●							●	●
Pyrophyllitic	●			●						●	●
Tschermak					●	●				●	●
Fe-Mg						●	●				
Ferrimuscovite					●			●			
Di/trioctahedral					●●	●●●			●		

The mica group is subdivided into three subgroups: *true micas*, *brittle micas* and *interlayer-deficient micas*. In a true mica ≥ 50 % of the total interlayer cations present are monovalent. Similarly, in a brittle mica > 50 % of the total interlayer cations present are divalent. If the mineral formula exhibits < 1.7 and ≥ 1.2 positive interlayer charges p.f.u., it represents an interlayer-deficient mica. The 1.7 charge divide holds for dioctahedral micas. The three mica subgroups are further subdivided into *dioctahedral* and *trioctahedral*. A mica is dioctahedral if it contains less than five octahedral cations p.f.u. and trioctahedral with five or more octahedral cations p.f.u. Most of the natural micas occur with intermediate octahedral occupancy.

6.2.2 Isomorphous substitutions

The following section is based on the work of Guidotti & Sassi (1998a; 1998b) and Yang (1998). Natural white mica often shows a significant deviation from the ideal muscovite end-member composition $K_2Al_4[Al_2Si_6O_{20}](OH)_4$. These deviations may be described in terms of a number of isomorphous substitutions leading to partial or complete solid solution with other dioctahedral micas and, to some extent, also with trioctahedral micas. The most common and important isomorphous substitutions in natural white mica are listed below in random order. A schematic overview of these substitutions is presented in Table 6.1.

- Paragonitic substitution: $K^{it} \leftrightarrow Na^{it}$
- Margaritic substitution: $(Na,K)^{it} + Si^{iv} \leftrightarrow Ca^{it} + Al^{iv}$
- Pyrophyllitic substitution: $(Na,K)^{it} + Al^{iv} \leftrightarrow \square^{it} + Si^{iv}$
- Tschermak substitution: $Al^{vi} + Al^{iv} \leftrightarrow (Mg,Fe^{2+})^{vi} + Si^{iv}$
- $FeMg_{-1}$ substitution: $(Fe^{2+})^{vi} \leftrightarrow Mg^{vi}$
- Ferrimuscovite substitution: $Al^{vi} \leftrightarrow (Fe^{3+})^{vi}$
- Di/trioctahedral substitution: $2\ Al^{vi} + \square^{vi} \leftrightarrow 3\ (Mg,Fe^{2+})^{vi}$

The isomorphous substitutions in Table 6.1 lead to micas ranging in composition between the following seven true end-members:

- Muscovite $K_2Al_4[Al_2Si_6O_{20}](OH)_4$
- Paragonite $Na_2Al_4[Al_2Si_6O_{20}](OH)_4$
- Margarite $Ca_2Al_4[Al_4Si_4O_{20}](OH)_4$
- Pyrophyllite $Al_4[Si_8O_{20}](OH)_4$
- (Ferro)celadonite $K_2Fe^{3+}{}_2(Mg,Fe^{2+})_2[Si_8O_{20}](OH)_4$
- (Ferro-)aluminoceladonite $K_2Al_2(Mg,Fe^{2+})_2[Si_8O_{20}](OH)_4$
- Biotite $K_2(Mg,Fe^{2+})_6[Al_2Si_6O_{20}](OH)_4$

The mica subcommittee (Rieder et al., 1998) approved the term *illite* as a series name for dioctahedral interlayer-deficient micas with a composition as defined in Figure 6.3. The term *phengite* refers to a series name for solid solutions involving muscovite, aluminoceladonite and celadonite (Figure 6.3), as appointed by the subcommittee.

Although the Ti substitution is usually insignificant in amount, it is quite important because the amount of Ti substitution is sensitive to temperature. However, the specific nature of the substitution remains ambiguous and disputed (Guidotti & Sassi, 2002). Spear (1993) describes two substitutions in mica involving Ti: the Ti-Tschermak substitution [$(Mg,Fe^{2+})^{vi}$ + 2 Si^{iv} ↔ Ti^{vi} +2 Al^{iv}] and a substitution in which Ti is coupled with Fe [2 $(Fe^{3+})^{vi}$ ↔ Ti^{vi} + $(Fe^{2+})^{vi}$]. Fleet (2003) reports a comparable substitution, but with Al as the reactant constituent [2 Al^{vi} ↔ Ti^{vi} + $(Fe^{2+})^{vi}$].

6.3 White mica composition

Compositional differences in white mica from the Panorama district are evident trough comparison of the average electron microprobe analyses presented in Table 6.2. The electron microprobe results reveal a distinct change in the white mica composition along the transection. Based on these compositional differences the samples are divided into two groups according to their total Al-content, i.e. an Al-rich group comprising the thin sections p04, p05, p06 and p07, and an Al-poor group comprising the thins sections p08 and p10. Thin section p09 chemically belongs to the Al-rich group but is omitted from this group because of evidence of late stage supergene alteration of this sample.

The following characteristics and differences between the two Al groups were observed after careful

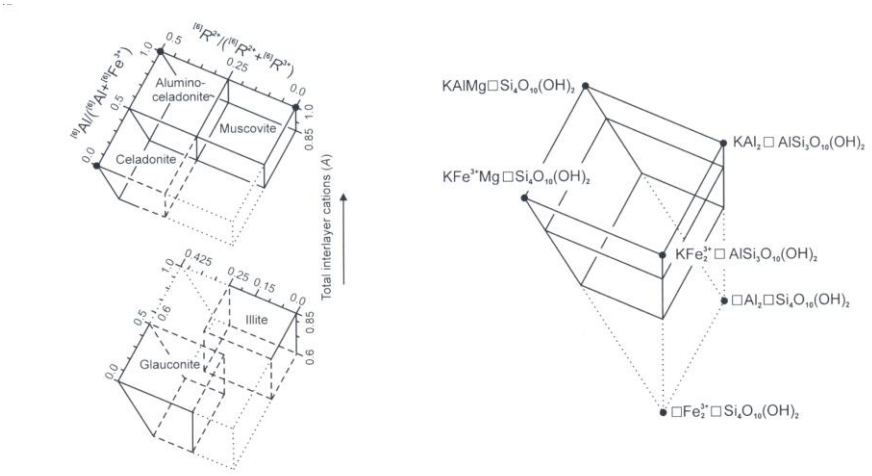

Figure 6.3 A three-dimensional plot in exploded view illustrating the compositional range for the illite and phengite series. Dashed lines indicate approximate composition limits. The dotted lines complete the solid solution (after Rieder *et al.*, 1998).

Table 6.2 Average white mica composition of the 7 thin sections analysed by electron microprobe expressed by structural formulae and major components. Results below the limit of detection are omitted for the average structural formulae calculations. Results marked with an asterix (*) are semi-quantitative. All the other results are quantitative with a high degree of confidence. All iron is given as ferrous iron. Structural formulae are based on 22 oxygen atoms. *K** = K/(Na + K + Ca); *Ms* muscovite; *Pg* paragonite; *Mrg* margarite; *Fe-Cel* Fe-aluminoceladonite; *Mg-Cel* Mg-aluminoceladonite; *Prl* pyrophyllite; *Bt* biotite.

Sample #	**p04**	**p05**	**p06**	**p07**	**p08**	**p09**	**p10**
# of analyses	40	20	31	30	30	28	23
Si	6.25	6.32	6.36	6.30	6.68	6.42	6.75
Al^{iv}	1.75	1.68	1.64	1.70	1.32	1.58	1.25
Σ*iv*	8	8	8	8	8	8	8
Al^{vi}	3.88	3.87	3.84	3.84	3.50	3.77	3.48
Mg	0.16	0.12	0.17	0.12	0.40	0.22	0.43
Fe^{2+}	0.07	0.08	0.09	0.09	0.21	0.09	0.22
Ti	0.01*	0.01*	0.01*	0.01*	0.01*	0.01*	0.01*
Σ*vi*	4.12	4.08	4.11	4.06	4.12	4.09	4.14
K	1.55	1.54	1.51	1.66	1.52	1.56	1.41
Na	0.08	0.07	0.05	0.06	0.01*	0.02*	0.02*
Ca	0.00*	0.01*	0.01*	0.01*	0.01*	0.01*	0.01*
Σ*it*	1.63	1.62	1.57	1.73	1.54	1.59	1.44
Mg/Fe	2.96	1.42	1.89	1.33	1.98	2.39	1.96
K*	0.95	0.95	0.96	0.96	0.99	0.98	0.98
Ms	74.49	73.45	71.46	77.62	57.70	70.93	52.45
Pg	3.82	3.68	2.46	2.79	0.74	1.14	1.05
Mrg	0.14	0.26	0.36	0.35	0.36	0.27	0.47
Fe-Cel	0.42	0.42	0.08	1.03	1.84	0.02	1.21
Mg-Cel	1.17	1.51	1.41	2.10	10.77	3.98	10.61
Prl	16.43	17.69	20.42	13.46	22.47	19.79	27.22
Bt	1.24	1.84	2.61	2.10	5.80	3.02	6.47
Σ	97.73	98.84	98.81	99.45	99.69	99.14	99.49

examination of the microprobe results and the averaged compositions presented in Table 6.2.

- The Al-rich group contains higher contents of Al coupled with a lower content of tetrahedral Si in both the tetrahedral and octahedral sites compared to the Al-poor group (Figure 6.4).
- Both the Mg and Fe^{2+} content are higher in the Al-poor group than the Al-rich group. The average value of the ratio Mg/Fe is approximately 2 for both groups. However, the ratio values of the Al-rich group show considerably more variation than those of the Al-poor group.
- The total number of octahedral cations p.f.u. is slightly higher for the Al-poor group compared to the Al-rich group.
- The total number of interlayer cations p.f.u. is higher for the Al-rich group in contrast to the Al-poor group.
- The Al-rich group contains higher contents of the interlayer cations K and Na, while the Al-poor group contains higher contents of the interlayer cations Ca. Although the absolute K content values are higher in the Al-rich group, the relative K content values are higher in the Al-poor group. These relative content values were calculated using the following ratio: K/(Na + K + Ca).

- Titanium is present in average trace amounts of approximately 0.01 atoms p.f.u. in both Al groups. Because 3.3 % of the Ti results exceed the limit of quantitation in the Al-rich group compared to 18.9 % in the Al-poor group, the latter is probably slightly enriched with Ti.
- Reported concentrations of the elements Cr, Mn, Ni and P never exceeded 0.1 wt% in both groups. All analyses were rejected as being less than the limit of detection.
- For the anions S, F and Cl the number of results greater than the limit of detection were 2, 2 and 15 respectively. Given the small number of results above the limit of detection, it was not possible to draw significant conclusions with respect to these three anions.
- Approximately half of the Na results and almost all of the Ca and Ti results show concentrations between the limit of detection (LOD) and the limit of quantitation (LOQ). This indicates that these elements are recognisably present, however cautious interpretation of these results is necessary. The compositional difference between both Al groups may or may not differ significantly.

The difference in Al and Si content between the two Al groups (Figure 6.4) can be attributed to a number of isomorphous substitutions as presented in Table 6.1. The two most important ones are the

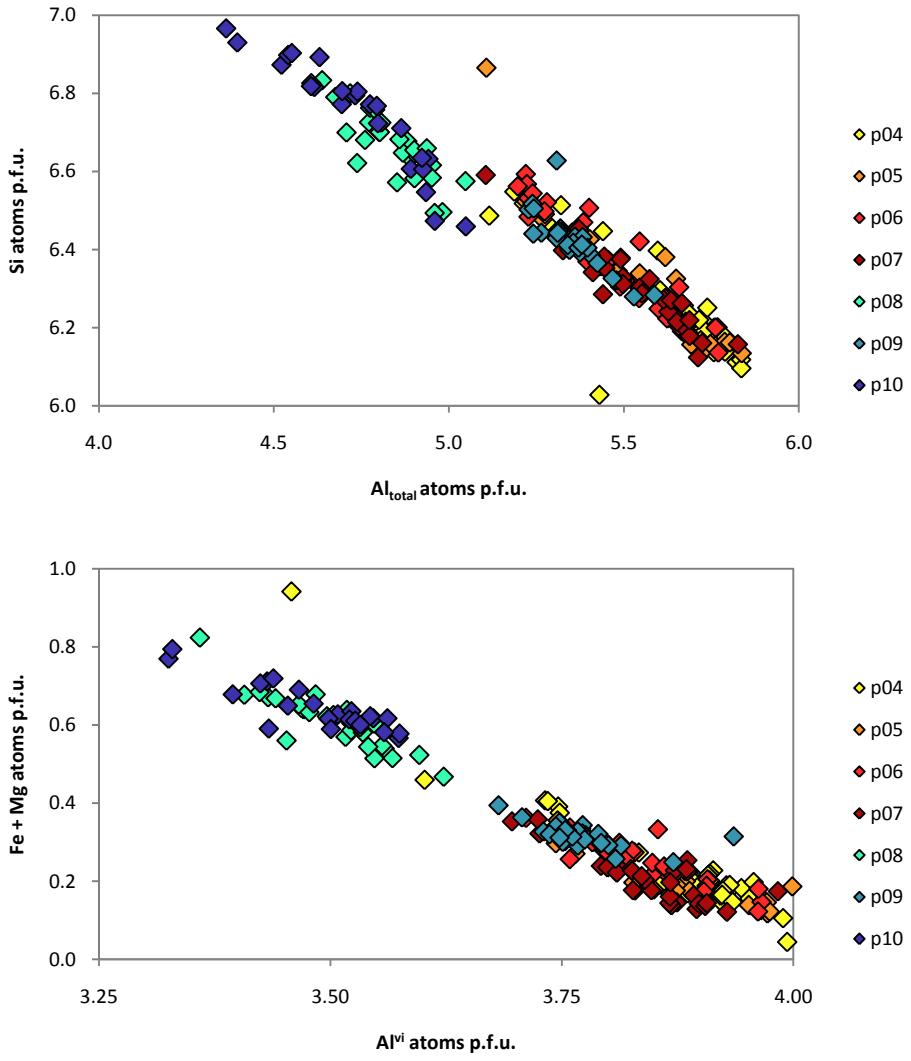

Figure 6.4 Electron microprobe results for with mica with total number of Al atoms p.f.u. plotted against the number of Si atoms p.f.u. and the number of octahedral Al atoms p.f.u. plotted against the number of Fe + Mg atoms p.f.u.

tschermak substitution and pyrophyllitic substitution. White mica of the Al-poor group shows a drastic increase in the endmember components of these two substitutions (Table 6.2). Other substitutions involving both Al and Si are the margaritic and ferrimuscovite substitution. Na concentrations in white mica are often below 0.1 atoms p.f.u. and the extent of the margaritic substitution is therefore neglectable. The ferrimuscovite substitution could not be assessed, because of the inability of the electron microprobe to distinguish between ferric and ferrous iron.

In the study by Brauhart (1999) microprobe analyses were also performed on white micas from the Panorama district. The primary aim was to define spatial variations in the white mica chemistry. In contrast to the current study, the study of Brauhart focused on a regional scale between the different lithologies and alteration facies. No clear relationship was found, but Brauhart (1999) showed, although not explicitly mentioned in his thesis, that the variations in white mica composition throughout the Panorama district are the result of Tschermak substitution and probably, for a part of the white micas, also pyrophyllitic substitution.

6.4 Controls on white mica composition

The chemical composition of white mica in metamorphic rocks and the corresponding isomorphous substitutions have been studied extensively. In metamorphic rocks the main controls on the white mica composition are temperature, pressure and to some extent also bulk-rock composition. The effect of these conditions on the composition of white mica in these systems is well constraint. In contrast to a metamorphic system, in a hydrothermal system also factors like like the fluid chemistry, fluid pressure and the water-rock ratio can influence the chemical composition of white mica. The effect of these conditions on the chemical composition is less well defined. Furthermore, conditions during metamorphism are generally of another order of magnitude compared to a hydrothermal system. For example, most experimental results and observations made on metamorphic rocks are for relatively high lithostatic pressures. When assuming that the during hydrothermal alteration at the Panorama district the seabed was marked by the Marker chert, the samples of this study were at that located at a maximum depth of 500 m below the seabed. Despite these difficulties an attempt has been made to discuss the most likely factors controlling compositional differences in white mica from the Panorama district.

An important factor controlling the white mica composition is often temperature. At the Los Azufres geothermal field increasing temperatures are accompanied by an increase in the octahedral Fe + Mg atoms and interlayer K atoms and a decrease in the pyrophyllitic component (Cathelineau & Izquierdo, 1988). The same increase in the octahedral Fe+ Mag atoms is also observed along the transaction (Figure 6.4). However, the number of interlayer K atoms decreases just as the pyrophyllitic component. This inconsistency is probably the result of the greater complexity of hydrothermal systems.

Also host-rock lithology can influence the white mica composition. Along the transection the division between the Al-rich group and Al-poor group coincide with a change from dacite to andesite-basalt as the primary rock type (Brauhart et al., 1998 and Brauhart, 1999). However, we will show in Chapter 8 that also sample p08 belongs to the more evolved primary rock type. Consequently, this apparent coincidence is not true and there seems to be no relationship between the Al content in white mica and the primary rock type.

Chapter 7: Trace element concentrations in white mica

7.1 Introduction

In the previous chapter compositional variations of white mica from the Panorama district have been discussed with respect to the most common and important isomorphous substitutions occuring in white mica. However, although often ignored during analytical work, also trace elements can be a major constituent in white mica and can have important petrologic and geologic implications Guidotti & Sassi (1998a; 1998b). Failure to analyse these elements can have major consequences. For example, in our study the extent of the pyrophyllitic and di/trioctahedral substitutions is determined by the occupancy of the interlayer and octahedral sheet, respectively. These compositional quantities cannot be determined by electron microprobe analyses and are therefore calculated from the other results. By the failure to analyses for elements like Sr, Ba, V, etc. by electron microprobe the calculated occupancy does not necessarily represent the true occupancy and consequently false conclusions can be drawn.

Trace element concentrations in white mica have been determined by laser ablation ICP-MS. Results of these analyses are presented and discussed in this chapter. For a detailed description of the followed analytical procedure, analytical specifications and data quality the reader is referred to Section 3.5.

7.2 Analytical results and discussion

The results of the laser ablation ICP-MS analyses of white mica have been summarised in Table 7.1. Rare earth element results have been excluded from this table, as concentrations are in general below the limit of quantitation and even below the minimum detection limit. This, despite the extremely low minimum detection limits in the lower ppb range for the rare earth elements. None of the analysed trace elements occurs as an abundant element in white mica. Only Ba occurs in minor concentrations

Table 7.1 Average trace element concentrations in white mica for the six samples analysed by laser ablation ICP-MS. Results marked with an asterix (*) are semi-quantitative. All the other results are quantitative with a high degree of confidence.

Sample #	**p04**	**p06**	**p07**	**p08**	**p09**	**p10**
# of analyses	6	4	5	8	2	4
V	21	84	74	24	510	285
Cr	12	4	2*	21	3*	1*
Ni	3*	7*	2*	7*	11*	20
Rb	297	337	285	334	327	287
Sr	13	8	4	3	2	2
Zr	7	10	5	12	7	16
Cs	6	6	2	8	2	11
Ba	3921	1451	1017	952	973	1011
Hf	2	2	2	2	1	1
Ta	6	6	6	4	4	0

of more than 0.1 weight % in white mica for the samples p04, p06 and p07. Ba is an interlayer constituent and the presence of minor amounts of Ba can affect the calculated interlayer occupancy, as presented in Table 6.2. Recalculation of the average white mica structural formula of sample p04 now including BaO yields an almost similar result. The interlayer occupancy increases with 0.1 atoms p.f.u. As the other analysed samples have compared to sample p04 a Ba concentration of less than half, the effect of Ba on the interlayer occupancy can be neglected. Conclusions drawn in chapter 6 regarding the interlayer occupancy therefore hold.

Concentrations of V, Cr, Ni, Zr, Cs vary considerably, by sometimes a factor 10 or more, between the samples. However, concentrations of these elements show no consistent trend throughout the transect. In contrast, to the elements Sr, Hf, Ta and to some extent Ba which show a decreasing trend in the concentration from sample p04 to p10. Although it is not easy to petrogenetically explain the decreasing trend for these elements it is possibly related to the temperature during hydrothermal alteration. The most convincing evidence for this suggestion comes from the element Sr as explained in the following subsection.

7.2.1 The Rb-Sr system

The following section describes an innovative approach to determine in a qualitative manner the temperature along the transect at the time of hydrothermal alteration using the Rb and Sr concentration of white mica. This approach is based on the Rb-Sr dating method and the closure temperature concept. Principles of these two fields are explained in standard textbooks on radiogenic isotope geology, as for example the classic work of Faure (1986).

Rb has two naturally occurring isotopes, ^{85}Rb and ^{87}Rb, whose isotopic abundances are 72.2 % and 27.8 %, respectively. Only ^{87}Rb is radioactive and decays to the stable isotope ^{87}Sr with a half-life of around 48.8 Gyr. As the relative mass difference between ^{85}Rb and ^{87}Rb is very small and Rb has only one oxidation state it is not likely that during geological processes isotopic fractionation of Rb occurs (White, 2005). This is confirmed by the paper of Nebel et al. (2005) in which no natural variations in the $^{87}Rb/^{85}Rb$ ratio of different geological samples could be observed. Therefore, it is perfectly acceptable to assume that the Rb isotope composition in white mica is the same for all the six hydrothermally altered volcanic samples analysed by laser ablation ICP-MS. Figure 7.1 shows that,

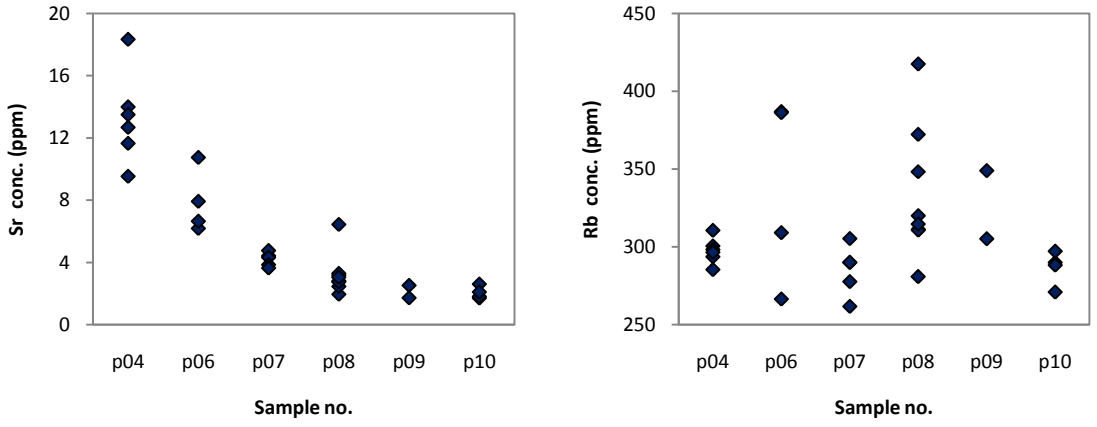

Figure 7.1 Sr and Rb concentration of white mica along the transect.

although within individual samples the concentration of Rb in white mica considerably varies, along the transect the Rb concentration in white mica is fairly constant. Consequently, at any moment in time the number of Rb atoms decaying to Sr is for the whole transect more or less similar.

Sr has four naturally occurring isotopes, ^{84}Sr, ^{86}Sr, ^{87}Sr and ^{88}Sr, all of which are stable. The Sr concentration in a mineral or rock that contains Rb is the sum of initial Sr present after formation and radiogenic Sr produced within the system by the decay of ^{87}Rb. This is only true when the rock or mineral system has neither lost nor gained either Rb or Sr after formation except by radioactive decay. The rock or mineral must be a so-called "closed system" with respect to Rb and Sr. Along the transect the concentration of Sr in white mica decreases gradually with relative high concentrations for sample p04 to relative low concentrations for samples p09 and p10. As earlier explained this decreasing trend is not the result of differences in the produced radiogenic Sr between the individual samples. Consequently there are two remaining possibilities to explain the trend: differences in the initial Sr concentration between the samples or the system has not remained closed for Sr. For the latter possibility the system could have become open during the hydrothermal alteration stage or during the metamorphic stage.

The closure temperature of a system is the temperature at which diffusion of the radiogenic daughter product becomes negligible and the system becomes closed. Different minerals and different isotopic systems close at different temperatures. The closure temperature for Sr in white mica is about 550 °C (Freeman et al., 1997). Temperatures during the hydrothermal alteration stage are estimate by Brauhart et al. (2000) using oxygen isotopes and are for the transect in the range of 200–250 °C. Lower greenschist facies metamorphism of the Panorama district yields an almost similar temperature range. This temperature range is far below the closure temperature of white mica. However, as Wickman et al. (1983) discussed the closure temperature of white mica can be drastically lowered by fluid circulation. The study shows that post-deformational fluid circulation in granitoid rocks resets the $^{87}Sr/^{86}Sr$ ratio. The hydrothermal system at Panorama is regarded as a high fluid-rock ratio system (Brauhart et al., 2000; 2001; Schardt et al., 2005). Therefore, it is possible that during hydrothermal alteration of the volcanic succession temperatures were high enough to start diffusion of Sr in white mica. The higher the temperature the more Sr would escape the white mica. Consequently, the decreasing trend in the Sr concentration of white mica along the transect is interpreted to represent a increase in the temperature during hydrothermal alteration of the rocks.

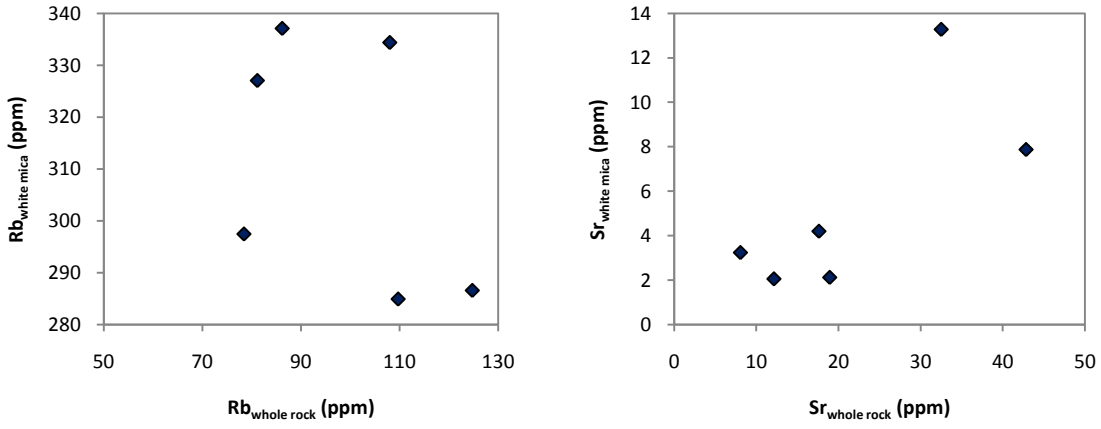

Figure 7.2 Bivariate plots of average element concentrations in white mica versus concentrations in the whole rock.

It is assumed that the mineral white mica has acted as a single, isolated system to Rb and Sr and that there has been no interaction with the surrounding, apart from diffusion of Sr out of the system. This assumption is tested by plotting the average Rb and Sr concentrations of white mica from Table 7.1 against Rb and Sr concentrations of the whole rock (Figure 7.2). Rb concentrations are a few factors lower in the whole rock compared to white mica and the opposite is observed for Sr. Furthermore, there is no relationship between Rb and Sr concentrations in white mica to concentrations in the whole rock. Therefore, based on the plots in Figure 7.2 the assumption of a single and isolated system for white mica seems to be justified.

Chapter 8: Whole-rock lithogeochemical signatures

8.1 Introduction

This chapter is concerned with the interpretation of the whole-rock lithogeochemistry of the 11 rock samples. A detailed description of the analytical procedures and data quality of the whole-rock lithogeochemical analyses is given in Section 3.6. Different applications of whole-rock lithogeochemistry, i.e. immobile elements, alteration indices and rare earth element geochemistry, will be used in this chapter to characterise, quantify and interpret the process of hydrothermal alteration at the Panorama district for the 11 rock samples, but also to determine primary geochemical characteristics of the volcanic rock samples before alteration. Immobile elements can be reliably used to classify and correlate altered volcanic rocks. Alteration indices are very useful in the discrimination and characterisation of alteration styles and in the quantification of alteration intensity. Furthermore, rare earth elements may help to define conditions during the hydrothermal alteration event at the Panorama district.

8.2 Immobile elements

Extensive hydrothermal alteration at the Panorama district precludes the use of major elements to determine the primary geochemical characteristics of the 11 rock samples. However, several elements remain immobile during most types of hydrothermal alteration and these can be reliably used to classify and correlate altered volcanic rocks. In this context, *immobile* means elements that are neither added to, nor taken from, the rock during alteration. Many studies on VMS deposits have shown that Al, Ti, Zr, Nb, Y, heavy rare earth elements (Yb, Lu), Hf, Ta and Th, and in some cases Sc, V and Cr, remain essentially immobile during alteration (*references in* MacLean & Barrett, 1993; Gifkins et al. 2005). However, as is shown by for instance Finlow-Bates & Stumpfl (1981), some of these elements like Sc, Nb and Th can indeed be extremely mobile during intense hydrothermal alteration. Therefore, element immobility is first established, rather than assumed, before proceeding with the interpretation of the altered rock samples.

Immobility of elements is established by plotting potentially immobile elements on a bivariate diagram with the origins at zero. If the selected elements are immobile, the data points will show a highly correlated linear trend, known as an alteration line, which projects through the origin of the plot. Addition of mobile elements, as in silicification, or extraction of material, as by solution, causes the proportion (i.e. concentration) of immobile elements to change, but the inter-element ratios remain essentially constant. Subsequently, these plots can be used to identify different magmatic suites and chemically distinct rock units, which may otherwise be unnoticed. Samples from different magmatic suites produce separate alteration lines in plots of incompatible-incompatible element pairs. When the element pairs are compatible-incompatible, a separate alteration line is formed for each chemically distinct rock unit. Sample p03 has been excluded from these plots, because the above mentioned procedure is only applicable to igneous rocks.

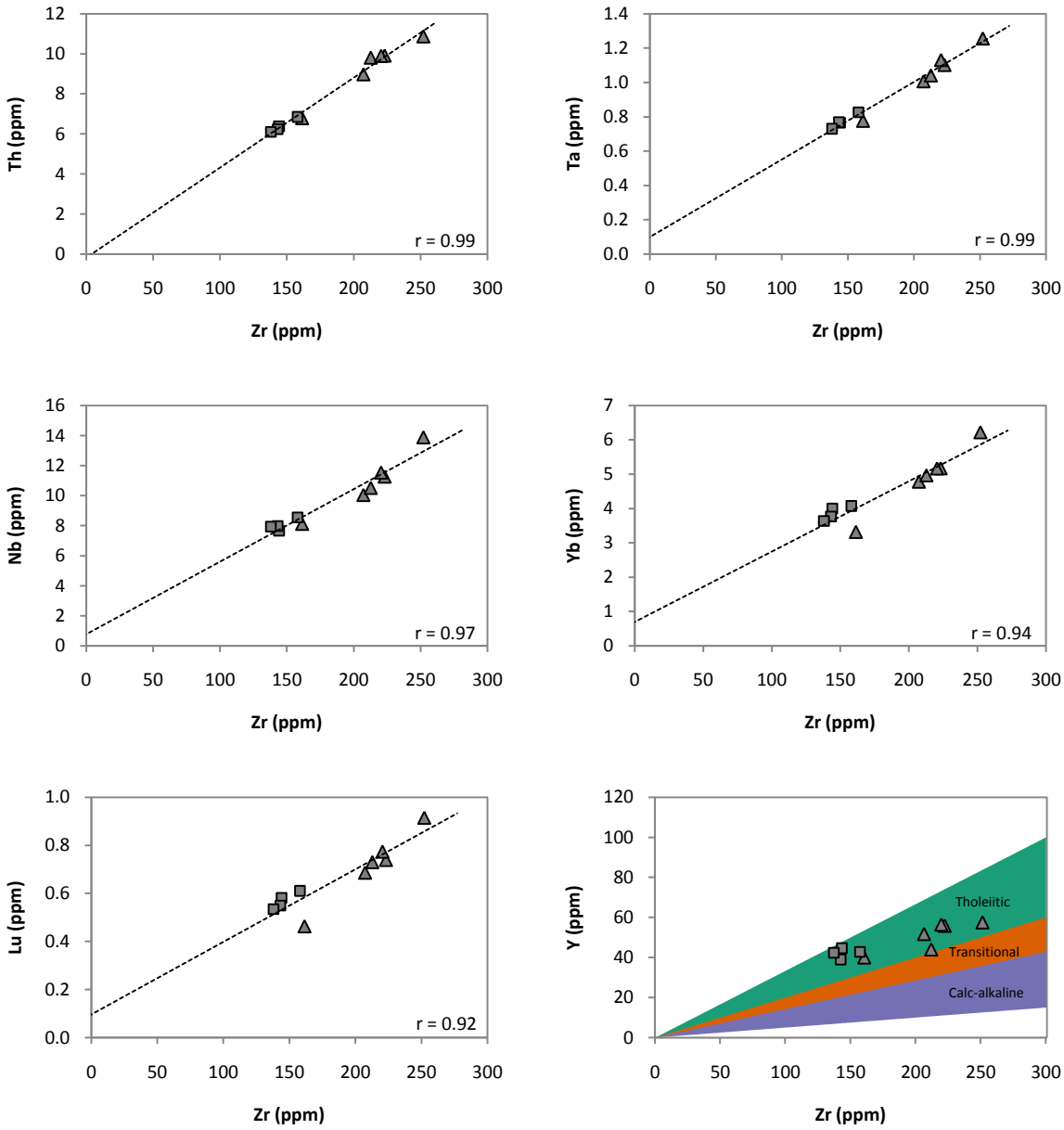

Figure 8.1 Bivariate plots for a range of incompatible elements plotted against the incompatible element Zr. The r values are the correlation coefficients of the dashed alteration lines. The plots indicate a single volcanic suite of tholeiitic composition for the volcanic samples. Magmatic affinity fields in the Y-Zr plot after MacLean & Barrett (1993). Symbols after this study: *triangles* = andesites; *squares* = basalts.

8.2.1 Magmatic affinity and primary rock type identification

Figure 8.1 shows incompatible elements plotted against the incompatible element Zr for the 10 volcanic samples. Alteration lines are indicated in each plot by a dotted line. The highly correlated linear alteration trends for Zr, Nb, Yb, Lu, Ta and Th suggest that these elements were essentially immobile during hydrothermal alteration and sub-greenschist facies metamorphism in the region. The small data scatter in the plots is probably the result of analytical errors and slight inhomogeneities in the primary rock. The plots display a single alteration trend indicating that the volcanic samples belong to a single volcanic suite. This suite corresponds geochemically and stratigraphically to the

upper (volcanic) suite in the work of Brauhart (1999) and Brauhart et al. (2001) and to the footwall (volcanic) rocks in the work of Vearncombe (1995) and Vearncombe & Kerrich (1999).

The plot of Y versus Zr does not define as clear a trend as the previous plots. As also mentioned by Brauhart (1999) possibly due to minor mobility of Y. Using the subdivision of MacLean & Barrett (1993), all samples have a Zr/Y ratio between 3.2 and 4.8 and are thus classified as tholeiitic. Besides the already mentioned elements, the only other elements which have behaved as essentially immobile are Al, Ti, Er, Tm and Hf (not shown).

When plotting compatible-incompatible element pairs, such as Al_2O_3–Zr and TiO_2–Zr (Figure 8.2), it becomes apparent that the 10 volcanic samples form two separate groups. This indicates that the volcanic suite is magmatic differentiated and that the samples represent two chemically distinct rock units. The data scatter in the group with the smallest slope (triangles) is probably the result of inhomogeneities in the primary rock caused by, for example, mechanical sorting during eruption. For the immobile element pair TiO_2–Zr, Brauhart (1999) and Brauhart et al. (2001) defined a fractionation trend for the upper volcanic suite based on least altered samples (Figure 8.2). From this trend it becomes apparent that the samples indicated with a triangle and represented by the sample numbers p04 to p08 and p14 are more evolved than the samples indicated with a square and represented by the sample numbers p09, p10, p12 and p13. Furthermore, according to the sample descriptions of Hein & Van Ruitenbeek (Appendix 1) sample p05 is classified as a third and more fractionated rock type (Table 8.1). Except for very primitive rock types, the following rule can normally be applied to the TiO_2–Zr plot: the more a rock is fractionated, the smaller the slope of the alteration line for that particular rock type. In the TiO_2–Zr plot sample p05 is no isolated point, nor has a hypothetical alteration line through this point the smallest slope. Therefore, it is not likely that sample p05 forms an individual, more fractionated rock type.

Brauhart (1999) and Brauhart et al. (2001) have used least altered samples to construct a fractionation trend for the volcanic succession. These least altered samples are considered to most closely approximate zero net mass transfer. Based on this, all the volcanic samples, except sample p07, have

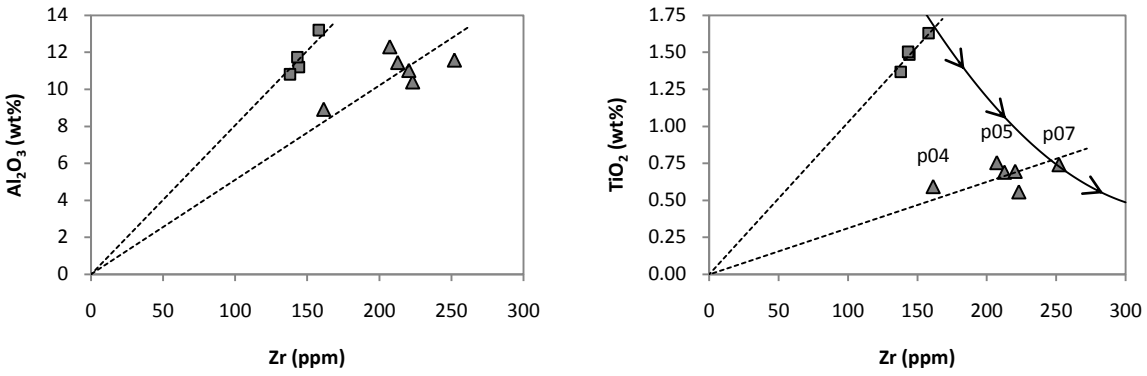

Figure 8.2 Bivariate plots for the two compatible components Al_2O_3 and TiO_2 plotted against the incompatible element Zr. Alteration lines are represented by a dashed line and are plotted under the condition that the lines have to pass through the origin. The plots indicate that the samples can be divided into two chemically distinct rock units. Fractionation trend after Brauhart (1999) and Brauhart et al. (2001) and based on least altered samples, which are considered to most closely approximate zero net mass transfer. Arrows indicate the direction of fractionation. Symbols after this study: *triangles* = andesites; *squares* = basalts.

Table 8.1 Primary rock type classification of the 10 altered volcanic samples. In the present study identification of the primary rock type before alteration is based on the Zr/TiO_2 versus Nb/Y discrimination diagram of Pearce (1996).

Sample No.	Primary rock type according to:		
	the geological map of Brauhart (1999) and Brauhart et al. (1998)	the sample descriptions of Hein & Van Ruitenbeek (Appendix 1)	present study
p04	dacite	dacite	andesite
p05	dacite	rhyodacite	andesite
p06	dacite	dacite	andesite
p07	dacite	dacite	andesite
p08	andesite-basalt	dacite	andesite
p09	andesite-basalt	basalt	basalt
p10	andesite-basalt	basalt	basalt
p12	andesite-basalt	basalt	basalt
p13	andesite-basalt	basalt	basalt
p14	andesite-basalt	basalt	andesite

undergone net mass gain. Net mass gain will cause the immobile elements to dilute resulting in the altered samples to plot below the fractionation trend. Sample p07 plots on the fractionation trend. This does not imply that element concentrations, other than the immobile ones, reflect actual concentrations of the primary rock, but that mass gain equals mass loss. Typically, seriticisation and chloritisation are often accompanied by strong leaching of certain elements resulting in mass loss (MacLean & Barrett, 1993). Observed dissolution vugs in the thin sections are the product after extreme leaching of the primary rock. That the samples have still undergone mass gain, is probably the result of extensive silicification of the volcanic succession. This is observed throughout the thin sections by the infilling of vesicles and contraction fractures by quartz. This also explains why sample p04 has undergone the largest mass gain. Former vesicles comprise about 20–25 % of this sample and have been completely filled.

In order to define the primary rock types of the 10 volcanic samples the Zr/TiO_2 versus Nb/Y discrimination diagram of Pearce (1996) is used (Figure 8.3). The two earlier identified rock units

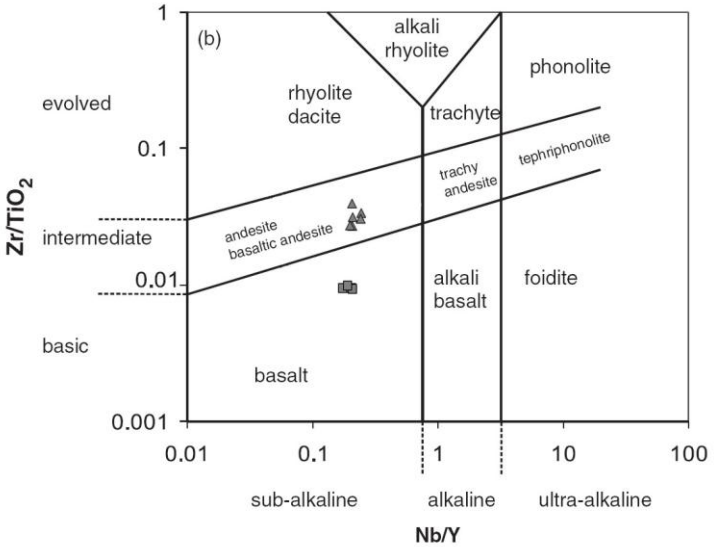

Figure 8.3 Discrimination diagram using the plot of Zr/TiO_2 versus Nb/Y (after Pearce, 1996), defining the primary rock types of the 10 altered volcanic samples. The samples p04 to p08 and p14 plot in the (basaltic) andesite field and are indicated with a triangle. The samples p09, p10, p12 and p13 plot in the basalt field and are indicated with a square.

form two separate clusters of samples in the diagram. According to this diagram the primary rock type of the samples indicated with a triangle and represented by the sample numbers po4 to p08 and p14 is (basaltic) andesite. The primary rock type of the samples indicated with a square and represented by the sample numbers p09, p10, p12 and p13 is basalt. The primary rock type of each volcanic sample indentified in this study does not totally agree with both the geological map of Brauhart (1999) and Brauhart et al. (1998) and the sample descriptions of Hein & Van Ruitenbeek (Appendix 1). Differences can be found in Table 8.1. It can be indicated from Table 8.1:

- Sample p05 is not recognised as a separate and more evolved rock type in the present study.
- The primary rock type of the samples belonging to the more basic rock unit is basalt.
- The primary rock type of the samples belonging to the more evolved rock unit is andesite. Andesite is preferred over basaltic andesite as the primary rock type, because andesite corresponds more to dacite, which is the rock type mentioned by the other authors.
- Sample p08 belongs to the more evolved rock unit.
- Sample p14 also belongs to the more evolved rock unit.

However, a problem of the discrimination diagram of Pearce (1996) is the large overlap between the different rock types. Samples are assigned to a rock type based on the highest probability. Other rock types may therefore not be excluded.

8.3 Alteration indices

Alteration indices are a very powerful tool in the discrimination and characterisation of alteration styles and the quantification of alteration intensity. They are geochemical representations of hydrothermal mineral assemblages and calculated from lithogeochemical composition data. Alteration

Table 8.2 Summary of alteration indices examined in the present study.

Alteration index	Element ratios	Source
Ishikawa alteration index (AI)	$\frac{100(K_2O + MgO)}{(K_2O + MgO + Na_2O + CaO)}$	Ishikawa et al. (1976)[a]
Chlorite-carbonate-pyrite index (CCPI)	$\frac{100(MgO + FeO + Fe_2O_3)}{(MgO + FeO + Fe_2O_3 + Na_2O + K_2O)}$	Large et al. (2001)
Sericite index	$\frac{100\ K_2O}{(K_2O + Na_2O)}$	Saeki & Date (1980)[b]
Silicification index (SI)	$\frac{100\ SiO_2}{(SiO_2 + Al_2O_3)}$	Van Ruitenbeek et al. (2005)
Alkali index	$\frac{100(Na_2O + CaO)}{(Na_2O + CaO + K_2O)}$	Saeki & Date (1980)[b]
Hashigushi index	$\frac{100\ Fe_2O_3}{Fe_2O_3 + MgO}$	Hashigushi (1983)[b]
Spitz-Darling	$\frac{Al_2O_3}{Na_2O}$	Spitz & Darling (1978)[b]
	$\frac{Zn}{Na_2O}$	Franklin (1997)

[a] *cited in* Franklin (1997); Large et al. (2001); Gifkins et al. (2005)

[b] *cited in* Franklin (1997)

indices have been widely applied in research and exploration for VMS deposits. However, as also discussed by Eilu et al. (1995) there are several limitations affecting the interpretation of results obtained from alteration indices. Primary lithological variations, several mineral phases controlling an alteration index and significant differences between individual districts are some of the problems. Furthermore, although alteration indices are less affected by closure than composition data, they are not independent of closure (Gifkins et al., 2005). However, when knowing and taking these limitations into account, reliable results can be obtained from alteration indices.

A wide variety of alteration indices have been examined in this study and these indices are listed in Table 8.2. Alteration indices are only recommended for the study of alteration in primary volcanic rocks and lavas, as also addressed by Large et al. (2001). Therefore, sample p03, the Marker Chert sample, has been excluded from further consideration.

8.3.1 Alteration box plot

The alteration box plot of Large et al. (2001) is a graphical representation of the Ishikawa alteration index (AI) plotted in the horizontal axis and the chlorite-carbonate-pyrite index (CCPI) in the vertical axis. The Ishikawa alteration index is also often termed in the literature 'Ishikawa index', 'alteration index' or even 'Hashimoto index'. The chlorite-carbonate-pyrite index is also known as the chlorite index of Saeki & Date (1980, *cited in* Franklin, 1997).

The AI quantifies the intensity of sericite and chlorite alteration and is useful in many plagioclase-destructive hydrothermal alteration systems. The AI represents the principal rock-forming components gained (MgO and K_2O) during chlorite and sericite alteration, and those lost (Na_2O and CaO) during the breakdown of Na-plagioclase and volcanic glass. It typically increases to maximum values in the proximal hydrothermal zones beneath massive sulfide ore lenses. The index ranges from the values 20 to about 60 for unaltered rocks and from 50 to 100 for hydrothermally altered rocks. An AI of 100 represents complete replacement of feldspars and glass by sericite and/or chlorite.

The AI has two major limitations (Large et al., 2001). Firstly, the index does not take carbonate alteration into account, despite this type of alteration can be significant in some VHMS alteration systems. This may lead to a decrease in the AI, even when alteration intensities are high. Vearncombe (1995) reports in her thesis pervasive carbonate alteration directly subjacent to sulphide mineralisation at Kangaroo Caves. Secondly, the AI effectively measures plagioclase destruction, but does not differentiate chlorite- from sericite-altered rocks, which are two common and major zones of alteration associated with massive sulphide ore. These limitations are overcome by the CCPI of Large et al. (2001). High values of CCPI reflect high FeO and MgO contents, suggesting intense alteration to Fe- and Mg- rich minerals, like chlorite, Fe-Mg bearing carbonates, pyrite, magnetite or hematite. Mafic rocks with high primary FeO and MgO contents typically have CCPI values greater than 50. This might pose a problem in the interpretation of the CCPI-index for mafic rocks. Given the intense alteration of the samples used in the present study, no difficulty is expected.

Figure 6.4 shows that all the volcanic samples have very high AI-values (AI = 90 – 99), except sample p12 (AI = 59), indicating that the samples are intensely chlorite and sericite altered and Na-plagioclase is almost completely broken down. The outlying value of sample p12 will be discussed later. It is possible to distinguish the Al-rich sericite altered rocks from the Al-poor sericite altered rocks. The

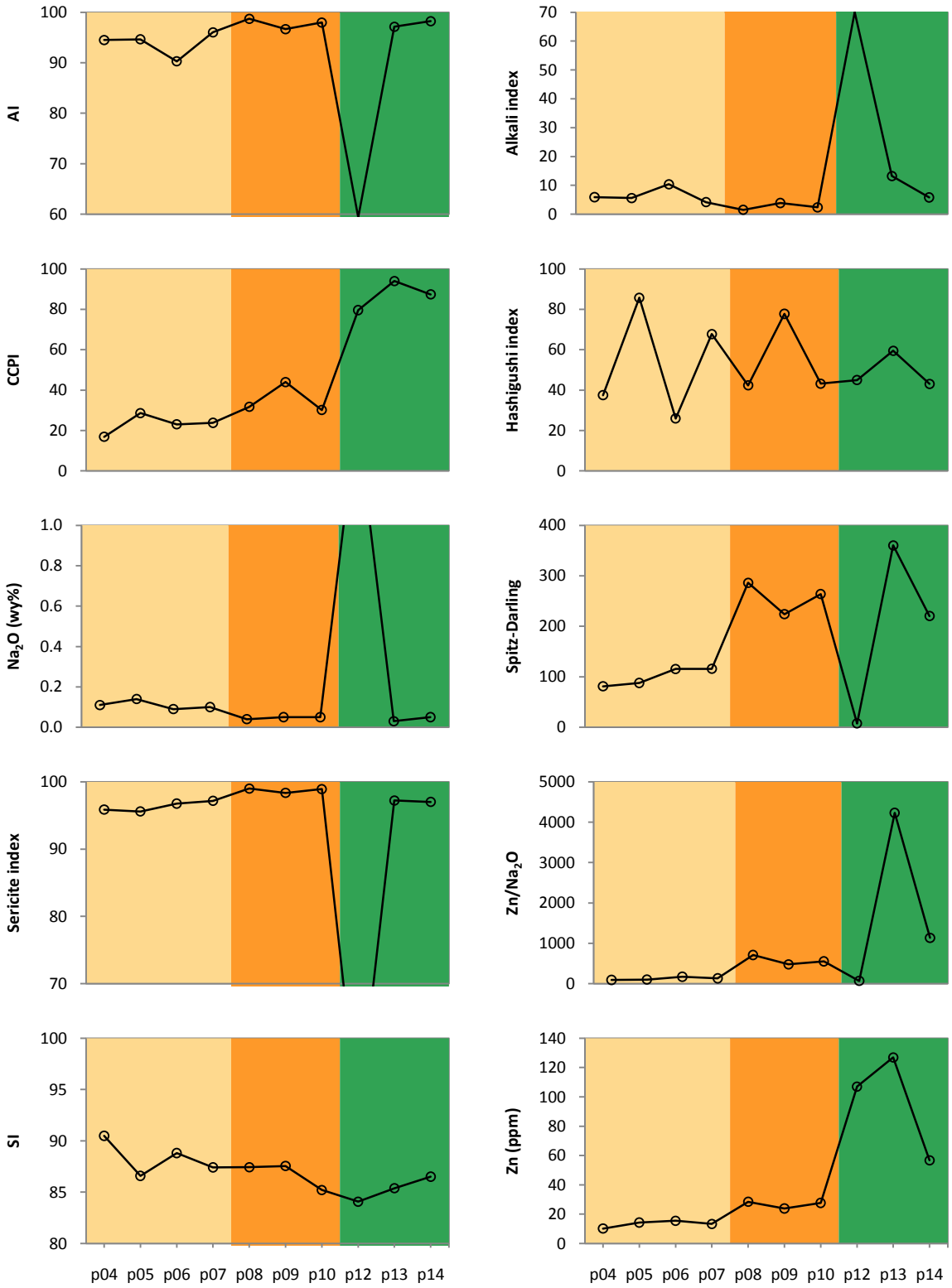

Figure 8.4 Variations in alteration indices values along the transect. The orange area represents the sericite alteration zone with a subdivision between Al-rich sericite (light orange) and Al-poor sericite (dark orange). The green are represents the chlorite alteration zone. Note the different scaling of the vertical axes

slightly higher concentration of Na_2O and lower concentration of MgO gives the Al-rich sericite samples a somewhat lower AI-value compared to the Al-poor sericite samples.

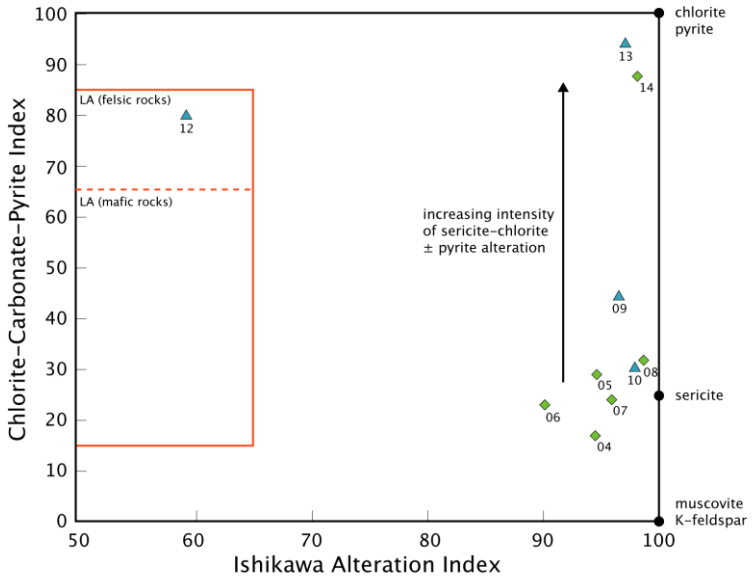

Figure 8.5 AI-CCPI alteration box plot for the 10 volcanic samples after Large et al. (2001). LA marks the least altered field for felsic and mafic rocks. Symbols after this study: *diamonds* = andesites; *triangles* = basalts.

Also for the CCPI the Al-rich sericite samples have lower index values compared to the Al-poor sericite samples. Furthermore, as is also the purpose of the CCPI, chlorite altered samples can easily be distinguished from sericite altered samples by higher index values. In the alteration box plot (Figure 8.5), the samples p13 and p14 from the chlorite alteration zone plot towards the upper-right chlorite corner. The sericite altered samples plot in the lower-right sericite alteration field. The Al-poor sericite samples can also in this plot be distinguished from Al-rich sericite samples.

Sample p12 gives a moderate AI-index of 0.59, which is not in agreement with field results, thin section results and CCPI results that show that the sample is intensely chlorite altered. From the oxides result it is known that only Na_2O, CaO and MnO concentrations for sample p12 are elevated, while the concentrations for the other oxides are in the range of the other (chlorite) altered samples. A reason for the low AI-value can be that the sample is carbonate altered. No evidence is found in the thin sections to corroborate this assumption. However, the carbonate can be too fine grained to detect. This also explains the elevated MnO concentrations. Brauhart (1999) demonstrated with microprobe results that the carbonates can contain up to 10 % $MnCO_3$. The elevated Na_2O, however, cannot be explained with carbonate alteration. Moreover, the carbonate alteration is only restricted to the area just below the VMS-deposit in the Panorama district (Vearncombe, 1995). The Kangaroo Caves deposit is at least 800 m away from sample p12. The presence of other minerals like amphiboles, epidote, actinolite is also not explanatory, because the rock would also be enriched in other elements besides Na_2O and CaO. A last explanation can be a local Ca-Na-Mn-rich fluid passing through the rock at a late stage. No evidence is found in the thin section that supports this. The fluid would probably also be enriched in Cu, as the concentration value for this element is also significantly higher in sample p12 compared to the other samples.

8.3.2 Other alteration indices

The sericte alteration index of assigns high scores to rocks enriched in sericite at the expense of feldspar. All the samples, except p12, have high sericite alteration indices. The Al-rich sericite altered

samples can be distinguished from the Al-poor sericite altered samples by the somewhat lower indices values, caused by higher Na_2O concentration in the samples. Also the chlorite altered samples give very high values. This is probably the result of the complete breakdown of the feldspars, causing the sample to be depleted of Na_2O.

The hashigushi index is a measure of the addition of Fe_2O_3 and designed to differentiate chlorite-rich samples from less altered samples. Hashigushi index values of the volcanic samples differ significantly and show a trivial sawtooth pattern along the transect. The index is unable to distinguish the chlorite-rich samples p12 to p14 from the other samples.

The silicification index (SI) measures Si enrichment or depletion relative to Al. SiO_2 and Al_2O_3 are rarely used in alteration indices, because, as these components dominate igneous rock compositions they are severely affected by closure (Gifkins et al., 2005). Therefore, mass changes in these components are generally obscured. All the volcanic samples have a high SI. There seems to be a weak tendency for the SI to decrease with depth along the volcanic succession.

The Spitz-Darling alteration index is designed to assign high scores to highly altered rocks on the basis of Na depletion associated with feldspar-destructive alteration and the conservation of Al_2O_3. The Spitz-Darling index gives a very clear contrast between Al-rich and Al-poor sericite altered samples, with lower values for the Al-rich sericite altered rocks. This can be attributed to a difference in the Na-concentrations between the Al-rich (Na 0.09 – 0.14 %) and Al-poor (Na 0.04 – 0.05 %) sericite samples. The index is not effective in distinguishing chlorite altered rocks from sericite altered rocks, because values for Al-poor sericite altered rocks are in the same range as chlorite altered rocks, due to a same Na-concentration in both sets of samples. Again, sample p12 gives an outlying value, due to the relatively high Na concentration.

The Zn/Na_2O ratio is based on sphalerite staining and sodium depletion during alteration. The three different alteration zones can easily be distinguished by this ratio. That is especially the result of an increase of Zn along the transect, which shows abrupt changes between different alteration zones.

8.4 Rare earth element geochemistry

The rare earth elements (REEs) comprise the series of elements with atomic numbers 57 to 71, i.e. La to Lu. Elements preceding Gd are called light rare earth elements (LREEs), while elements following Gd are called heavy rare earth elements (HREEs). The REEs all have very similar chemical and physical properties and therefore constitute a unique and coherent group of elements which are not decoupled in geochemical processes. This is due to their equal charges (3+) and similar ionic radii. However, the steady decrease in ionic size with decreasing atomic number, known as the lanthanide contraction, causes fractionation of the REEs relative to each other. It is this phenomenon which is used in geochemistry to investigate complex geological systems and to unravel petrological processes. For hydrothermal systems REE patterns have the potential for delineating interactions between rocks and fluids.

In this study, the REE abundances of the 11 rock samples are normalised to average CI carbonaceous chondrite values as presented by McDonough & Sun (1995). The subscript ‘N’ indicates chondrite-normalised values. The degree of fractionation of the REE, LREE and HREE can be expressed by the

ratios $(La/Yb)_N$, $(La/Sm)_N$ and $(Gd/Yb)_N$, respectively. Europium anomalies are defined quantitatively as:

$$Eu/_{Eu^*} = \frac{Eu_N}{\sqrt{(Sm \cdot Gd)_N}}$$

where *Eu** is the hypothetical concentration that strictly trivalent Eu would have (Taylor & McLennan, 1985). A value greater than 1.0 indicates a positive anomaly whilst a value less than 1.0 is a negative anomaly.

Rare earth element data plotted for the 11 rock samples show all gentle REE slopes (Figure 8.6), which are in accordance with the findings of Vearncombe (1995), Vearncombe & Kerrich (1999) and Brauhart (1999). Inspection of the ratios presented in Table 8.3 reveals that LREEs are more fractionated than HREEs. Furthermore, the volcanic samples p04 and p05, located at the top of the volcanic succession, have much higher $(La/Yb)_N$ ratio values than the other deeper-lying volcanic samples. This observation is in complete contrast to the findings of Vearncombe (1995), Vearncombe & Kerrich (1999) and Brauhart (1999). These authors report a progressive decrease in the fractionation of the REEs with elevation in the volcanic succession. To explain this discrepancy would require detailed examination of the REE data reported by these authors, which is beyond the scope of this study.

The volcanic samples all show pronounced negative Eu anomalies except for sample p13 which lacks an Eu anomaly. Chert sample p03 shows in contrast a positive Eu anomaly. There seems to be no consistency in the amplitude of the negative Eu anomalies of the volcanic samples along the transect. Eu is the only REE which can exist in both the 3+ oxidation state and 2+ oxidation state depending on the oxygen activity. Europium forms Eu^{2+} at low oxygen activities and Eu^{3+} at high oxygen activities. In the divalent state Eu is compatible in plagioclase and K-feldspar in contrast to the trivalent REEs which are incompatible. Thus, under reducing conditions Eu partition coefficients for plagioclase and K-feldspar are high (generally > 1.0) and anomalous relative to the other REEs, whereas under oxidising conditions partition coefficients for Eu are low and Eu behaves in a similar way to the other REEs (Drake & Weill, 1975). Petrographic examination of the thin sections from the volcanic samples

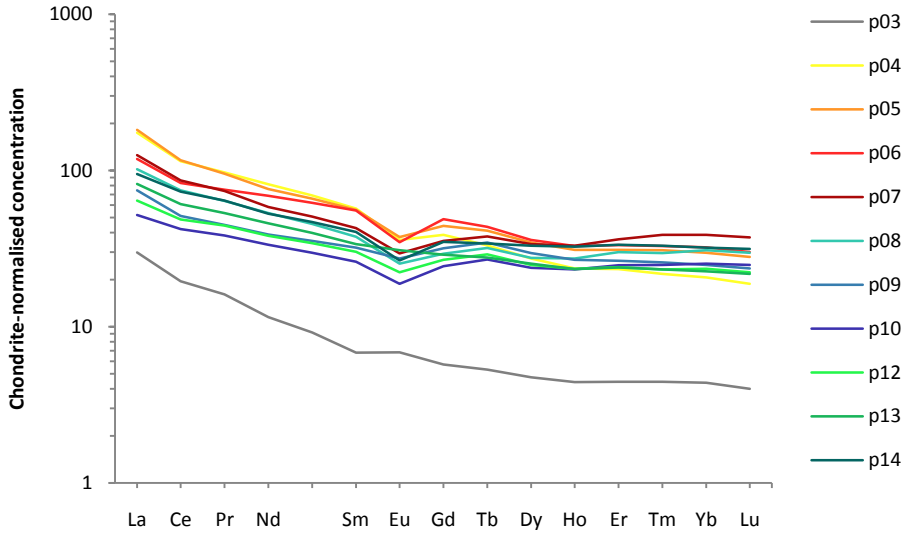

Figure 8.6 Chondrite-normalised plot of REE concentrations for the 11 collected rock samples. For all 14 natural occurring REEs analytical results were obtained. Normalisation values are after McDonough & Sun (1995).

Table 8.3 Summary of relevant chondrite-normalised (McDonough & Sun, 1995) REE ratios for the 11 collected rock samples. See text for explanation of the ratios.

	p03	**p04**	**p05**	**p06**	**p07**	**p08**	**p09**	**p10**	**p12**	**p13**	**p14**
$(La/Yb)_N$	6.8	8.5	6.1	3.7	3.2	3.3	3.0	2.1	2.7	3.6	3.0
$(La/Sm)_N$	4.4	3.1	3.2	2.1	2.9	2.7	2.3	2.0	2.1	2.4	2.4
$(Gd/Yb)_N$	1.3	1.9	1.5	1.5	0.9	0.9	1.3	1.0	1.1	1.3	1.1
Eu/Eu*	1.10	0.76	0.75	0.67	0.76	0.76	0.86	0.74	0.79	0.99	0.71

shows partly to completely replaced feldspar ranging in size from small crystals in the groundmass to large phenocrysts (Chapter 5). As feldspar is one of the main primary constituents of the volcanic samples it would be expected that the resulting chondrite-normalised REE patterns show no or positive Eu anomalies depending on the oxygen activity during crystallisation.

In section 8.2 it is demonstrated that the HREE Er, Tm, Yb and Lu have behaved as essentially immobile during hydrothermal alteration and sub-greenschist facies metamorphism in the Panorama district. On the contrary, the other REE have been mobilised and the variable $(La/Yb)_N$ ratios of the volcanic samples are interpreted to reflect mobility during hydrothermal alteration. Also the observed negative Eu anomalies are assumed to be a product of REE mobility. This is a more specific explanation for the negative Eu anomalies than the interpretation by Vearncombe (1995) of, in part, secondary induced mobility of Eu. The degree of REE mobility depends, among other factors, on the temperature (Bau, 1991). A high temperature promotes REE leaching from the host rock and REE mobility can both increase or decrease towards the heavier REEs. The latter, greater mobility of the LREE, is applicable to the study area and similar to that described in other VMS districts (e.g. Liaghat & MacLean, 1995). The relative steep REE patterns (i.e. relative high $(La/Yb)_N$ ratios) of the samples p04 and p05 are regarded to most closely represent primary REE patterns before alteration. With increasing temperature the loss of LREE from the rock towards the altering fluid increases resulting in a modification of the slopes of the REE patterns of the volcanic samples towards more neutral slopes and REE patterns become less fractionated.

Kikawada et al (2001) conducted an experiment on the alteration of andesitic rocks by acidic hot spring water under relative mild conditions representative for the subsurface of volcanic areas. The study shows that the LREEs are more readily leached out than the HREEs, as is also applicable to this study. Furthermore, positive Eu anomalies flip to negative Eu anomalies as rock alteration proceeds. The negative Eu anomalies of the volcanic samples can therefore be explained by hydrothermal alteration. The positive Eu anomaly for sample p03 could indicate that part of the REEs are precipitated in the chert.

The REE content of alteration fluids from mid-ocean ridges and geothermal fields in volcanic areas are both extremely low (Bau, 1991; Klinkhammer et al., 1994; Kikawada et al., 2001). Therefore, as also suggested by Bau (1991), to affectively alter REE patterns of volcanic rocks high water/rock ratios are required during hydrothermal fluid-rock interaction. However, as already mentioned, also temperature is one of the factors controlling REE patterns. Nevertheless, the hydrothermal system at Panorama is regarded as a high fluid-rock ratio system. This is in agreement with other papers in which the Panorama district is mentioned as a high fluid-rock ratio hydrothermal system (Brauhart et al., 2000; 2001; Schardt et al., 2005).

Chapter 9: Discussion

9.1 Alteration facies in the Kangaroo Caves footwall

As part of his PhD research, Brauhart (1999) has conducted detailed field mapping and additional analyses of collected rock samples of the fossil Archaean submarine hydrothermal system at the Panorama district. This has resulted in, among other things, an alteration map of the Panorama district published in the paper of Brauhart et al. (1998). Four major alteration facies have been identified in the volcanic succession and underlying granite of the Panorama district by these authors (Section 2.3). The distribution of the alteration facies is interpreted to be the result of convective hydrothermal circulation most likely related to the intrusion of the Strelley Granite. In the footwall to the Kangaroo Caves VMS deposit, the semi-conformable feldspar-sericite-quartz alteration zone is crosscut by a broad corridor of chlorite-quartz alteration (Figure 9.1). The semi-conformable alteration zone is interpreted as broad areas of fluid recharge with increasing temperature towards the Strelley Granite, while the corridor marks pathways of high temperature discharge fluids (Brauhart et al., 2000). The transect of rock samples collected by Hein & Van Ruitenbeek (Appendix 1) in the Kangaroo Caves area runs from the top of the volcanic succession downwards (Figure 9.1). According to the alteration map of Brauhart et al. (1998) the transect intersects the feldspar-sericite-quartz alteration zone as well as the chlorite-quartz alteration zone (Table 9.1).

Van Ruitenbeek et al. (2005) revised the alteration classification of Brauhart et al. (1998) based on new information obtained by short wavelength infrared spectroscopy. The only modification of interest to this study is the newly defined quartz-sericite alteration facies, which forms a subgroup of the feldspar-sericite-quartz alteration facies of Brauhart et al. (1998). The quartz-sericite alteration facies is characterised by complete replacement of feldspar to sericite and quartz, in contrast to the feldspar-sericite-quartz alteration facies. The quartz-sericite alteration facies occurs at the top of the

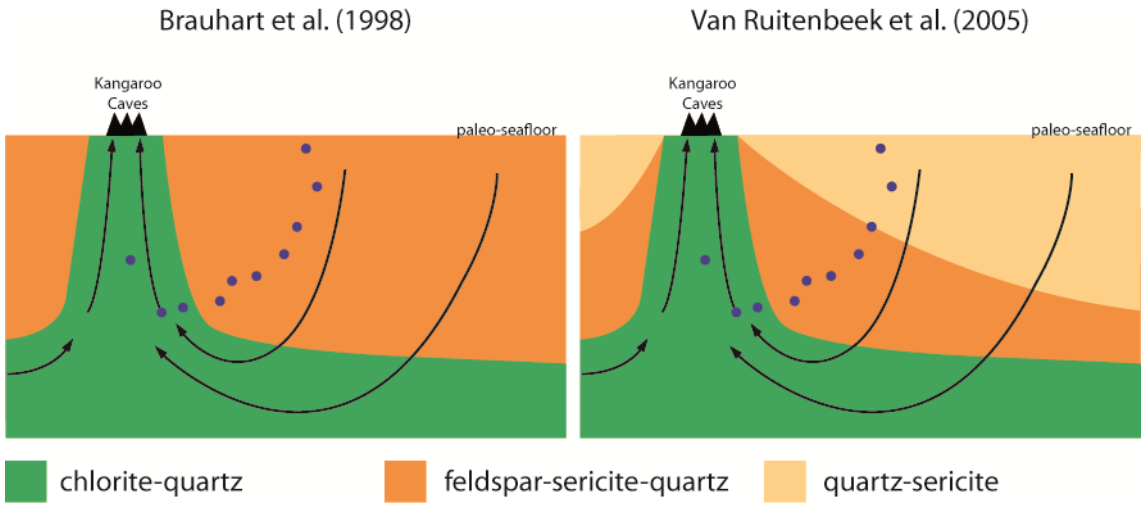

Figure 9.1 Schematic and simplified cross sections through the footwall of the Kangaroo Caves VMS deposit showing the distribution of alteration zones according to the paper of Brauhart et al. (1998) and Van Ruitenbeek et al. (2005). Arrows indicate fluid pathways during regional-scale alteration. Purple dots approximate the position of the sample localities along the volcanic succession.

Table 9.1 Summary of several different properties of the 11 transect samples.

Sample No.	Alteration facies according to:		Spectral parameters derived from airborne spectra (Van Ruitenbeek et al., 2006)		Spectral parameters derived from field sample laboratory spectra			Primary rock type according to the present study
	Brauhart et al. (1998)	Van Ruitenbeek et al. (2005)	white mica probability	absorption λ (nm)	WMAI	absorption λ (nm)	Interpreted mineralogy	
p03	silicified	---	0.19	2211	0.93	2199	quartz	chert
p04	feldspar-sericite-qtz	quartz-sericite	1	2205	1	2198	white mica	andesite
p05	feldspar-sericite-qtz	quartz-sericite	1	2201	1	2199	white mica	andesite
p06	feldspar-sericite-qtz	quartz-sericite	1	2201	1	2201	white mica	andesite
p07	feldspar-sericite-qtz	quartz-sericite	0.98	2205	1	2198	white mica	andesite
p08	feldspar-sericite-qtz	feldspar-sericite-qtz	0.99	2216	1	2212	white mica	andesite
p09	feldspar-sericite-qtz	feldspar-sericite-qtz	1	2213	1	2208	white mica	basalt
p10	feldspar-sericite-qtz	feldspar-sericite-qtz	0.99	2214	1	2211	white mica	basalt
p12	chlorite-quartz	chlorite-quartz	0.96	2212	0.60	2207	white mica + chlorite	basalt
p13	chlorite-quartz	chlorite-quartz	0.57	2206	0.44	2207	chlorite + white mica	basalt
p14	chlorite-quartz	chlorite-quartz	0.66	2207	0.53	2206	chlorite + white mica	andesite

volcanic succession underlying the Marker Chert and overlying the feldspar-sericite-quartz alteration zone (Figure 9.1). Both the quartz-sericite and feldspar-sericite-quartz alteration facies are spectrally dominated by absorption features of white mica. Diagnostic absorption features of white mica occur between 2180–2228 nm and near 2344 nm and 2440 nm, and are associated with Al-OH (Pontual et al., 1997b) (Figure 4.2). The wavelength position of the main Al-OH absorption feature near 2200 nm of white mica varies with composition. White mica from the quartz-sericite alteration zone shows short absorption wavelengths (<2205 nm), while the feldspar-sericite-quartz alteration zone contains white mica of long absorption wavelengths (>2208 nm). Consequently, these two alteration facies can be easily recognised and distinguished by field and airborne imaging spectroscopy. Van Ruitenbeek et al. (2006) created two images for the Panorama district using airborne derived reflectance spectra. An image representing the probability, ranging from 0 to 1, of white mica being present and an image showing the wavelength position of the 2200 nm absorption feature of white mica (Figure 4.1). Based on these two images the alteration facies of the transect samples in Table 9.1 can be reclassified according to the paper of Van Ruitenbeek et al (2005).

Brauhart et al. (1998) also defines a completely feldspar-destructive alteration facies characterised by a quartz-sericite assemblage. This by Brauhart et al. (1998) so-called sericite-quartz alteration facies is petrographically similar to the quartz-sericite alteration facies of Van Ruitenbeek et al. (2005). However, while the quartz-sericite alteration zone occurs at the top of the volcanic succession, sericite-quartz alteration is in general observed near the base of the volcanic succession and in upper parts of the Strelley Granite. Only near the Man O'War prospect a zone of sericite-quartz alteration is mapped at the top of the volcanic succession by Brauhart et al. (1998) (Figure 2.3). Airborne imaging spectrometry shows that the rocks affected by sericite-quartz alteration at Man O'War contain long-wavelength white mica (Van Ruitenbeek, 2007). This is in contrast to the quartz-sericite alteration facies of Van Ruitenbeek et al. (2005) which is characterised by short-wavelength white mica. So, although petrographically maybe similar the quartz-sericite and sericite-quartz alteration facies are spatially and spectrally distinctively different.

9.2 Validation of the alteration mineralogy

The reclassification of the alteration facies for the transect samples after the paper of Van Ruitenbeek et al. (2005) is based on spectral parameters derived from two images of the Panorama district presented in the paper of Van Ruitenbeek et al. (2006). The two images have been created using airborne derived reflectance spectra. Airborne spectra can possibly differ from field sample laboratory spectra as a result of several factors. The presence of vegetation and weathering material in the area, inhomogeneous mineralogy in the resolution cell are some of these factors. Therefore, laboratory spectra are obtained from the transect samples for verification. Examination of the field sample laboratory spectra reveal that white mica and chlorite are the only minerals spectrally present in the rocks (Table 9.1). Despite the possible errors the estimated spectral parameters derived from the two images of Van Ruitenbeek et al. (2006) show satisfactory correlation with the measured values in the rock samples. The abrupt change in the wavelength position of the main Al-OH absorption feature of white mica is also observed in the samples. Based on the field sample laboratory spectra the reclassified alteration facies of the transect samples is confirmed

Subsequently interpretations of the reflectance spectra are validated by thin section petrography. The white mica rich samples p04 to p10 have been extensively silicified and sericitic altered (Table 9.2).

Table 9.2 Summary of several different properties of the 7 white mica rich samples.

Sample No.	Absorption λ (nm)	Thin section petrography			Average white mica composition	Primary rock type
		Alteration type	Alteration intensity	Feldspar destruction		
p04	2198	sericitic	moderate	near-complete	$K_{1.55}Na_{0.08}Al_{3.88}Mg_{0.16}Fe_{0.07}[Al_{1.75}Si_{6.25}O_{20}](OH)_4$	andesite
p05	2199	sericitic	strong	complete	$K_{1.54}Na_{0.07}Al_{3.87}Mg_{0.12}Fe_{0.08}[Al_{1.68}Si_{6.32}O_{20}](OH)_4$	andesite
p06	2201	sericitic	strong	complete	$K_{1.51}Na_{0.05}Al_{3.84}Mg_{0.17}Fe_{0.09}[Al_{1.64}Si_{6.36}O_{20}](OH)_4$	andesite
p07	2198	sericitic	strong	complete	$K_{1.66}Na_{0.06}Al_{3.84}Mg_{0.12}Fe_{0.09}[Al_{1.70}Si_{6.30}O_{20}](OH)_4$	andesite
p08	2212	sericitic	strong	complete	$K_{1.52}Al_{3.50}Mg_{0.40}Fe_{0.21}[Al_{1.32}Si_{6.68}O_{20}](OH)_4$	andesite
p09	2208	sericitic	strong	complete	$K_{1.56}Al_{3.77}Mg_{0.22}Fe_{0.09}[Al_{1.58}Si_{6.42}O_{20}](OH)_4$	basalt
p10	2211	sericitic	intense	complete	$K_{1.41}Al_{3.48}Mg_{0.43}Fe_{0.22}[Al_{1.25}Si_{6.75}O_{20}](OH)_4$	basalt

Because of the pervasive alteration of the rocks the primary mineralogy was difficult to determine. Nevertheless, the shape of some of the phenocrysts and minerals in the groundmass suggest that feldspar was the primary mineral before alteration. On this basis the sericitic alteration of the samples was completely feldspar destructive. Only for sample p04 feldspar laths in the groundmass are partly replaced by sericite and feldspar destruction is near-complete.

These petrographic findings are not in agreement with the petrographic descriptions of the alteration facies defined by both Brauhart et al. (1998) and Van Ruitenbeek et al. (2005). All the feldspar in the thin sections has been completely replaced. Therefore, the finding of Van Ruitenbeek et al. (2005) that the wavelength position of the 2200 nm absorption feature of white mica is related to the completeness of feldspar destruction is by this study refuted.

9.3 White mica characteristics

In his study Beran (2002) demonstrated that the exact 2200 nm wavelength position of white mica varies as a function of the Al content. Electron microprobe analyses performed on the samples p04 to p10 indeed show that the 2200 wavelength position is negatively correlated with the Al content. It is often assumed that the variations in Al content are the result of tschermak substitution where Al is replaced by Fe and Mg (Duke, 1994). Variations in the Al content of the white mica at Panorama are the result of tschermak substitution and pyrophyllitic substitution. Another substitution which has only minorly affected the white mica composition is the paragonitc substitution. Laser ablation ICP-MS analyses on white mica show that trace elements are only present in trace amounts in white mica and do not contribute significantly to the white mica composition. Immobile element plots have shown that Al has behaved as essentially immobile during hydrothermal alteration at a rock scale (Section 8.2). A possible source, or sink, of Al required by the tschermak substitution is therefore the surrounding. A fluid source can at least be excluded, otherwise Al would be mobile.

To determine the main factors controlling variations in the white mica composition at the Panorama district has been very difficult. This problem is not only applicable for the Panorama district, but for hydrothermal systems in general. Compositional variations in white mica for metamorphic systems have been extensively studied and are a function of the temperature, pressure and to some extent bulk-rock composition. For hydrothermal systems also factors like fluid chemistry, fluid pressure and the water-rock ratio play a role in the white mica composition and these factors are less well defined. Furthermore, conditions during metamorphism are generally of another order of magnitude compared to a hydrothermal system and between different hydrothermal systems there are inconsistencies in the white mica composition. Despite, these problems it is assumed that the white mica composition of the Panorama district is related to the temperature. Maybe the best argument comes from the Sr concentration in white mica. The Sr concentration in white mica shows a decreasing trend with relative high concentrations for sample p04 to low concentrations for sample p09 and p10. This decrease is the result of a loss of Sr from the white mica structure by diffusion controlled by the temperature. Variations in white mica composition at the Panorama district are in no case controlled by host rock lithology. Immobile elements show that the division between andesite-basalt and dacite mapped by Brauhart et al. (1998) and Brauhart (1999) does not coincide with the transition from Al rich to Al poor white mica (Table 9.2).

9.4 Conclusions

The following final conclusions can be drawn from the present study:

- The abrupt change in the wavelength position of the main Al-OH absorption feature of white mica near 2200 nm observed both in field and airborne reflectance spectra is the effect of the Al content in white mica.
- The Al content in white mica is not a function of the completeness of feldspar destruction.
- Variations in the Al content of the white mica are the result of the tschermak substitution and phyrophyllitic substitution.
- A fluid source for the Al in white mica can be excluded, as Al has behaved as essentially immobile during hydrothermal alteration.
- The primary host rock lithology is not controlling the white mica composition.

References

Bau, M., 1991, Rare-earth element mobility during hydrothermal and metamorphic fluid-rock interaction and the significance of the oxidation state of europium. *Chemical Geology*, v. 93, p. 219–230

Beran, A., 2002, Infrared spectroscopy of micas. *In:* Mottana, A., Sassi, F.P., Thompson, J.B., Jr. & Guggenheim, S. (Eds.), *Micas: Crystal Chemistry and Metamorphic Petrology*. Reviews in Mineralogy & Geochemistry, Mineralogical Society of America, v. 46, p. 351–369

Brauhart, C.W., 1999, *Regional alteration systems associated with Archean volcanogenic massive sulfide deposits at Panorama, Pilbara, Western Australia*. University of Western Australia, PhD thesis (unpublished), 194 p.

Brauhart, C.W., Groves, D.I. & Morant, P., 1998, Regional alteration systems associated with volcanogenic massive sulfide mineralization at Panorama, Pilbara, Western Australia. *Economic Geology*, v. 93, p. 292–302

Brauhart, C.W., Huston, D.L. & Andrew, A.S., 2000, Oxygen isotope mapping in the Panorama VMS district, Pilbara Craton, Western Australia: Applications to estimating temperatures of alteration and to exploration. *Mineralium Deposita*, v. 35, p. 727–740

Brauhart, C.W., Huston, D.L., Groves, D.I., Mikucki, E.J. & Gardoll, S.J., 2001, Geochemical mass-transfer patterns as indicators of the architecture of a complete volcanic-hosted massive sulfide hydrothermal alteration system, Panorama district, Pilbara, Western Australia. *Economic Geology*, v. 96, p. 1263–1278

Brigatti, M.F. & Guggenheim, S., 2002, Mica crystal chemistry and the influence of pressure, temperature, and solid solution on atomistic models. *In:* Mottana, A., Sassi, F.P., Thompson, J.B., Jr. & Guggenheim, S. (Eds.), *Micas: Crystal Chemistry and Metamorphic Petrology*. Reviews in Mineralogy & Geochemistry, Mineralogical Society of America, v. 46, p. 1–97

Buick, R., Brauhart, C.W., Morant, P., Thornett, J.R., Maniw, J.G., Archibald, N.J., Doepel, M.G., Fletcher, I.R., Pickard, A.L., Smith, J.B., Barley, M.E., McNaughton, N.J., & Groves, D.I., 2002, Geochronology and stratigraphic relationships of the Sulphur Springs Group and Strelley Granite: a temporally distinct igneous province in the Archaean Pilbara Craton, Australia. *Precambrium Research*, v. 114, p. 87–120

Cathelineau, M. & Izquierdo, G., 1988, Temperature – composition relationships of authigenic micaceous minerals in the Los Azufres geothermal system. *Contributions to Mineralogy and Petrology*, v. 100, p. 418–428

Clark, R.N., 1999, Spectroscopy of rocks and minerals, and principles of spectroscopy: *in* Manual of remote sensing, volume 3, remote sensing for the earth sciences (3rd edition) *edited by* Rencz, A.N.: John Wiley & Sons, New York, pp. 3–58

Clark, R.N., King, T.V.V., Klejwa, M., Swayze, G. & Vergo, N., 1990, High spectral resolution reflectance spectroscopy of minerals. *Jorunal of Geophysical Research*, v. 95, p. 12653–12680

Cuday, T.J., Okada, K. & Brauhart, C., 2000, Targeting VMS-style Zn mineralisation at Panorama, Australia, using airborne hyperspectral VNIR-SWIR HYMAP data: *in* ERIM Proceedings of the 14th International Conference on Applied Geologic Remote Sensing, Las Vegas, pp. 395–402

Cudahy, T.J., Okada, K., Ueda, K., Brauhart, C., Morant, P., Huston, D., Cocks, T., Wilson, J., Mason, P. & Huntington, J.F., 1999, Mapping the Panorama VMS-style alteration and host rock mineralogy, Pilbara Block, using airborne hyperspectral VNIR-SWIR data: MERIWA Report 205, 107 p.

Cudahy, T. & Quigley, M., 2004, Panorama: *in* Evaluation of the EO-1 Hyperion hyperspectral instrument and its applications at Australian validation sites 2001-2003 *edited by* Jupp, D.L.B. & Datt, B.: CSIRO Earth Observation Centre Report 2004/06, pp. 150–160

Dalla Torre, M., Livi, K.J.T., Veblen, D.R. & Frey, M., 1996, White K-mica evolution from phengite to muscovite in shales and shale matrix melange, Diablo Range, California. *Contributions to Mineralogy and Petrology*, v. 123, p. 390–405

Deer, W.A., Howie, R.A. & Zussman, J., 1992, An introduction to the rock-forming minerals (2nd edition): Longman Scientific & Technical, Harlow, 696 p.

Drake, M.J. & Weill, D.F., 1975, Partition of Sr, Ba, Ca, Y, Eu^{2+}, Eu^{3+}, and other REE between plagioclase feldspar and magmatic liquid: an experimental study. *Geochimica et Cosmochimica Acta*, v. 39, p. 689–712

Drieberg, S.L., 2003, *The magmatic-hydrothermal architecture of the Archean Volcanic Massive Sulfide (VMS) System at Panorama, Pilbara, Western Australia*. University of Western Australia, PhD thesis (unpublished), 327 p.

Duke, E.F., 1994, Near infrared spectra of muscovite, Tschermak substitution, and metamorphic reaction progress: Implications for remote sensing. *Geology*, v. 22, p. 621–624

Eilu, P., Groves, D.I., Mikucki, E.J., McNaughton, N.J. & Ridley, J.R., 1995, Alteration indices and pathfinder elements in wallrock alteration zones around Archaean lode-gold deposits. *In:* Pašava, J., Kříbek, B. & Žák, K. (Eds.), *Mineral Deposits: From their Origin to their Environmental Impacts*. Proceedings of the Third Biennial SGA Meeting, A.A. Balkema, Amsterdam, p. 113–116

Faure, G., 1986, *Principles of Isotope Geology*, 2nd Edition. John Wiley & Sons, New York, p. 589

Finlow-Bates, T. & Stumpfl, E.F., 1981, The behaviour of so-called immobile elements in hydrothermally altered rocks associated with volcanogenic submarine-exhalative ore deposits. *Mineralium Deposita*, v. 16, p. 319–328

Fleet, M.E., 2003, *Sheet silicates: micas* (2nd edition): vol. 3A *of* Rock-forming minerals: The Geological Society, London, 758 p.

Franklin, J.M., 1997, Lithogeochemical and mineralogical methods for base metal and gold exploration. *In:* Gubins, A.G. (Ed.), *Proceedings of Exploration 97: Fourth Decennial International Conference on Mineral Exploration*. Prospectors and Developers Association of Canada, p. 191–208

Freeman, S.R., Inger, S., Butler, R.W.H. & Cliff, R.A., 1997, Dating deformation using Rb-Sr in white mica: Greenschist facies deformation ages from the Entrelor shear zone, Italian Alps. *Tectonics*, v. 16, p. 57–76

Gifkins, C., Herrmann, W. & Large, R., 2005, *Altered volcanic rocks: A guide to description and interpretation*. Centre for Ore Deposit Research, University of Tasmania, 275 p.

Guidotti, C.V. & Sassi, F.P., 1998a, Petrogenetic significance of Na-K white mica mineralogy: Recent advances for metamorphic rocks. *European Journal of Mineralogy*, v. 10, p. 815–854

Guidotti, C.V. & Sassi, F.P., 1998b, Miscellaneous isomorphous substitutions in Na-K white micas: A review with special emphasis to metamorphic micas. *Scienze Fisiche e Naturali*, v. 9, p. 57–78

Guidotti, C.V. & Sassi, F.P., 2002, Constraints on studies of metamorphic K-Na white micas. *In:* Mottana, A., Sassi, F.P., Thompson, J.B., Jr. & Guggenheim, S. (Eds.), *Micas: Crystal Chemistry and Metamorphic Petrology*. Reviews in Mineralogy & Geochemistry, Mineralogical Society of America, v. 46, p. 413–448

Hickman, A.H., 1983, Geology of the Pilbara Block and its environs: Western Australia Geological Survey, Bulletin 127, 268p.

Huston, D.L., Kamprad, J., & Brauhart, C., 1997, Preliminary results of PIMA analyses of the alteration zone underlying the Sulphur Springs deposit, Panorama district, Pilbara Block, Western Australia: Australian Geological Survey Organisation, Record 1997/14, 36p.

Jarvis, K.E., 1989, Determination of rare earth elements in geological samples by inductively coupled plasma mass spectrometry. *Journal of Analytical Atomic Spectrometry*, v. 4, p. 563–570

Jochum, K.P., Stoll, B., Herwig, K., Willbold, M., Hofmann, A.W., Amini, M., Aarburg, S., Abouchami, W., Hellebrand, E., Mocek, B., et al., 2006, MPI-DING reference glasses for in situ microanalysis: New reference values for element concentrations and isotope ratios. *Geochemistry Geophysics Geosystems*, v. 7, 44 p.

Kikawada, Y., Ossaka, T., Oi, T. & Honda, T., 2001, Experimental studies on the mobility of lanthanides accompanying alteration of andesite by acidic hot spring water. *Chemical Geology*, v. 176, p. 137–149

Klinkhammer, G.P., Elderfield, H., Edmond, J.M. & Mitra, A., 1994, Geochemical implications of rare earth element patterns in hydrothermal fluids from mid-ocean ridges. *Geochimica et Cosmochimica Acta*, v. 58, p. 5105–5113

Large, R.R., Gemmell, J.B., Paulick, H. & Huston, D.L., 2001, The alteration box plot: A simple approach to understanding the relationship between alteration mineralogy and lithogeochemistry associated with volcanic-hosted massive sulfide deposits. *Economic Geology*, v. 96, p. 957–971

Liaghat, S. & MacLean, H., 1995, Lithogeochemistry of altered rocks at the New Insco VMS deposit, Noranda, Quebec. *Journal of Geochemical Exploration*, v. 52, p. 333–350

MacLean, W.H. & Barrett, T.J., 1993, Lithogeochemical techniques using immobile elements. *Journal of Geochemical Exploration*, v. 48, p. 109–133

McDonough, W.F. & Sun, S.-s., 1995, The composition of the earth. *Chemical Geology*, v. 120, p. 223–253

Mottana, A., Sassi, F.P., Thompson, J.B., Jr. & Guggenheim, S., 2002 *Micas: Crystal Chemistry and Metamorphic Petrology*. Reviews in Mineralogy & Geochemistry, Mineralogical Society of America, v. 46, 499 p.

Nebel, O., Mezger, K., Scherer, E.E. & Münker, 2005, High precision determinations of $^{87}Rb/^{85}Rb$ in geologic materials by MC-ICP-MS. *International Journal of Mass Spectrometry*, v. 246, p. 10–18

Pearce, J.A., 1996, A user's guide to basalt discrimination diagrams. *In:* Wyman, D.A. (Ed.), *Trace Element Geochemistry of Volcanic Rocks: Applications for Massive Sulphide Exploration*. Geological Association of Canada, short course notes, v. 12, p. 79–113

Pearce, N.J.G., Perkins, W.T., Westgate, J.A., Gorton, M.P., Jackson, S.E., Neal, C.R. & Chenery, S.P., 1997, A compilation of new and published major and trace element data for NIST SRM 610 and NIST SRM 612 glass reference materials. *Geostandards and Geoanalytical Research*, v. 21, p. 115–144

Pontual, S., Merry, N. & Gamson, P., 1997a, *Spectral interpretation field manual* (vol. 1). AusSpec International, Australia

Pontual, S., Merry, N. & Gamson, P., 1997b, *Volcanic-hosted massive sulphide systems* (vol. 7). AusSpec International, Australia

Rieder, M., 2001, Mineral nomenclature in the mica group: The promise and the reality. *European Journal of Mineralogy*, v. 13, p. 1009–1012

Rieder, M., Cavazzini, G., D'Yakonov, Y.S., Frank-Kamenetskii, V.A., Gottardi, G., Guggenheim, S., Koval, P.V., Müller, G., Neiva, A.M.R., Radoslovich, E.W., Robert, J.-L., Sassi, F.P., Takeda, H., Weiss, Z. & Wones, D.R., 1998, Nomenclature of the micas. *The Canadian Mineralogist*, v. 36, p. 905–912

Schardt, C., Yang, J. & Large, R., 2005, Numerical heat and fluid-flow modelling of the Panorama volcanic-hosted massive sulfide district, Western Australia. *Economic Geology*, v. 100, p.547–566

Shelley, D., 1993, *Igneous and metamorphic rocks under the microscope: Classification, textures, microstructures and mineral preferred orientations*. Chapman & Hall, London, 445 p.

Siivola, J. & Schmid, R., 2007, List of mineral abbreviations: *in* Metamorphic rocks: a classification and glossary of terms *edited by* Fettes, D. & Desmons, J.: Cambridge University Press, recommendations of the international union of geological sciences subcommission on the systematics of metamorphic rocks, p. 93–110

Smith, R.-K., 2001, *Interpretation of inorganic data*. Genium Publishing Corporation, Amsterdam, New York, 138 p.

Spear, F.S., 1993, *Metamorphic phase equilibria and pressure-temperature-time paths*. Mineralogical Society of America, Monograph, 799 p.

Suryantini, S.E., Van Ruitenbeek, F.J.A. & Van der Meer, F.D., 2005, The effect of weathering on reflectance spectra of hydrothermal white micas and chlorites: Implications for alteration mapping. *In:* Mao, J. (Ed), *Mineral Deposit Research*. Proceedings of the 8th Biennial SGA Meeting, Beijing, p. 703–706

Taylor, S.R. & McLennan S.M., 1985, *The continental crust: Its composition and evolution*. Blackwell, Oxford, 312 p.

Thomsen, V., Schatzlein, D. & Mercuro, D., 2003, Limits of detection in spectroscopy. *Spectroscopy*, v. 18, p. 112–114

Van Achterbergh, E., Ryan, C.G. & Griffin, W.L., 2001, GLITTER user's manual: On-line interactive data reduction for the LA-ICPMS microprobe. GEMOC, Version 4, 72 p.

Van Kranendonk, M.J., 2000, Geology of the North Shaw 1:100 000 sheet: Western Australia Geological Survey, 1:100 000 Geological Series Explanatory Notes, 86 p.

Van Kranendonk, M.J., Hickman, A.H., Smithies, R.H., Nelson, D.R., & Pike, G., 2002, Geology and tectonic evolution of the Archean North Pilbara terrain, Pilbara Craton, Western Australia. *Economic Geology*, v. 97, p. 695–732

Van Kranendonk, M.J., Hickman, A.H., Smithies, R.H., Williams, I.R., Bagas, L., & Farrell, T.R., 2006, Revised lithostratigraphy of Archean supracrustal and intrusive rocks in the northern Pilbara Craton, Western Australia. *Western Australia Geological Survey*, Record 2006/15, 57 p.

Van Kranendonk, M.J., Hickman, A.H., Williams, I.R., & Nijman, W., 2001, Archaean geology of the East Pilbara Granite-Greenstone Terrane, Western Australia ─ a field guide. *Western Australia Geological Survey*, Record 2001/9, 134 p.

Van Ruitenbeek, F.J.A., 2007, *Hydrothermal processes in the Archean: New insights from imaging spectroscopy*. International Institute for Geo-Information Science and Earth Observation, Enschede, PhD-thesis, 114 p.

Van Ruitenbeek, F.J.A., Cudahy, T., Hale, M. & Van der Meer, F.D., 2005, Tracing fluid pathways in fossil hydrothermal systems with near-infrared spectroscopy. *Geology*, v. 33, p. 597–600

Van Ruitenbeek, F.J.A., Debba, P., Van der Meer, F.D., Cudahy, T., Van der Meijde, M. & Hale, M., 2006, Mapping white micas and their absorption wavelengths using hyperspectral band ratios. *Remote Sensing of Environment*, v. 102, p. 211–222

Vearncombe, S.E., 1995, *Volcanogenic massive sulphide-sulphate mineralisation at Strelley, Pilbara Craton, Western Australia*. University of Western Australia, PhD thesis (unpublished), 153 p.

Vearncombe, S., Barley, M.E., Groves, D.I., McNaughton, N.J., Mikucki, E.J., & Vearncombe, J.R., 1995, 3.26 Ga black smoker-type mineralization in the Strelley Belt, Pilbara Craton, Western Australia: *Journal of the Geological Society*, London, v. 152, p. 587–590

Vearncombe, S. & Kerrich, R., 1999, Geochemistry and geodynamic setting of volcanic and plutonic rocks associated with Early Archaean volcanogenic massive sulphide mineralization, Pilbara Craton. *Precambrian Research*, v. 98, p. 243–270

Vearncombe, S., Vearncombe, J.R., & Barley, M.E., 1998, Fault and stratigraphic controls on volcanogenic massive sulphide deposits in the Strelley Belt, Pilbara Craton, Western Australia. *Precambrian Research*, v. 88, p. 67–82

Wickman, F.E., Åberg, G. & Levi, B., 1983, Rb-Sr dating of alteration events in granitoids. *Contributions to Mineralogy and Petrology*, v. 83, p. 358–362

Williams, H., Turner, F.J. & Gilbert, C.H., 1982, Petrography, an introduction to the study of rocks in thin sections (2nd edition): W.H. Freeman and Company, San Francisco, 626 p.

White, W.M., 2005, Stable isotope geochemistry. *In: Geochemistry*, Chapter 9. Free online textbook

Yang, K., 1998, Compositional variations of white micas – a literature review: *CSIRO Exploration and Mining*, report 469F, 24 p.

Appendix 1: Sample locations and descriptions

The 11 rock samples were collected by Kim Hein and Frank van Ruitenbeek during their fieldwork in the Panorama district, November 2003. The following information on the rock samples is based on fieldnotes taken during their fieldwork. Locations are in AMG zone 50 grid coordinates using the AGD66 projection.

Sample p03	
	AMG coordinates: 732149;7652212
	Primary rock type: Chert
	Field description: Finely laminated grey-black chert. The chert forms a topographic high.

Sample p04	
	AMG coordinates: 732075;7652243
	Primary rock type: Dacite
	Field description: Dacite with non-pervasive fracture cleavage. The rocks dip gently west.

Sample p05	
	AMG coordinates: 732019;7652227
	Primary rock type: Rhyodacite
	Field description: Rhyodacite with non-pervasive fracture cleavage.

Sample p06	
	AMG coordinates: 731948;7652246
	Primary rock type: Dacite
	Field description: Quartz-feldspar porphyritic dacitic lava. The rock contains sulphides and is silicified.

Sample p07	
	AMG coordinates: 731904;7652275
	Primary rock type: Dacite
	Field description: Fractured quartz-feldspar porphyritic dacite. The rock is a hydroclastic breccia and located near a Fe-Mn gossan.

Sample p08	
	AMG coordinates: 731830;7652342
	Primary rock type: Dacite
	Field description: Fractured and altered dacite. The rock is located near a fault structure and completely broken.

Sample p09	
	AMG coordinates: 731800;7652376
	Primary rock type: Basalt
	Field description: Vesicular pillow basalt. Vesicles are filled with quartz.

Sample p10	
	AMG coordinates: 731762;7652380
	Primary rock type: Basalt
	Field description: Altered pillow basalt. The rock contains quartz.

Sample p12	
	AMG coordinates: 731721;7652460
	Primary rock type: Basalt
	Field description: Epidote-bearing chlorite-quartz-actinolite altered pillow basalt and lava flow.

Sample p13	
	AMG coordinates: 731649;7652481
	Primary rock type: Basalt
	Field description: Epidote-bearing chlorite-quartz altered hyaloclastic basalt. Some parts are more massif.

Sample p14		
	AMG coordinates: 731735;7652931	
	Primary rock type: Basalt	
	Field description: Very fractured and altered hyaloclastic basalt.	

Appendix 2: MATLAB code

This appendix includes the MATLAB code used for major component calculations and written by M.A.T. van Hinsberg.

```
function result = project(V, y)
grootteV = size(V);
groottey = size(y);
if (groottey(2) ~= grootteV(2))
    result = 'Fout: de lengte van V is ongelijk aan de lengte van y';
end
if (groottey(2) == grootteV(2))
    for m = [1:groottey(1)]
        C=zeros(grootteV(1),grootteV(1));
        for i = [1:grootteV(1)]
            for j = [1:grootteV(1)]
                for k = [1:grootteV(2)]
                    C(i,j)=C(i,j)+V(i,k)*V(j,k);
                end
            end
        end
        d=zeros(1,grootteV(1));
        for i = [1:grootteV(1)]
            for k = [1:grootteV(2)]
                d(1,i)=d(1,i)+y(m,k)*V(i,k);
            end
        end
        CI=transpose(inv(C));
        e(:,m)=CI*transpose(d);
        for o = [1:100]
            D=C;
            grootteD=grootteV(1);
            H=V;
            for i = [grootteV(1):-1:1]
                if(e(i,m)<=0.00001)
                    e(i,m)=0;
                    D(i,:)=[];
                    D(:,i)=[];
                    H(i,:)=[];
                    grootteD=grootteD-1;
                end
            end
            f=y(m,:)-transpose(e(:,m))*V;
            g=zeros(1,groottey(2));
            for i = [1:groottey(2)]
                if(f(i)<0)
                    g(i)=f(i);
                end
            end
            d=zeros(1,grootteD(1));
            for i = [1:grootteD(1)]
                for k = [1:grootteV(2)]
                    d(1,i)=d(1,i)+g(k)*H(i,k);
                end
            end
```

```
            DI=transpose(inv(D));
            erbij=DI*transpose(d);
            for i = [1:grootteV(1)]
                if(e(i,m)<=0)
                    grootteE=size(erbij);
                    for k = [grootteE(1):-1:i]
                        erbij(k+1,1)=erbij(k,1);
                    end
                    erbij(i,1)=0;
                end
            end
            e(:,m)=e(:,m)+erbij;
        end
    end
    result = transpose(e);
end
```